POLITECNICO DI TORINO

Collegio di Ingegneria Meccanica, Aerospaziale e dell'Autoveicolo

Corso di Laurea Magistrale in

INGEGNERIA MECCANICA (MECHANICALENGINEERING)

Master thesis

In-Process Mitigation of Residual Stress in Laser Powder Additive Manufacturing

Supervisor:

Prof. Abdollah Saboori

Co-supervisor:

Dr. Reza Ghanavati

Dr. Mohammad Taghian Todeshki

Candidate:

Ali Kazemi Movahed

July 2025

1. Contents

List of Figures

List of Tables

Abtract

Residual stress is a critical challenge in Laser Powder Bed Fusion (L-PBF) that can compromise the mechanical performance and dimensional accuracy of printed parts. This study investigates the influence of different scanning strategies—defined by rotation angles (45°, 67°, and unidirectional) and scanning continuity (continuous vs. discontinuous)—on residual stress development in Ti-6Al-4V components fabricated using L-PBF. A combination of experimental measurements using X-ray diffraction (XRD) and finite element simulations was employed to evaluate the residual stress magnitude, temperature distribution, and uniformity across six distinct scanning patterns.

XRD results revealed that the discontinuous 67° rotation strategy produced the lowest residual stress (220 MPa), while the continuous unidirectional strategy resulted in the highest (648 MPa). Simulation results confirmed these trends and further highlighted that interlayer rotation and scan path discontinuity promote a more homogeneous stress field by disrupting repetitive heat input and facilitating thermal relaxation. Among the strategies analyzed, discontinuous 67° rotation emerged as the most effective, providing perfect balance between reducing peak residual stresses and enhancing stress uniformity.

This study demonstrates the importance of optimizing scanning strategies for residual stress mitigation in L-PBF. The insights gained provide valuable guidance for improving the structural integrity and reliability of additively manufactured components.

Keywords : Additive manufacturing, Residual stress, Formation mechanisms, Measurement methods, heat treatment, Laser-based additive manufacturing (LAM) process parameters, Finite element method, Numerical modeling

Acknowledgments

First and foremost, I want to sincerely thank my supervisor, Dr. Saboori, for his invaluable guidance, constant support, and patience throughout this journey. His expertise and thoughtful advice have been essential in helping me shape this thesis, and I’ve learned so much from him—not just academically, but personally. I’m genuinely grateful for the opportunity to work under his supervision.

I’m also deeply thankful to Dr. Reza Ghanavati for his kindness, wisdom, and encouragement. His thoughtful insights and willingness to help, no matter how busy he was, truly made a difference and meant a lot to me.

My sincere thanks also go to Dr. Mohammad Taghian Todeshki, whose support and encouragement helped me stay focused and motivated throughout this work.

To my family, thank you from the bottom of my heart. Your love, prayers, and constant belief in me have been my anchor. Even when we were miles apart, I always felt your presence and support. This achievement is as much yours as it is mine.

Finally, to everyone who stood by me in this journey, thank you. This has been a long and challenging road, but your support made it possible.

1. Introduction

In 1984, the patent enabled the fabrication of three-dimensional (3D) objects[1], marking a revolutionary shift in the production industry and introducing a new method called Additive Manufacturing (AM). Compared to other traditional manufacturing methods, this modern approach allows the fabrication of complex geometries[2] with minimal environmental impact[3] and interconnected porous structures [4] with higher azccuracy[5] and more design flexibility[6], obtaining near-net shaped parts with opportunities for in-situ alloying and development of novel alloys[7], [8]. Furthermore, AM offers several advantages, such as cost efficiency, faster production rates[9], shorter lead time[10], and sustainability[11]. Recent advancements in hybrid processing, including the integration of AM with conventional methods, have led to improved production capabilities and better performance [12].

AM technologies can be divided into several categories in terms of energy source and material used as feedstock. Energy sources such as lasers or electron beams are used to process materials, which may be liquid, solid [13], or in powder form, to melt[14], cure[15], or sinter[16]. Among all AM techniques, metal AM has become a promising technology for producing parts with finer microstructure[17] and enhanced mechanical properties[18] through rapid solidification[19]. Systems like Laser Powder Bed Fusion (L-PBF), Directed Energy Deposition (DED), and Electron Beam Powder Bed Fusion (EB-PBF) provide high strength, toughness, and corrosion-resistance components by using metals like stainless steel[20] aluminum alloys, nickel alloys[21], copper alloys[22], and titanium alloys[23] as their feedstock. Therefore, metal additive manufacturing systems have come to play a crucial role in several industries, such as aerospace[24], medical[25], [26], repair[27], and tooling[28].

However, dealing with high-power energy sources will raise challenges like high production costs[29], porosity and anisotropy[30], [31], poor surface finish[32], poor wettability[33], limited resolution[5], the need for post-processing[34] and slower production rates[35]. These constraints must be managed in large-scale applications. The reason behind these issues lies beneath the core principle in metal AM, which is the temperature gradient. The lack of thermal distribution management will cause defects such as cracking, delamination, and distortion. For instance, in L-PBF, a high-power laser is used to melt powdered metal spread over a platform selectively[36], [37], as depicted in Fig. 1. The laser increases the temperature of powder metal locally and rapidly, generating a significant thermal gradient between the outer and inner layers[38]. The outer layers cool down more quickly than the inner layers, which leads to non-uniform solidification and shrinkage due to the volumetric changes that occur as the material transitions from liquid to solid. These processes introduce self-balancing stress, known as residual stress[39] within the material, which is the source of most common defects in fabricated parts produced via metal AM.

Residual stress is one of the common defects in metal AM[40]. This stress is generated during the cooling of layers in the fabrication process[41]. When the layer cools down rapidly from high temperatures, grain boundaries cannot move or deform to release the stress trapped within the structure[42]. In other words, the inability of grain boundaries to relax causes the trapping of thermal strain within a component, manifesting as residual stress[43], [44].

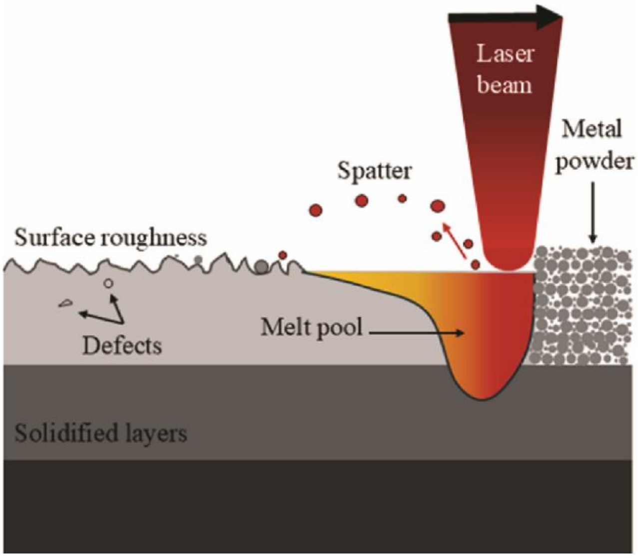

Fig 1. Representation of laser powder bed fusion process

Residual stresses have destructive effects on the mechanical properties of parts[45]. For instance, common problems include warping, distortion[42], cracking[46], delamination[44], geometric inaccuracies[47], reduced fatigue performance[48], and out-of-plane deformation[49]. These effects are depicted in Fig. 2 as a consequence of residual stress during fabrication. To avoid these defects, controlling and mitigating residual stress in manufacturing methods have become important research topics. Research has focused on methods for reducing residual stress and its negative consequences on the performance and longevity of parts.

Several strategies have been explored for reducing residual stresses, including pre-processing, in-situ, and post-processing interventions. Pre-heating the powder bed or build chamber reduces residual stresses by minimizing the thermal gradient between the build and the surrounding environment[50]. Post-processing methods like annealing relieve residual stresses, achieving reductions of up to 90% based on treatment temperature and duration[51]. Other methods, including heat treatment, vibrational stress relief[52], [53], [54], and shot peening[54] , are effective but add extra time and cost to the manufacturing process.

Therefore, in-situ techniques to control residual stress are less time-consuming and costly than other reduction strategies. Parameters like laser power, scanning speed, hatch spacing, and scanning strategy directly influence thermal history, temperature gradients, and cooling rates, which drive residual stress formation. Higher laser power creates a larger, deeper molten pool, increasing the temperature gradient and, consequently, the residual stress. Thus, fine-tuning laser power and other process parameters will balance the size of the molten pool, temperature gradient, and residual stress. Furthermore, the latest research suggests that machine learning strategies enable precise control of process parameters, in real time, to obtain an ideal molten pool, which helps mitigate residual stress[55].

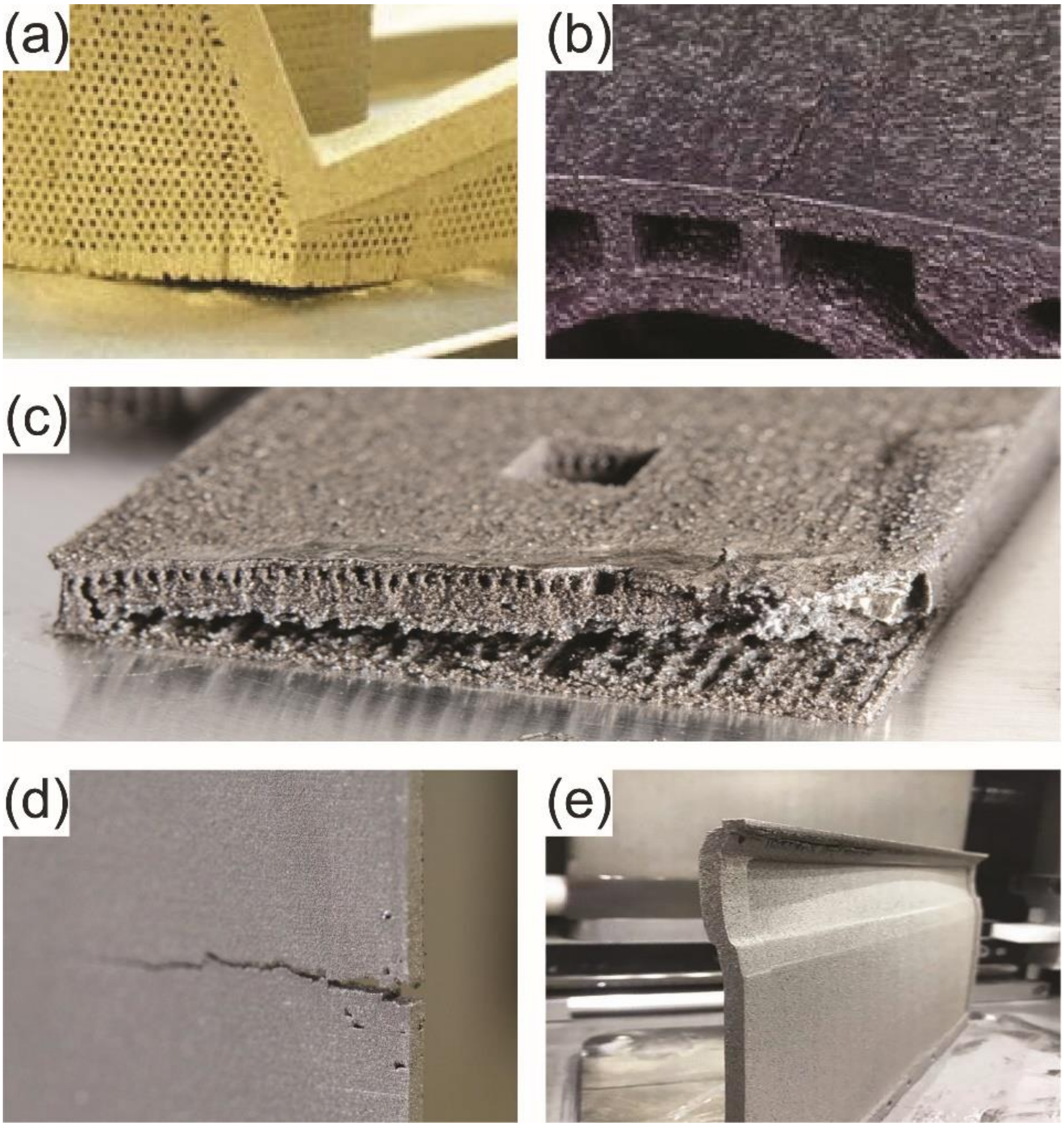

Fig. 2 Defects during the fabrication: a) warping and layer separation caused by high residual stress and b) cracking in the part due to accumulated tensile stresses[56]. c) Distortions and delamination during the AM process[42]. d) Failure during manufacturing of a Ti-6Al–4V component caused by the build-up of residual stress[57]. e) Example of a build that failed for a thin plate[36].

Process parameters can be divided into several groups: energy input and heat management, thermal gradient control, material and build configuration, and structural and mechanical integration. Laser power, scanning speed, scanning strategies, layer thickness, and hatch spacing are crucial in determining molten pool characteristics and residual stress development during production. For example, a study shows that the deposition pattern in DED fabrication of 316L stainless steel affects residual stress distribution. Residual stress levels on the top surfaces are similar, and the lateral surfaces of samples with a 90° rotation in the deposition pattern exhibit higher residual stresses due to variations in cooling rates during the process[58].

Hence, prediction of residual stress in L-PBF is critical step toward understanding and reducing its consequences. Several prediction approaches have been implemented by researchers and engineers to fulfill this purpose. These approaches include validation by experimental methods, analytical methods, computation methods, multiscale modeling, and data-driven models. For instance, after the fabrication of the parts with custom process parameters such laser power, hatch space, or scanning strategy, measurement methods can be applied to obtain the residual stress value. Then, the effect of the process is revealed, and different process parameters influence are depicted. However, these methods are best for validation, not prediction and implementing these instruments will be costly and time consuming.

Residual stress evolution can be modeled using mathematical formulations in an analytical method. In this approach, melting and cooling phase are simplified by elasticity theory and 1D or 2D heat transfers. These simplified governed equations provide closed-form solutions for stress and strain distribution. The most flexible tool for RS prediction is computational methods- particularly finite element analysis (FEA). FEA enables simulation and studying of formation of melt pool during the L-PBF which enables investigation of thermal gradient, temperature distribution, and residual stress generation. Simulation may include thermal analysis, mechanical or fully coupled thermos-mechanical models based on the level of complexity of the problem. In thermal analysis, the heat from the laser is considered as input and by implementing the analysis, temperature distribution, cooling rates, and melt pool shape can be revealed. In the mechanical analysis, thermal history of the component is fed to model obtain stress, strain, and distortion. In more complex models like thermos-mechanical coupled analysis, the model solves the heat and stress problems simultaneously. Several researchers have set up a finite element model to explore thermal history and formation of residual stress in the AM. X.X. Yao and Z. Zhang[59] developed FE model in COMSOL Multiphysics and ABAQUS and simulate the L-PBF process of 1.4 mm × 0.6 mm × 0.05 mm powder layer of Ti-6Al-4V. Hongjian Zhao et al. set up a 3D coupled thermo-mechanical model in ABAQUS for predicting residual stress in functionally graded Ti-6Al-4V / Inconel 718 parts fabricated by LAM. Furthermore, computation methods enable the exploration of process parameters on mechanical properties and quality of final part. For instance, Yang et al.[60] ran thermo-mechanical coupled simulation using Differential Quadrature Method (DQM) to analyze the effects of porosity, ceramics, and scanning parameters on residual stress and temperature distribution in laser powder bed fused titanium-matrix composites (TMCs).

The primary goal of this thesis is to investigate and mitigate the formation of residual stress in metal parts fabricated by L-PBF through a comprehensive multi-phase approach. Residual stress, resulting from non-uniform thermal gradients and rapid solidification during the additive process, significantly affects the dimensional accuracy, mechanical performance, and overall reliability of printed components. In this study, the focus is on analyzing the effect of scanning strategies on residual stress distribution using finite element (FE) simulations in ABAQUS, coupled with experimental validation via the XRD measurement method.

Chapter two, titled “State of the Art,” provides a comprehensive review of the formation mechanisms, classification, and measurement techniques of residual stress in Laser Powder Bed Fusion (L-PBF). It explores the key physical phenomena such as thermal gradients, phase transformations, and cooling cycles that contribute to stress accumulation during the additive manufacturing process. The chapter also categorizes residual stress by scale (Type I, II, and III) and critically examines various destructive and non-destructive measurement methods. In addition, it outlines current mitigation strategies—pre-process, in-situ, and post-process—

focusing on how process parameters such as laser power, scanning speed, scanning strategy, and energy density influence residual stress. The chapter concludes by reviewing recent advances in simulation-based modeling and machine learning approaches aimed at improving residual stress prediction and control in metal AM.

Chapter three, titled “Material and methods,” outlines the experimental procedures and simulation framework used to investigate residual stress mitigation in Ti-6Al-4V parts produced by Laser Powder Bed Fusion (L-PBF). Six scanning strategies—three continuous and three discontinuous—were applied to fabricate samples under controlled parameters. Experimental analyses, including 3D X-ray CT and surface roughness measurements, were complemented by coupled thermo-mechanical simulations in Abaqus. Temperature-dependent properties and user subroutines (DFLUX and USDFLD) were implemented to model laser-material interaction and phase transitions, enabling accurate prediction of thermal behavior and residual stress fields across different scan strategies.

Chapter four, titled “Results and Discussion, analyzes how scanning strategies affect residual stress in L-PBF. Experimental and simulation results show that discontinuous strategies—especially 67° rotation—achieve higher density, lower porosity, reduced surface roughness, and significantly lower residual stress. Continuous unidirectional scanning performed the worst due to heat buildup and stress concentration.

Chapter five, titled “Conclusion and Future Perspective,” concludes that discontinuous scanning strategies—especially 67° rotation—effectively reduce residual stress, porosity, and peak temperatures in L-PBF of Ti-6Al-4V. Future work should explore fatigue performance, extend simulations to multi-layer builds, and apply machine learning to optimize process parameters.

The aim of this study is to investigate the effect of different scanning strategies—specifically varying rotation angles and continuity modes—on the formation and mitigation of residual stress in Ti-6Al-4V parts fabricated via Laser Powder Bed Fusion (L-PBF). The study combines experimental measurements using X-ray diffraction (XRD) with finite element simulations to evaluate how these scanning strategies influence the magnitude, distribution, and uniformity of residual stress fields, with the goal of identifying optimal strategies that minimize residual stress and enhance part quality.

2. State of Art

2.1. Residual stress

2.1.1. Classification and formation mechanisms

Analyzing the stresses within the solidified layers during the heating and cooling cycles of L-PBF is an important step in understanding the origin of residual stress. The volume shrinkage and temperature gradients between layers play a key role in stress generation. Three mechanisms are suggested for the formation of residual stress: Temperature Gradient Mechanism (TGM), Cool-Down Mechanism, and Phase Transformation.

When the laser irradiates the powder, it creates a hot zone that cools down rapidly. The hot zone causes thermal expansion, which generates tensile stress in the upper layers and compressive stress in the lower layers. As layers are added as the fabrication process continues, residual stress builds within the part. The second mechanism, known as the Cool-down mechanism, occurs once the part cools after being removed from the build platform. During the heating cycle, the new layer experiences higher temperatures and expands. However, this expansion is constrained by the less expanded inner layer, resulting in the formation of compressive stress in the outer layer and tensile stress in the inner layer. Likewise, in the cooling cycle, the outer layer contracts more than the inner one and pulls away from it. The interaction forms tensile stress in the outer layer and compressive stress in the inner layer as shown in Fig. 3a, b. In general, the outer layers cool faster, creating tensile stress on the surface and compressive stress in the inner layers, especially in thicker sections or large parts[28], [52], [61], [62].

Phase transitions in some alloys during the AM process can also induce residual stress. For instance, Rangaswamy et al.[63] suggested that the generation of residual stress in stainless steel fabricated by laser-engineered net shaping (LENS) could be due to the phase transformation from δ-ferrite to austenitic stainless steel. Such transitions can lead to material expansion or contraction, resulting in tensile stresses. This formation mechanism is called the solid-state phase transition. As another example, Vyatskikh et al.[64] investigated the effect of solid-state phase transformations on residual stresses in the parts fabricated by DED. This study used two different materials: pure iron (Fe) and an iron-copper (Fe–50Cu wt%) alloy. The results showed that pure Fe undergoes a phase transformation with volume expansion, while Fe–50Cu shows a decrease in volume, suggesting that material selection and phase transformations influence residual stress and microstructure.

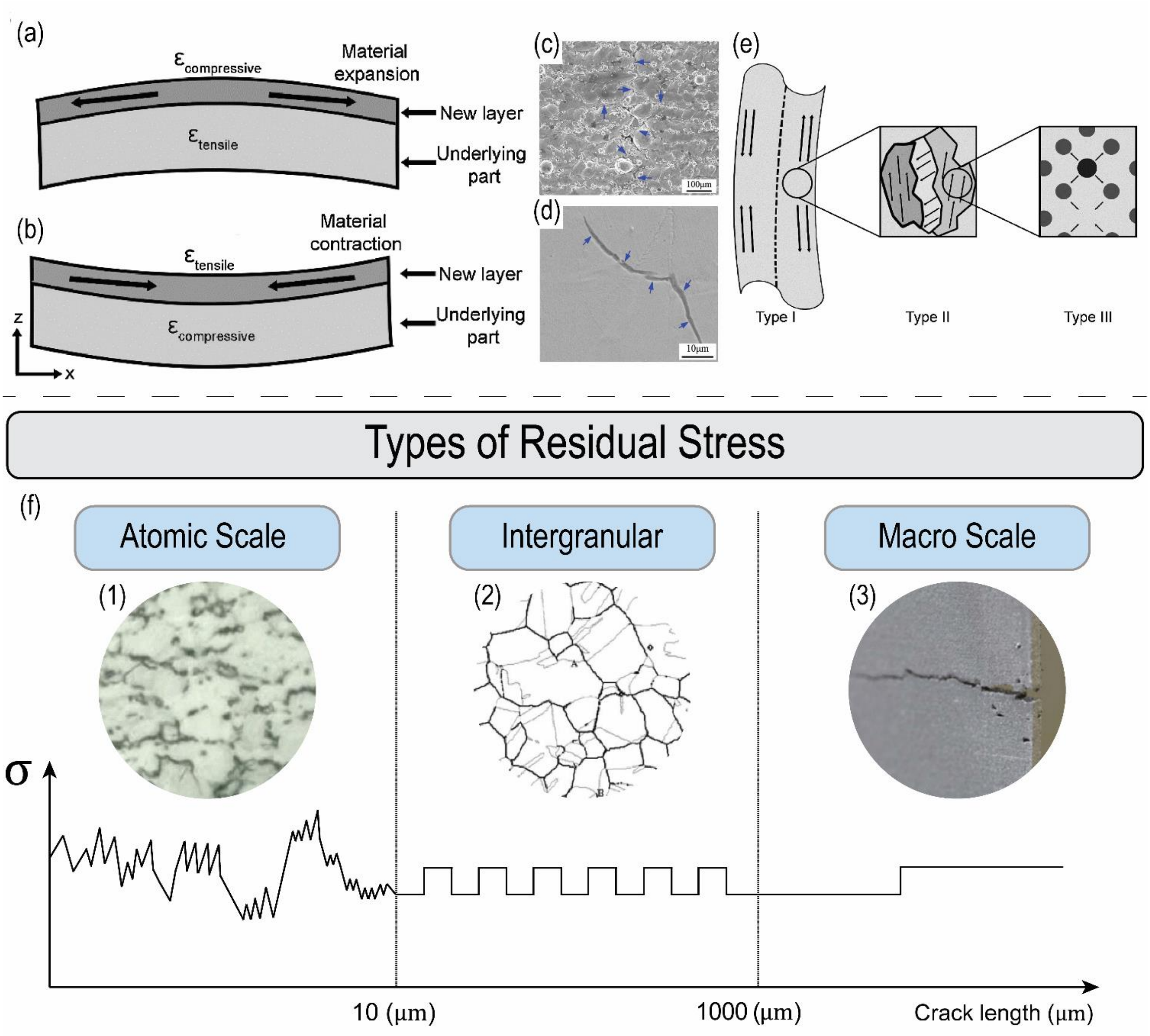

Fig. 3 Classification and formation mechanism of residual stress: a) Basic mechanisms of stress and plastic deformation development during: a) heating and thermal expansion of new layer (Top) and b) cooling and thermal contraction of new layer (Bottom) [65]. Cracks on the L-PBF part: c) Macro and d) Micro cracks[66]. e) A schematic of different types of residual stress divided based on their crack length[65]. f) Three different types

of residual stress - type I, type II, and type III concerning their different crack spans: 1) Atom probe tomography analysis of hydrogen distribution in laser peened Ti6Al4V alloy: Implications for residual stress evolution and hydrogen embrittlement control[67] 2) OIM grain boundary map with twin boundaries indicated by finer lines in Ni-base (alloy 600) stainless alloys[68] and, 3) Crack formation in a Ti6A14V thin wall produced via L-PBF caused by the build-up of residual stresses[57].

Residual stress is categorized by length scale into three types[69]. Type I (Macro Residual Stress) occurs at a macro level, typically over 1mm, and is caused by non-uniform plastic deformation and thermal loads during fabrication or post-treatment[65], [70]. In AM, controlling these stresses is crucial because they significantly affect part distortion and fatigue properties[71], [72], [73]. Type II (Intergranular Residual Stress) affects areas between 0.01 mm and 1.0 mm and arises from microstructural effects like differences in slip behavior between grains. Though present in polycrystalline materials, Type II stresses are less discussed in AM due to complex measurement methods and their secondary impact on material properties. The two crack levels associated with Type I and Type II stresses are depicted in Fig. 3c, d. At the atomic scale (<0.01 mm), Type III stresses are caused by lattice mismatches, dislocations, and grain boundary coherence but are less critical for AM components. Fig. 3e and 3f illustrate the types of residual stress and their crack associated length.

2.1.2. Measurement methods

Residual stress is the phenomenon that can alter the mechanical properties and influence the performance and reliability of the L-PBF fabricated parts under failure conditions. Therefore, monitoring and measuring residual stress is essential before operational use. Numerous methods and techniques have been developed to track, measure, and report the magnitude and distribution of residual stress. Based on the range of damage they cause to the component during the measurement process; these methods are categorized into two main groups: destructive and non-destructive.

X-ray diffraction is one of the most accurate non-destructive methods for measuring residual stress within a component[74]. This technique is based on the change in lattice spacing caused by residual stress, compared to the stress-free state. X-rays are directed at the crystal lattice, where they scatter and produce a diffraction pattern[75]. The diffraction pattern reveals information about the gap between the layers, which is calculated using Bragg's law, as illustrated in Eq. (1)[76] :

$$n\lambda = 2d \sin(\theta) \tag{1}$$

where n is the diffraction order, λ is the X-ray wavelength, d is the lattice spacing, and θ is the angle of incidence (Fig. 4).

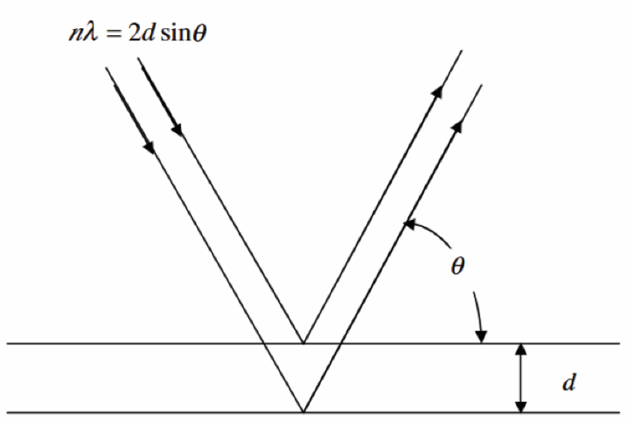

Fig. 4 Parameters of Bragg's law in X-ray diffraction[77].

The core idea behind this technique is that the lattice spacing within the material is affected by residual stress. By utilizing Eq. (2), the relationship between the lattice strain (ε), lattice spacing (d) and the angle of incidence (ψ) can be elucidated:

$$\tan(2\theta) = \frac{\lambda\varepsilon}{d}\sin^2(\psi) \tag{2}$$

where θ is an angle at which diffraction occurs and λ is a wavelength of the X-ray used. As depicted in Eq. (2), normal stress is related to the change in the lattice spacing normal to the diffracting plane. The formula indicates that changes in diffraction peak position result from strain and changes in lattice spacing, both induced by residual stress (the stress component (σ)). Therefore, special equipment is required, which increases the overall cost of applying this method. These methods also have limitations, such as surface sensitivity[78] , limited depth penetration [79], and a limited range of materials (only crystalline material)[80].

Synchrotron is another non-destructive method used to obtain the magnitude of residual stress. It operates on the same principle as conventional XRD, but uses high-power, intense X-rays, enabling deeper penetration. Therefore, deeper residual stress measurement can be achieved by using a synchrotron[79]. Also, in comparison to conventional XRD, this approach offers higher resolution and faster data acquisition. However, one of its limitations is the requirement for costly facilities, leading to higher overall experimental costs.

Neutron Diffraction (ND) is one of the advanced non-destructive techniques to measure residual stress in material. The approach follows the same rule as XRD but uses neutrons instead of X-rays. Strain calculation follows Eq. (2), the same as the XRD method. Eq. (2) explains the changes in lattice spacing (d) caused by stresses -residual or external- represented as variations in θ. Next, stresses are determined following Eq. (3) in which σ is stress in principal coordinates (like x, y and z), E is young modulus, ν is Poisson's ratio and ε is strain assessed by the ND[81]. Deeper penetration and bulk measurements are offered by neutron diffraction. Nevertheless, using specific facilities to accelerate the neutrons makes the approach more expensive compared to XRD[70], [82], [83].

$$\sigma_x = \frac{E}{(1+\nu)(1-2\nu)}[(1-\nu)\varepsilon_x + \nu(\varepsilon_y + \varepsilon_z)] \tag{3}$$

Meanwhile, one of the common and widely used semi-destructive methods, especially for surface residual stress, is hole-drilling strain gage method. In this technique, a small hole is generated on the surface of the component, which modifies the stress distribution. Then, the changes in radial and circumferential strains are measured by surface-mounted strain gauges. The relationship for calculating residual stress (σ_{r}) is given in Eq. (4):

$$\sigma_{\mathrm{r}} = -\frac{E}{1-\upsilon}(\varepsilon_{\mathrm{r}} + \upsilon\varepsilon_{\theta}) \tag{4}$$

where υ is the Poisson's ratio, ε_{r} the radial strain and ε_{θ} is the circumferential strain, making it suitable for surface stress measurement[84].

The ring-core method, like hole drilling, is semi-destructive but achieves higher accuracy by concentrating strain near the strain gauge rosette and isolating the core, thereby reducing errors[85], [86].

There are other non-destructive methods based on the changes which residual stress induces in the non-mechanical properties of the material. Magnetic methods offer a non-destructive and rapid approach for obtaining surface residual stress values[87], depending on the magnetic properties of components[88]. When a ferromagnetic material is exposed to a magnetic field, its microstructure aligns with the field, except in areas affected by defects and residual stress, leading to magnetic domain redistribution or reorientation and producing Barkhausen noise[89], which is analyzed to determine residual stress magnitude and direction. These methods are sensitive to surface conditions such as roughness and are mainly used for surface stress measurement[90].

Ultrasonic methods are a non-destructive way to obtain residual stress[91]. In this technique, the ultrasonic waves propagate through the component. The velocity of the waves and energy loss during the propagation through the material are affected by internal stresses[92]. This approach is suitable for bulk material as the waves can penetrate and propagate more easily in bulk materials than in complex geometries[93].

The contour method is one of the earliest measurement techniques that has been combined with finite element analysis[75]. In this destructive approach, the component is cut into two halves, and residual stresses cause deformation in each half during the stress relaxation phase. The post-cut deformation contours are measured using surface metrology devices such as optical scanners or Coordinate Measuring Machine (CMM) and are averaged to obtain the displacement field[75]. Next, the original non-deformed half of the component is modeled, and this displacement field is applied as a boundary condition to a finite element model (FEM) of one half of the original component before cutting to perform analysis and compute the corresponding stress field. The calculation of residual stress will follow the Bueckner's Superposition Principle which is depicted in Eq. (4):

$$\sigma_{\text{After cutting}} = \sigma_{\text{Residual}} + \sigma_{\text{Cutting plane}} \tag{4}$$

Eq. (4) shows that total stress within the component after cutting is the superposition of residual stress and stresses induced by cutting process. Therefore, by solving the FE model, the original residual stress distribution (σ_{Residual}) is reconstructed.

Fig. 5 compares residual stress measurement methods across various categories for further clarification. Furthermore, Table 1 summarizes the comparison between different measurement methods.

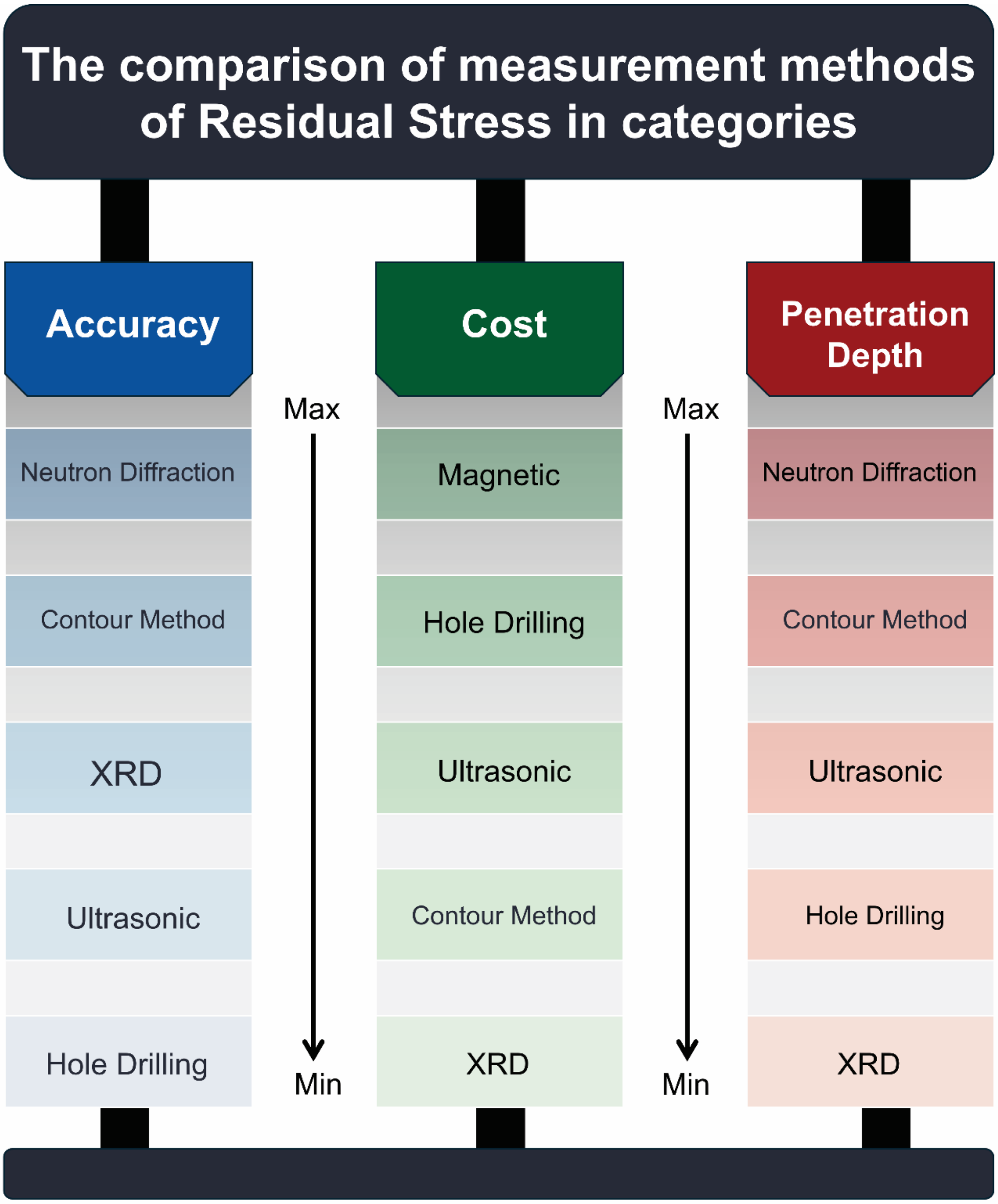

Fig. 5 The comparison of measurement methods in categories including penetration depth, cost, and accuracy - the methods are sorted from top to bottom[75], [94], [95].

Table 1 Ths summary of properties and comparison of measurement methods [75], [94], [95]

Method	Type	Fundamental	Surface Stress	Subsurface\internal stress	Depth	Limitation
X-ray diffraction	Non-destructive	Measuring lattice spacing – Bragg's law	✓	✗	~ 10-30 µm	Affected by grain size, surface only
Synchrotron x-ray diffraction	Non-destructive	Measuring lattice spacing	✓	✓	Up to ~10 mm (Ti alloys)	Expensive facilities, sensitive to geometry
Magnetic methods	Non-destructive	Measuring variations in magnetic signal caused by stress-induced domains	✓	✗	~0.2 mm	Applicable only to ferromagnetic materials, sensitive to surface condition
Ultrasonic methods	Non-destructive	Detecting velocity shifts caused by stress-induced domains in acoustic waves	✓	✓	Frequency dependant	Need for calibration, influenced by microstructure
Contour method	destructive	Calculating 2D stress by measuring deformation of cut parts	✓	✓	cm-scale	Precision cutting, further FEM analysis is needed
Neutron diffraction	Non-Destructive	Measuring deep internal lattice spacing using neutron scattering	✓	✓	Up to ~25 mm (steel), 100 mm (Al)	Slow process, expensive equipment
Hole Drilling	Semi-destructive	Altering stresses by applying strain	✓	✗	~1-2 mm	Requiring accurate calibration

2.2. Mitigation Methods of Residual Stress

Researchers and manufacturers have developed several methods and processes to control and mitigate residual stress before, during, and after production. These techniques are divided into three groups based on their intervention in fabrication: pre-process, in-situ, and post-process. For instance, pre-heating the powder bed is one of the pre-processing methods that can help reduce thermal gradients during the building process. In-situ methods focus on optimizing process parameters like laser power, scanning strategy, and scanning speed to obtain more uniform temperature distribution and lower temperature gradient to control residual stress during the manufacturing process. Post-process methods, such as heat treatment and shot peening, are applied to a component after production to relieve residual stress and improve the mechanical properties of a fabricated component. In this section, several researchers have been reviewed, and their roles in mitigating residual stress in L-PBF are discussed.

2.2.1. Pre-Process Methods

Pre-heating the powder bed is a common pre-process method that has shown effectiveness in reducing residual stress within the parts. For instance, experimental analysis on DED-fabricated Ti-6Al-4V thin walls has demonstrated that pre-heating the substrate to approximately 400 °C reduces peak tensile stress in the substrate by up to 40 % and distortion during the first layer deposition by 27%[96]. Similarly, Lu et al. analyzed the formation of residual stress and distortion in rectangular and S-shaped Ti–6Al–4V components fabricated by DED. They reported that peak tensile stress reached 560 MPa at substrate, while preheating the substrate up to 700 °C reduced residual stress and distortion by 80% and 90%, respectively[97]. Vasinonta et al. conducted temperature-dependent thermomechanical simulation of 2D thin-walled AISI 304 stainless steel structure during LENS process. Their findings confirmed that a 40% reduction in residual stress compared to the yield stress can be obtained by pre-heating to approximately 400 °C[98].

Hong et al.[99] showed a notable reduction in residual stress using real-time heating during DED. Mishurova et al.[100] found that a 650 °C heat treatment for 3 h nearly eliminated residual stress in Ti-6Al-4V fabricated by L-PBF. Similarly, Shiomi et al.[101] studied the impact of increasing powder bed temperatures to 80 °C, 120 °C, and 160 °C during the L-PBF process for chrome molybdenum steel (JIS SCM440).

Ali et al. [102] found that pre-heating the bed to 570 °C in L-PBF processing of Ti-6Al-4V caused a significant reduction in residual stress. They reported that heating the build platform to 570 °C diminished the formation of residual stresses within the components and decreased their magnitude. They used the L-PBF process to fabricate Ti-6Al-4V and introduced six cases with different preheating temperature conditions. The details and results are reported in Table 2.

Pre-process methods offer a reduction in residual stress but introduce tradeoffs in cost and built time. For instance, increasing the temperature of the powder bed to 570 °C (e.g., for Ti-6Al-4V) requires special equipment and time which extends both overall production cost and build time. Plus, controlling the production environment to avoid risk of oxidation for the materials such as Ti-6Al-4V necessitates the use of an inert gas. These considerations, combining maintenance cost and operators requirements, bring about challenges for industrial-scale adoption of pre-process stress mitigation strategies. Effectiveness of these methods, along with their impact on production efficiency and cost represents a critical trade-off in implementing residual stress mitigation strategies[103].

Table 2 Amplitude of residual stress concerning different cases of pre-heating temperature

Case	Pre-heat temperature (°)	Description	Residual stress (MPa)	Reduction (%)
T1	100	Standard bed temperature	214	-
T2	370	-	61	71 %
T3	470	-	25	88 %
T4	570	30 °C below the start of martensitic decomposition temperature	1	99 %
T5	670	30 °C below the start of the annealing temperature range	5	97 %
T6	770	20 °C below the start of the higher annealing temperature range	-4	98

2.2.2. Post–Process Methods

Post-heat treatment methods can also reduce stress locked within the component. These include methods such as annealing[104], hot isostatic pressing[105], and solution aging[106]. Frequently, post-heat treatment cycles are applied to L-PFB components to reduce the residual stress within the component, although this increases the time and cost of the manufacturing process[107]. These cycles prompt the material to respond to thermal stresses, altering its mechanical properties—such as toughness and ductility—without changing the material. Cruz et al. [108] applied heat treatment strategies to 316L austenitic stainless steel rectangular component produced by L-PBF. They investigated three heat treatment approaches: annealing at 400 °C for 4 h, annealing at 650 °C for 2 h, and solution annealing at 1100 °C for 5 min. The first approach reduced the residual stress value from 248 MPa to almost 191.1 MPa. The second one reduced the value of residual stress by 65 %, and the third one achieved nearly total stress relief (~90%) with no further reduction after longer holding times. Furthermore, results showed changes in microstructure as $\delta -$phase appeared in the range of 650 – 800 °C which directly affects ductility. The efficacy of heat treatment in reducing distortion and residual stress caused by various manufacturing processes has been highlighted in several studies.

For instance, Husson et al. discussed the application of stress relief on gearbox shafts manufactured by cold forging to decrease residual stress generated during manufacturing[109]. They applied treatment at 600 °C for 4 h in a low-pressure atmosphere which results in a reduction of residual stress from 300 MPa to 150 MPa. Moreover, they noted that residual stress can become heterogeneous in the automotive industry if the geometrical and stress requirements between the two rolling racks and both tips are not maintained during the heat treatment of gearbox shafts, potentially leading to deformation[109]. Similarly, Kwak et al. employing the hole drilling method and electronic speckle pattern interferometry (ESPI) equipment, measured the residual stress generated during the quenching heat treatment and observed a new distribution of stress patterns, indicating the necessity to consider the residual stress generated in previous heat treatment steps[110].

Several researchers conducted investigations to determine the effect of mechanical treatment and heat treatment on reducing residual stress and enhancing the mechanical properties of the component. For instance, Santa-aho et al.[111] applied stress relief annealing at 1030 °C for 60 min to a simple strip geometry made of austenitic stainless steel 316L fabricated by L-PBF, and shot peening was applied for different durations. Moreover, nitrogen gas was used to cool down the component. Shot peening increased surface hardness due to the induction of compressive stress.

Heat treatment has also been utilized to improve the mechanical properties of AM stainless steel 316L. Chimmat et al. discovered that heat-treating stainless steel 316L and CoCrMo alloy fabricated by the LAM process and reported a significant reduction in residual stress at the top surface and below according to X-ray diffraction measurements[112]. They applied heat treatment at 650 °C for 2 h and 30 min into stainless steel 316L, leading to a reduction in residual stress from 127 MPa on top surface to 93 MPa. and applied different heat treatments to CoCrMo alloy at 950 °C, 1050 °C, 1150 °C for 4 h in vacuum which exhibited sinusoidal behavior. Additionally, it was reported that the reduction of residual stress correlates with an increase in annealing temperature in AM stainless steel 316L fabricated by DED[113]. However, heat treatment methods are not reliable for reducing all types of residual stress. For instance, Wang et al. studied a staircase Inconel 718 part, noting that as-fabricated parts exhibit higher compressive residual stress compared to those subjected to stress-relieving methods, suggesting that stress relieving only partially alleviates stress[114].

Moreover, residual stress influences hardness, depending on the phase fraction and stress state. After stress relief heat treatment, the samples exhibited lower compressive residual stress due to the evolution of the microstructure during the heat treatment process[114]. For the heat treatment of Inconel 718 fabricated by AM, according to ASTM F3055 and Teixeira et al., the material must undergo homogenization (HO) at a temperature range of 1050 to 1080 °C for 1.5 h followed by air cooling (AC), a process that, while reducing residual stress, increases the risk of grain growth and recrystallization [115], [116]. Shiomi et al. reported an almost 70% reduction in residual stress in chrome molybdenum steel (JIS SCM440) fabricated by L-PBF by applying stress relief heat treatment at 500 °C – 700 °C for 1 h[101].

In summary, heat treatment methods are widely used to mitigate residual stress in the MAM process. Although their efficiency in enhancing mechanical properties is significant, procedure expenses, special equipment, and time constraints pose challenges for their practical implementation in reducing residual stress. Therefore, the need for efficient residual stress reduction has driven research into how process parameters affect stress levels and distribution.

In this situation, the control of residual stress (RS) becomes more accurate, faster, more cost-effective, and time-saving compared to traditional heat treatment methods.

2.3.3. In – situ methods

The high cost and time-consuming nature of heat treatment processes make tuning the process parameters a more compelling tool for reducing residual stress and distortion in parts fabricated by AM. Several parameters and aspects can be considered as key variables in mitigating residual stress during fabrication. Bian et al. highlighted that although numerous process parameters affect the product performance in AM[117], five key parameters are critical: laser power, scan speed, scanning strategy, hatching distance and layer thickness.

As the temperature gradient of the molten pool plays a crucial role in the mitigation of RS during manufacturing, understanding the effects and influence of process parameters on temperature gradient, size of the molten pool, and heat affected zone (HAZ) is crucial to tuning the parameters for reducing the RS and obtaining the uniform and evenly distributed temperature gradient. Several researchers conducted experimental analysis on different alloys to investigate the effect of increasing or decreasing each parameter on the characteristics of the molten pool and the thermal history of the process. For instance, Vasinonta et al. [96] delved into the AISI 304 stainless steel fabrication using the LENS process. Their research confirmed a direct relationship between the value of maximum residual stress and the thermal gradient. They observed that a decreasing temperature gradient led to a decrease in residual stress during the fabrication of SS304. These findings have also been supported by other researchers[118], [119].

This section gathers useful information about the parameters that can be tuned to mitigate the residual stress generated in the part during the L-PFB process. Fig. 6 depicts a schematic of important process parameters that can effectively mitigate the residual stress within the part.

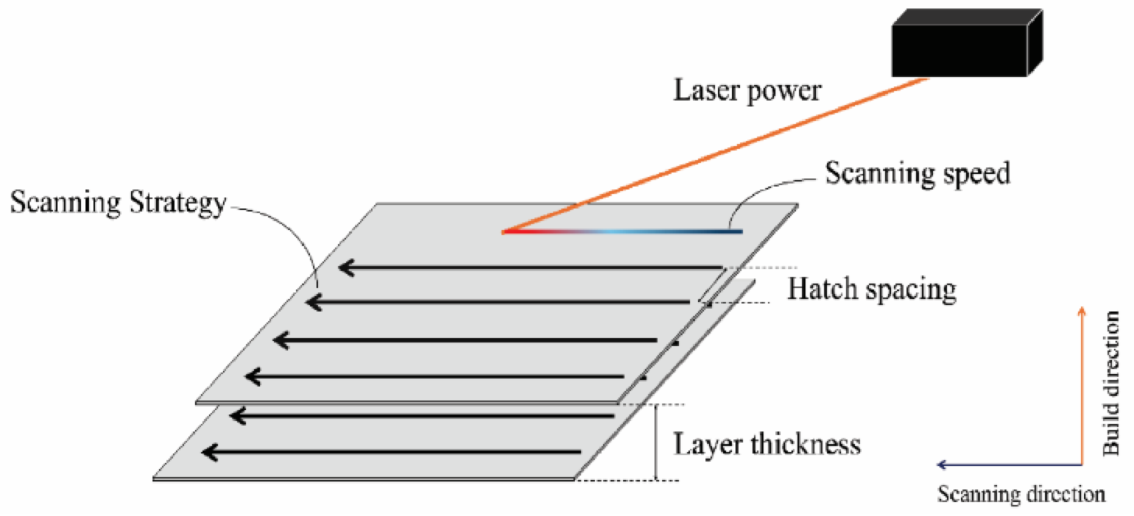

Fig. 6 The schematic of essential process parameters mitigating residual stress, including laser power, scanning strategy, scanning speed, and hatch spacing.

The period during which the energy source—either a laser or an electron beam—pauses and remains stationary at a specific point to melt the powder is called dwell time. During dwell time, thermal energy melts the powder and creates a temperature gradient. A steeper gradient often results in a deeper molten pool and higher residual stress. Therefore, controlling the dwell time can affect the thermal history of the part and molten pool. Increasing dwell time allows for better heat distribution and more even cooling, potentially reducing residual stress in the material[120]. Jendrzejewski et al.[121] investigated the laser cladding process of Co-based stellite SF6 alloy and found that increasing the time delay from 1 second to 60 seconds between the cladding of consecutive layers led to an increase in residual stress, as the temperature gradient became larger in this case.

However, thermal conductivity influences the transfer of thermal load and temperature distribution within the part during fabrication. Therefore, establishing the relationship between dwell time and residual stress poses a significant challenge. For instance, Dellinger et al.[122] studied the impact of dwell time on distortion and residual stress in Inconel 625 and Ti-6Al-4V alloys fabricated via DED process. Their findings (Table 3) revealed contrasting behavior in the two material systems with increasing dwell times. Components built using Ti–6Al–4V exhibited increasing residual stress levels with longer dwell times, while components made from Inconel 625 exhibited decreasing residual stress levels under the same conditions.

Additionally, the study highlighted that Inconel 625 possess a greater interlayer temperature difference than Ti-6Al-4V, attributed to its higher thermal conductivity. The experiment analyzed three different dwell times: 0, 20, and 40 s. Residual stress in the samples was measured using the hole-drilling method.

Table 3 Residual stress obtained for different dwell times in the AM process of Inconel 625 and Ti-6Al-4V alloys[122]

Alloy	0 s	20 s	40 s
Inconel 625	740 MPa	648 MPa (12%↓)	566 MPa (14%↓)
Ti-6Al-4V	98 MPa	176 MPa (80%↑)	218 MPa (24%↑)

As shown in Table 3, the alloys respond differently to increased dwell times. For instance, residual stresses in Inconel 625 decrease with longer dwell times, whereas in Ti-6Al-4V, they increase with longer dwell times. Dellinger et al. proposed that this phenomenon may be attributed to the alloys' varied responses to temperature and phase transitions occurring during the process, particularly in Ti-6Al-4V, which may result in an annealing effect that relieves residual stress[122]. Longer dwell time allows Ti-6Al-4V to undergo phase transformations, introduce lattice strain, and create stress concentrations between successive layers. Plus, combined with the lower thermal conductivity of Ti-6Al-4V, heat accumulates during the build, generating a thermal gradient that develops localized expansion/contraction and increases residual stress. On the other hand, Inconel 625 has higher thermal conductivity, which enables rapid heat dissipation through the part during fabrication. Longer dwell time allows more heat dissipation through the part. Therefore, fewer thermal gradients are generated during fabrication, reducing residual stress. In another research, Li and Xiong[123] investigated the effects of four interlayer dwell times, including 0, 120, and 300 s, and cooling to the ambient temperature in Wire Arc Additive Manufacturing (WAAM). They found that both longitudinal and transversal components of residual stress measured by the hole drilling method were effectively reduced by increasing the interlayer dwell time. For instance, the value of longitudinal residual stress for 0, 120, and 300 s and cooling to ambient temperature changes from 564 MPa to 547 MPa (3% reduction), 482 MPa (14.5% reduction), and 373 MPa (33.9% reduction). However, near the top of the part, the longitudinal stress first decreased, then increased with increasing the interlayer dwell time[123]. On the other hand, Dumontet et al.[124], in the L-PBF fabrication of Ti-6Al-4V using XRD to measure the residual stress, found increasing the number of parts (thereby increasing dwell time) enhances heat evacuation time, which in turn increases the thermal gradient, leading to a higher residual stress state[124], [125].

Furthermore, increasing or decreasing the time between the layers during the fabrication also affects the material's mechanical properties. Ivanov et al.[125] investigated laser metal deposited walls using Inconel 625 as the deposited material and AISI 316 as the substrate material. They found that when a new layer was added without any pause between layers, the part bent less, and internal stress was lower. On the other hand, when a pause occurred between the deposition of layers was applied, the metal part bent more, and the stress near the top and edges was higher than the material could withstand without deformation.

Layer thickness shapes the transfer of thermal load through the part during deposition, affecting the cooling rate throughout the process. Studies conducted by Van et al.[126], Zäh et al.[56], and Kruth et al.[127] have confirmed that an increase in layer thickness leads to a reduction in residual stress due to a slower cooling rate. In addition, Mirkoohi et al. investigated the effect of increasing the layer thickness from 30 µm to 50 µm on mitigating residual stress in L-PBF of Inconel 718. Selecting 150 W for laser power and 600 mm/s for scanning speed, with a scan vector rotation angle of 67 degrees between layers, Mirkoohi's findings, obtained using the X-ray diffraction technique at various depths, showed that the sample with a layer thickness of 50 µm exhibited higher residual stress levels[128]. The transition from tensile to compressive residual stress occurred at different depths for the two-layer thicknesses, with the

50-sample transitioning at a deeper level, revealing that residual stress increases with layer thickness. Roberts found that doubling the layer thickness increased residual stress by almost 172% in the investigation of the laser melting process of Ti-6Al-4V[129]. Furthermore, the results showed that the parts with two layers had a lower residual stress than the single layer in both the longitudinal and transverse residual stress components. This finding reveals that splitting the material deposition into more layers can reduce residual stress. However, the choice of material is effective in studying the effect of layer thickness on residual stress, as the size of powder particles sets the lower limit for layer thickness[129]. As a result, establishing a relationship between layer thickness and residual stress is challenging.

The thickness of the substrate can affect the value of residual stress during the manufacturing process. Feng et al. simulated the AM process using Q345 as the substrate and Y309L as the deposited material for substrate thicknesses of 5, 10, and 20 mm. It was found that increasing substrate thickness led to a decrease in maximum longitudinal tensile stress, while it only affected the distribution and magnitude of transverse stresses[130].

Furthermore, increasing layer thickness may increase the mechanical properties in some cases. For instance, Diaz et al. investigated the mechanical properties of Inconel 625 alloy fabricated by AM with layer thicknesses of 50 µm and 100 µm. They found that parts made with thicker layers (100 µm) became much stronger and exhibited greater elongation after heat treatment[131], suggesting that increasing layer thickness can help reduce residual stress within the part, leading to improved mechanical properties. However, increasing the layer thickness can also negatively affect the mechanical properties. Delgado et al.[132] noted that increasing layer thickness resulted in poorer mechanical properties, such as yield stress and elongation, in twenty iron-based parts fabricated by L-PBF methods.

Therefore, it can be concluded that the relationship between residual stress and layer thickness depends on several parameters, such as the AM process and material thermal conductivity. The molten pool is also affected by the layer thickness. Fig. 7 illustrates how layer thickness impacts the dimensions of the melt pool. As shown in Fig. 7, the thicker layer generates a larger molten pool. Also, it was mentioned that a larger molten pool tends to cool down more slowly. A slower cooling rate results in higher residual stress; therefore, thicker layers may lead to increased residual stress in the part.

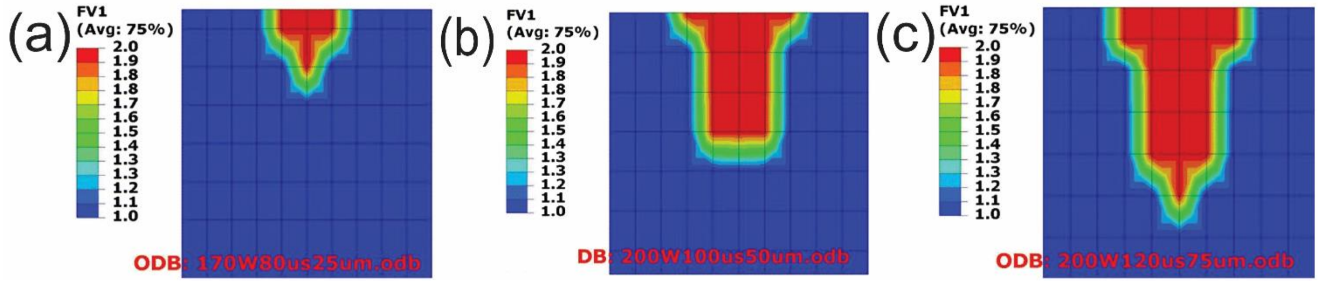

Fig. 7 The effect of the layer thickness on the dimension of the molten pool: a) 25 µm layer thickness, b) 50 µm layer thickness, and c) 75 µm layer thickness of L-PBF fabrication of Ti-6Al-4V[129].

Laser power controls the heating and cooling rate of the component during manufacturing. Therefore, among all the key parameters, laser power plays a more significant role as it is a critical parameter in generating thermal gradients, which results in residual stress[133]. The laser melts the powder metal and creates a molten pool. High laser power amplifies the rate at which the material heats and subsequently cools, contributing to residual stress formation[37]. Furthermore, increased laser power results in a deeper and larger molten pool. A larger molten pool extends the cooling duration, which is expected to mitigate the residual stress within the fabricated parts. However, scanning speed controls the duration of laser-material interaction, which, with laser power, shapes the molten pool geometry and characteristics. To confirm this, Ahmad et al. investigated the impact of laser power and other parameters on the densification of stainless steel 316L in the L-PBF fabrication. They found that the combination of laser speed and power is critical for ensuring the stability of the molten pool and obtaining a high percentage of densification (Fig. 8a)[134].

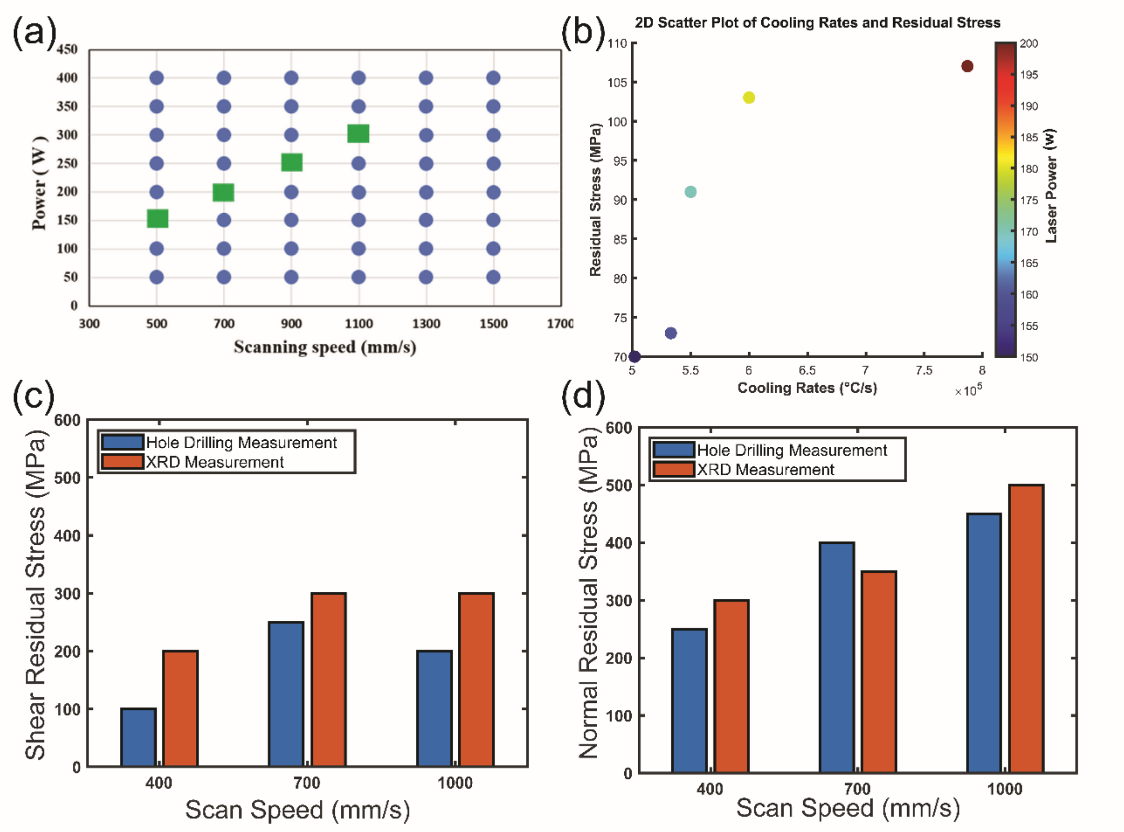

Fig. 8 a) Various combinations of laser power and scanning speed considered for study; green squares indicate a combination giving high densification (> 99.9%)[134]. b) Effect of varying the laser power on residual stress and cooling rate[129] . c) Shear residual stress and d) normal residual stress measured by XRD and hole-drilling residual stress measurements on the top surface of 12.7 mm L-PBF deposits fabricated with different scan speeds[135].

Fig. 8b demonstrates a discernible pattern: reduction in the cooling rate, predicted by finite element analysis, correlates with a decrease in the average maximum residual stress in L-PBF fabrication of Ti-6Al-4V by Ali et al.[129]. As depicted; as the cooling rate decreases, a reduction in residual stress is observed. Additionally, a decrease in power led to a downward trend in both cooling rate and residual stress, which was observed by Bartlett et al.[52] when exploring the influence of beam parameters on residual stress, as determined through X-ray diffraction (XRD), and affected the melt pool dynamics in stainless steel 316L processed by L-PBF.

The thermal energy transferred to powder during the heating cycle depends on the interplay between laser power and scanning speed. Laser power defines the amount of thermal energy required to melt down the powder, and speed determines the exposure time and cooling rate. Hence, the trade-off between energy input and heat dissipation is crucial to reducing residual stress. For instance, Levkulicha et al.[135] investigated the effect of laser power and scanning speed on molten pool size, which directly influences the mitigation of residual stress in the fabrication of Ti-6Al-4V using L-PBF. They employed X-ray diffraction and hole drilling for surface residual stress measurements alongside the contour method to gauge bulk stresses. The study varied laser power at 100 W, 200 W, and 300 W, along with different scanning speeds. Their results led them to conclude that a decreased scanning speed combined with increased laser power enlarges the molten pool. A larger molten pool slows the cooling rate, lowering residual stress. Increasing scanning speed while decreasing laser power reduces the molten pool's size. Consequently, the extended cooling time increases residual stress at the top and bottom surfaces of the part. Fig. 8c, 8d represent residual stress values at different scanning speeds.

Some studies have conducted numerical simulations or designed experimental setups to explore the impact of laser power on generating residual stress. Jonaet et al.[136] developed a thermo-mechanical coupling model for the L-PBF fabrication of the Ti6Al4V alloy with a unidirectional scanning strategy (Fig. 9a, b), revealing that von Mises residual stress increases with each successive layer added during manufacturing. As represented in Fig. 9, simulations of a five-layer structure with a laser power of 150 W and scanning speed of 750 mm/s, showed an increase in surface residual stress from 450.51 MPa to 981.23 MPa after adding the fifth layer. Furthermore, when the laser power was reduced to 120 W, maintaining a constant scanning speed of 750 mm/s, the residual stress for the first layer was measured at 417.52 MPa, indicating a 7.3 % reduction. The reduction persisted up to the fifth layer, where residual stress was 981.23 MPa for 150 W laser power, compared to 952.24 MPa for 120 W. These findings support the fact that an increase in laser power leads to higher residual stress, as illustrated in Fig. 9c–h. This observation was further corroborated in simulations conducted at a scanning speed of 1000 mm/s, where the residual stress for the fifth layer was 894.35 MPa at 120 W, compared to 935.72 MPa at 150 W[136].

In a separate study, Kaess et al.[42] set up numerical modeling using finite element methods to investigate the behavior of stainless steel 316L in L-PBF. By examining a range of laser powers—100, 150, 200, 250, 300, and 350 W—and maintaining a layer thickness of 30 μm with a laser speed of 850 mm/s, they found that the maximum residual stress values rose with an increase in laser power. In another study, Bian et al.[137] combined finite element modelling of the L-PBF process with experimental verification for stainless steel 316L, measuring residual stress through the X-ray diffraction method. Their investigation was performed with two distinct laser powers, 160 W and 200 W, with a constant scanning speed of 600 mm/s. Initially, they noted that residual stress distribution near the base of the printed structure was relatively uniform but decreased in comparison to the near top of the part. Furthermore, their findings indicated that employing 200 W of laser power led to significantly higher in-depth residual stress compared to 160 W across both stripe and chessboard scanning strategies. The values corresponding to the laser power of 200 W have been depicted in Fig. 10.

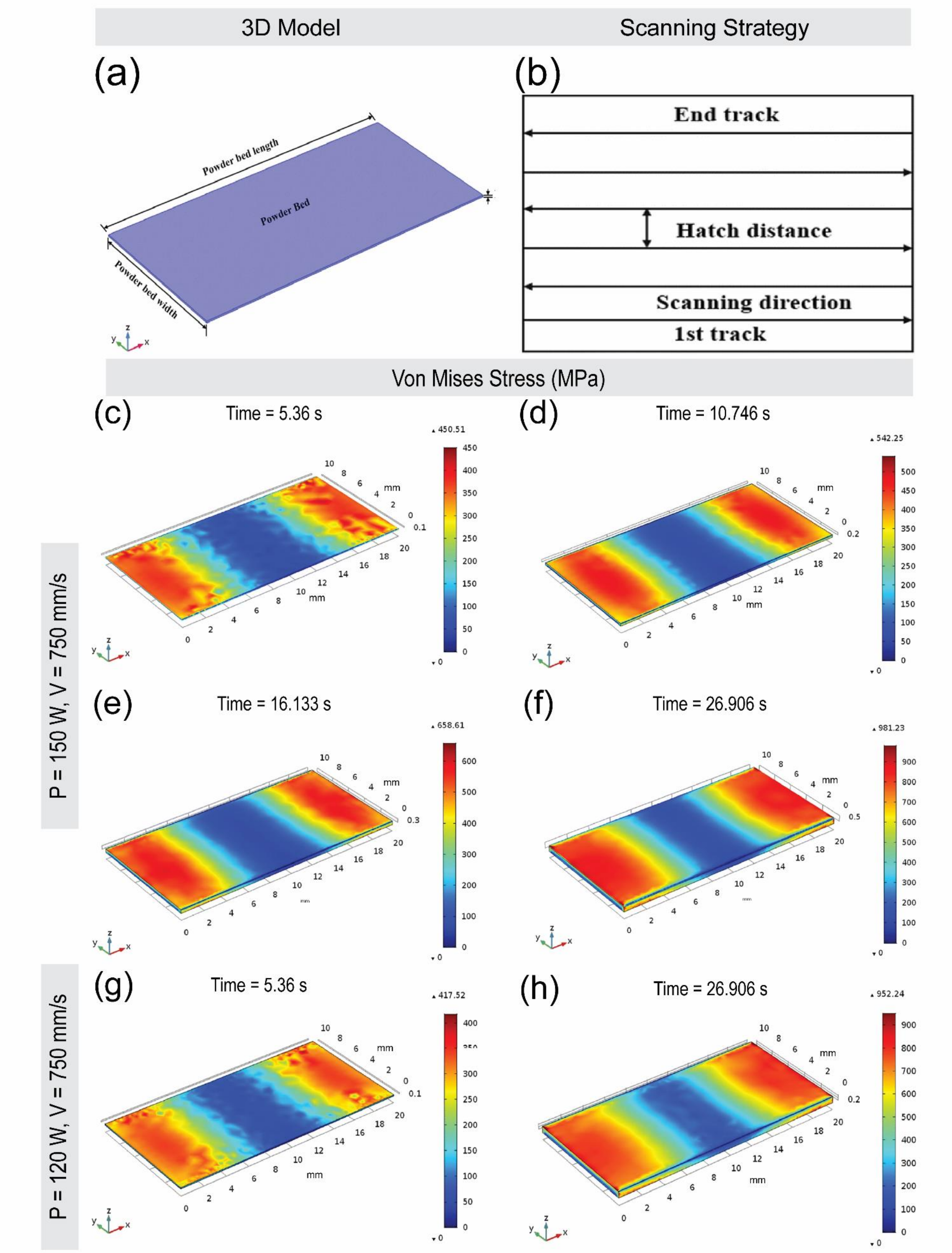

Fig. 9 Maximum von Mises stress at different laser power[136] : a) schematic of the solution domain consisting of powder bed, b) scanning strategy. Maximum von Mises stress at laser power 150 W and scanning speed 750 mm/s: c) at the end of the first layer, d) at the end of the second layer, e) at the end of the third layer, and f) at the

end of the fifth layer. Maximum von Mises stress at laser power 120 W and scanning speed 750 mm/s: g) at the end of the first layer and h) at the end of the fifth layer[136].

In conclusion, when optimizing laser power for the mitigation of residual stress, the role of scanning speed should not be overlooked. As Vastola et al.[138] highlighted, scan speed and laser power both influence on residual stress in Ti-6Al-4V. Mukherjee et al.[139] found that higher laser power worsened distortion and stress, while faster scan speeds reduced them and Yadroitsev et al.[140] emphasized the impact of laser power on layer bonding in single-track depositions. Overall, increasing laser power will lead to higher residual stress within the components.

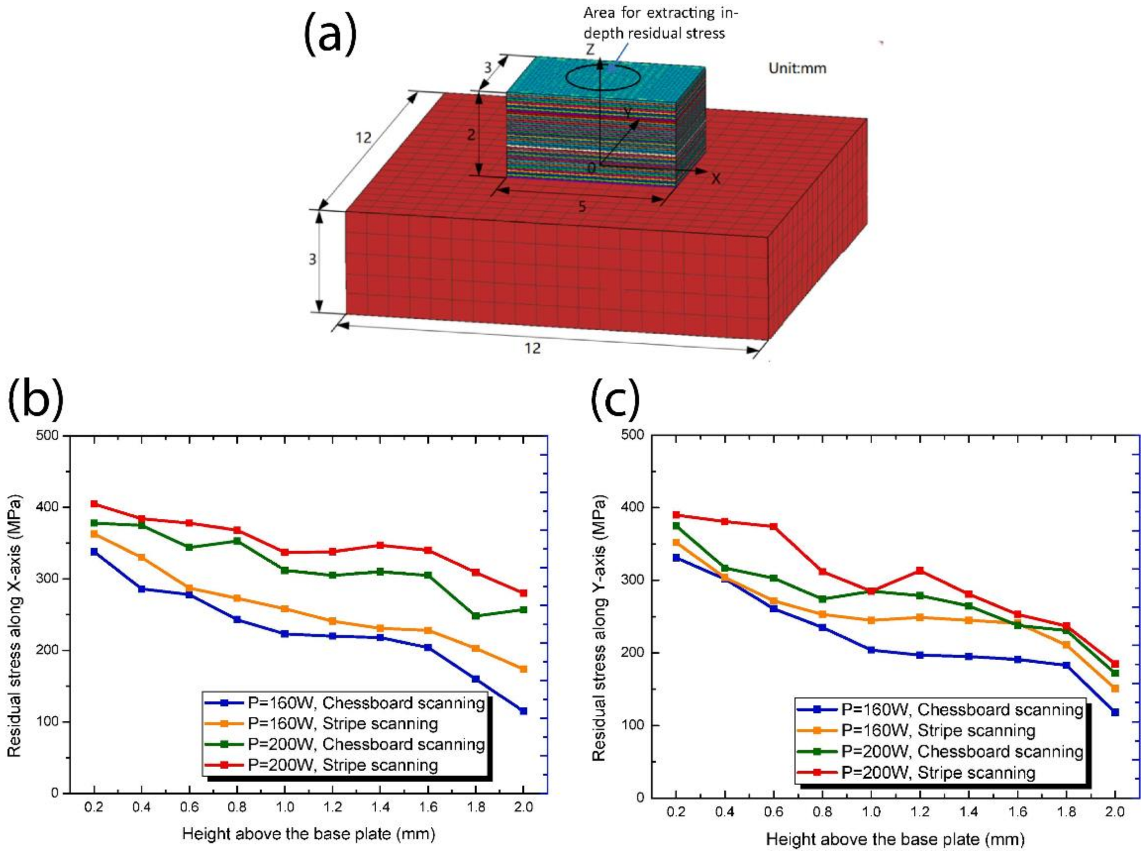

Fig. 10 Effect of laser power on formation of residual stress for two different scanning strategies[137]: a) schematic of the model used in FEA analysis of L-PBF, b) in-depth residual stress x direction, and c) in-depth residual stress in y direction of the component[137].

The impact of scanning speed alone on the manufacturing process is often not the primary focus; instead, the interplay between scanning speed and laser power is typically emphasized due to its significant effect on altering the temperature gradient within the molten pool, which is important for mitigating residual stress.

Lower scanning speeds result in larger molten pools, longer cooling duration, and slower cooling rates. As a result, residual stress is reduced. Hussein et al.[141] explored the impact of scanning speed on melt pool dimensions and temperature gradient along scan track in L-PBF fabrication of 316L stainless steel (Fig. 11a). They found that the melt pool length increases with scanning speed. Conversely, the melt pool's width and depth decrease with increased scanning speed, which reduces the time needed for the molten track to cool and solidify (Fig. 11b-d).

In another study, Loh et al.[142] combined the effects of scanning speed and laser power to observe their effect on molten size by measuring and comparing the volume of molten and solidified powder (Fig. 11e-g). They investigated the effects of various laser powers and scanning speeds on melt penetration and width in 316L stainless steel, correlating experimental measurements with simulated predictions. Their findings demonstrate that melt height was greater at lower power and higher scan speed, increasing with a scan speed up to a specific laser power threshold, beyond which it stabilizes. Moreover, increasing laser power and decreasing scan speed enhance melt penetration and width.

Some researchers have studied the direct effect of scanning speed on residual stress. For instance, Shiomi et al.[101] reported a decrease in residual stress magnitude with an increase in scanning speed up to a certain threshold, beyond which residual stress begins to rise again. Their study on the fabrication of chrome molybdenum steel (JIS SCM440) via L-PBF showed minimal variation in average residual stresses (ranging from 300 MPa to 400 MPa) in the top layer with changes in scan speed.

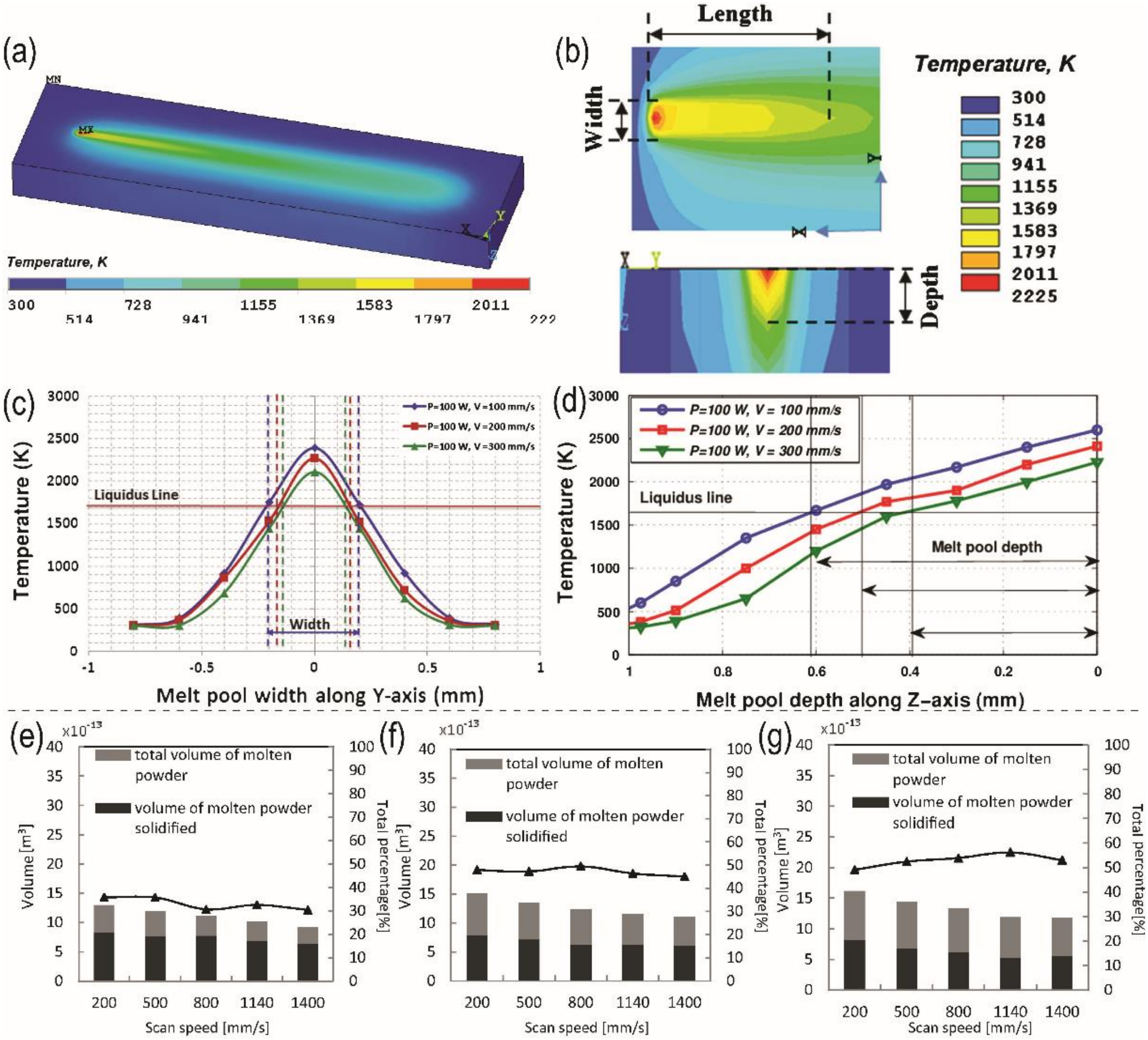

Fig. 11 a) Transient temperature distribution during layer melting at the end of the 5th track scan[141]. b) Predicted melt pool temperature contours after scanning the 5th track.[141] c) Melt pool width of various scanning speeds, and d) melt pool depth of various scanning[141]. Numerical results showing the total molten powder volume (including both solidified and evaporated portions), the solidified molten volume, and the percentage of evaporated molten powder at different scanning speeds at laser power of e) 150 W, f) 250 W, and g) 350 W[142].

In their thermo-mechanical model of L-PBF fabrication of Ti-6Al-4V, Ansari Md Jonaet et al. observed that increasing scanning speed from 750 mm/s to 1000 mm/s reduced residual stress in the fifth layer of fabrication with a laser power of 150 W from 981.23 MPa to 935.72 MPa, highlighting a decline in residual stress with increased scanning speed. This trend remained consistent at a laser power of 120 W[136].

Furthermore, scanning speed can influence the microstructure and mechanical properties of the fabricated parts. For example, Cho et al.[143] explored the AM fabrication of the Ti-48Al-2Cr-2Nb alloy. At increased scanning speeds (1600 mm/s, 2000 mm/s, and 2500 mm/s), they observed a layered microstructure perpendicular to the build direction, characterized by duplex-like regions (containing lamellar and fine grains) and a band (predominantly consisting of equiaxed grains). Notably, the highest tensile stress occurred at a scanning speed of 800 mm/s[143].

As previously mentioned, to explain the phenomenon of residual stress, understanding the properties of the molten zone and its temperature gradient is crucial. Key parameters such as laser power, scanning speed, and hatch spacing directly influence the molten pool size, which affects the thermal history of the part during the process. This plays a significant role in the generation of residual stress. Several researchers have investigated the combination of laser parameters, including those mentioned above, to study their effects on microstructure, chemical composition, mechanical properties, and residual stress. Li et al.[144] studied the effect of process parameters, including laser power, scanning speed, and hatch spacing, on the surface morphology, densification, and microstructure of tungsten samples fabricated by L-PBF. Their study presents the transition of surface morphology from porous and irregular to dense and flat as the laser power increases from 200 W to 300 W while keeping the scanning speed at 300 mm/s and hatch spacing at 0.08 mm constant[144]. Likewise, Pekok1 et al.[145] investigated the effect of laser power, hatch spacing, and scanning speed on the mechanical and internal structure properties of as-fabricated aluminum 2024 alloy (AA2024) manufactured using L-PBF. The study revealed slower scanning speeds, combined with wider hatch spaces (60 and 80 µm), resulted in lower relative porosity. The optimal surface quality was achieved at the slowest scanning speed and 80 µm hatch spacing[145]. Consequently, the need for a formula that combines and summarizes the effects of process parameters in AM leads to the formalization of energy density. Therefore, the concept of energy density was introduced by several researchers, to capture the combined effects of key parameters and provide better insight into process tuning to achieve their goal, such as improving surface quality or reducing residual stress. Researchers have proposed specific energy density formulations based on their objectives. For instance, several researchers used linear energy density (LED, E_{l}) to study the effect of process parameters on the density, microstructure, and roughness of several alloys in the AM process[146], [147], [148]. The formulation of LED is represented in Eq. (5):

$$E_{\mathrm{l}} = \frac{P}{v} \left[\frac{J}{mm}\right] \tag{5}$$

This formulation combines laser power (P) and scanning speed (v), which has been widely adopted in related studies. For instance, Wu et al.[149] suggested that increasing energy per unit length (through adjustments in laser power and speed) decreases residual stress-induced deflection upon sectioning. Zhao et al.[150] showed that higher laser power (600 W) increased residual stress in TC4/Inconel718 materials, and that residual stress decreased when lower energy per unit length was applied. Higher laser power or speed alters the substrate temperature and the heat-affected zone's size, resulting in lower residual stresses[149].

The other formulation of energy density is area energy density (AED, E_{s}), which represents:

$$E_{\mathrm{s}} = \frac{P}{hv} \left[\frac{J}{mm^2}\right] \tag{6}$$

where h is the hatch spacing. Unlike other formulations of energy density, AED has a physical meaning, representing the amount of energy obtained by the section, which is derived from laser power[29].

The most common representation of energy density is VED, which is volume energy density. In this formulation, the effect of layer thickness has been considered to provide a more comprehensive understanding of the influence of process parameters. VED can be calculated using Eq. (7):

$$E_{\mathrm{v}} = \frac{P}{thv}[\frac{J}{mm^3}] \tag{7}$$

where t is the layer thickness. In contrast to other energy densities, VED is a representation of mechanical properties, microstructure, density, and geometrical aspects of the process. Therefore, VED is widely used to quantify the effects of process parameters on the mitigation of residual stress[100], density[151], roughness[152], and surface quality[153], [154]. Researchers use volumetric energy density (VED) to study how process parameters affect residual stress mitigation. Simson et al.[155] found that doubling VED significantly increased residual stress in stainless steel 316L L-PBF samples. Vastola et al.[138] demonstrated that lower scan speeds or higher laser power expanded the heat-affected zone (HAZ), increasing residual stress profiles. Also, Bian et al.[137] set up a finite element model and an experimental analysis of stainless steel 316L fabricated by L-PBF, with two scanning strategies including stripe and chessboard (Fig. 12a, b). Their finding revealed that molten pool width increases by increasing the laser power in both scanning strategies (Fig. 12c–f). Additionally, increasing laser power increases residual stress at depth along the x-direction (Fig. 12g and 12h). In another study, Bian et al. [117] confirmed that VED can effectively represent the influence of laser power and scan speed on residual stress. Their results indicated that higher laser powers (160 W to 240 W) and slower scan speeds increased residual stress, with stripe scanning producing more stress than chessboard scanning. For instance, raising laser power from 200 W to 240 W increased residual stress from 285.8 MPa to 444.7 MPa at 800 mm/s. Furthermore, increasing scan speed from 400 mm/s to 600 mm/s reduced residual stress from 469.7 MPa to 242.7 MPa. Table 4 further supports this by showing a decrease in residual stress as energy density decreases. However, Dumontet et al.[124] found that energy density values with different process parameters led to different residual stress levels, suggesting that VED may not be a reliable tool for stress comparisons and predictions.

There are some articles in which the simulation of the AM process and optimization of process parameters to reduce the residual stress were performed considering the VED. Panda and Sahoo[156] developed a numerical finite element model to simulate the fabrication of AlSi10Mg via DMLS. They observed that increasing the laser power from 70 W to 100 W while maintaining a constant scanning speed of 100 mm/s led to an increase in the temperature of the molten pool, which in turn led to an increase in residual stress. Huo et al.[157] investigated the L-PBF fabrication of Inconel 718 alloys and identified an optimum set of parameters — laser power: 300 W, scanning speed: 1.3 m/s, and scan interval: 0.12 mm—to achieve the lowest residual stress of 294.54 MPa through simulation.

Malmelöv et al.[158] developed a thermo-mechanical model to study the effects of process parameters on the mitigation of residual stress and distortion of alloy 625 samples fabricated by L-PBF. The experimental validation was conducted using X-ray diffraction measurements. They investigated two process parameters with energy densities of 69.4 J/mm^3 (laser power: 100 W, scanning speed: 1200 mm/s) and 95.2 (laser power: 160 W, scanning speed: 1400 mm/s) with the same hatch space of 60 μm and layer thickness of 20 μm and a bi-directional scanning strategy along the *y*-axis. They found no significant trend in the residual stress between the two sets of parameters, suggesting that the range of parameters was not wide enough to demonstrate the impact of process parameters[158].

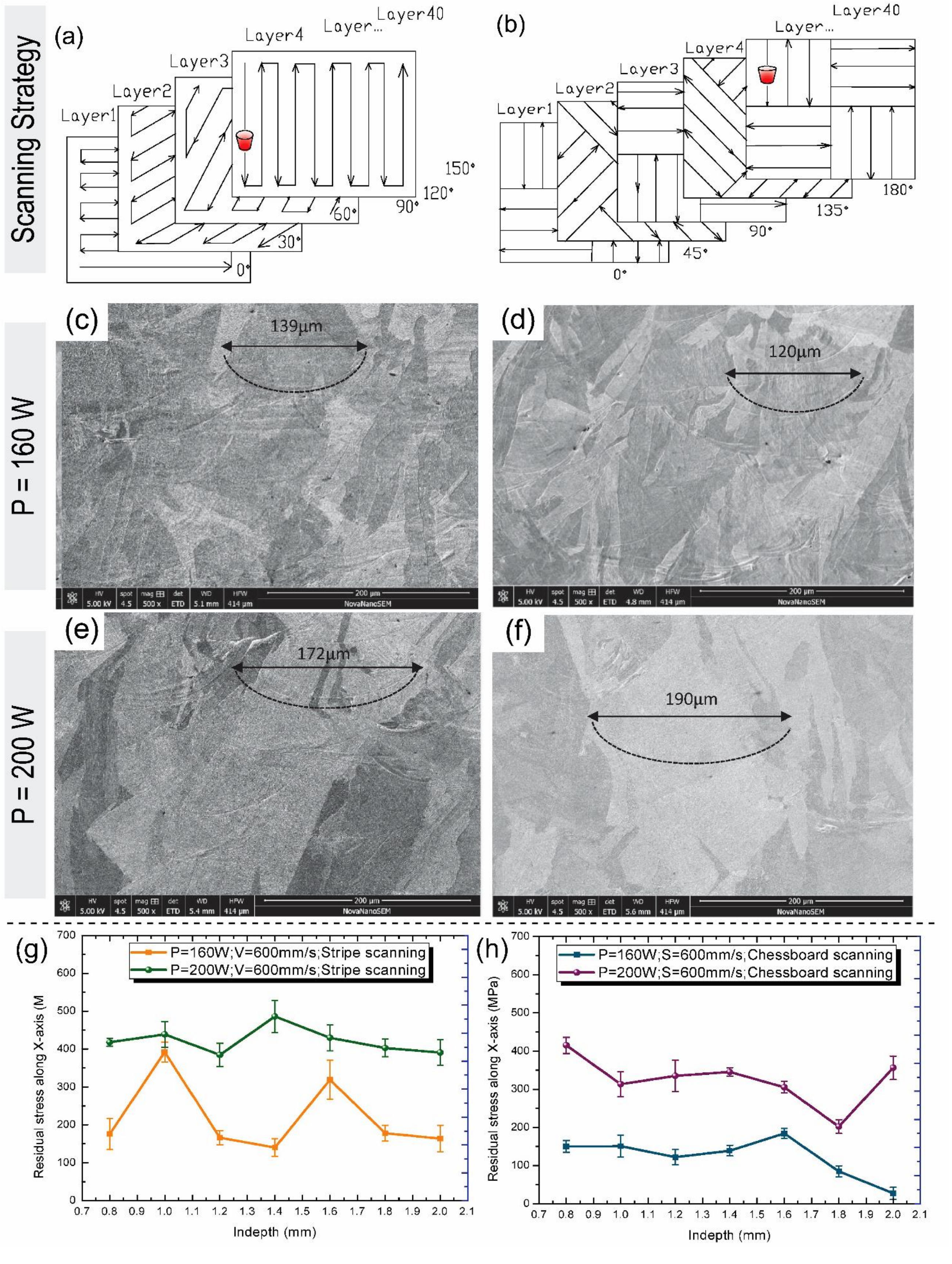

Fig. 12 Size of molten pool formed by L-PBF by two different scanning strategies[137] : a) stripe scanning strategy and b) chessboard (island) scanning strategy. Molten pool size in different L-PBF process parameters[137]: (c) *P* = 160 W, stripe scanning; (d) *P* = 160 W, chessboard scanning; (e) *P* = 200 W, stripe

scanning; (f) $P = 200$ W, chessboard scanning. Effect laser power in-depth residual stress with different laser power of $P = 160$ W and $P = 200$ W, constant scanning speed and two scanning strategies[137]: (g) stripe scanning; (h) chessboard scanning.

Table 4 The value of energy volume density for different laser power and scanning speeds and its corresponding value of molten pool size and residual stress[117]

Sample	Power (W)	Scanning speed (mm/s)	Scanning strategy	Energy density	Molten pool size (μm)	Residual stress (MPa)
1	160	400	Striped	56	122 × 60	469.7
2		500	Striped	45	112 × 45	242.7
3		600	Striped	37	100 × 40	199.3
4	200	400	Chessboard	56	115 × 35	405
6		600	Chessboard	37	100 × 38	122.6
9		600	Chessboard	46	125 × 35	324.4

Researchers often use VED to optimize process parameters not only for residual stress mitigation, but also for improving mechanical properties. Ravichander et al.[159] studied Inconel 718 parts in L-PBF and found that increasing energy density affects phase composition, potentially transforming Inconel 718 into thermally stable δ phases, and can also cause height deviations in the built part due to deeper melt pools. In Fig. 13, the optimal processing region of the laser power and scanning speed for obtaining the best mechanical properties of Inconel 718 is depicted.

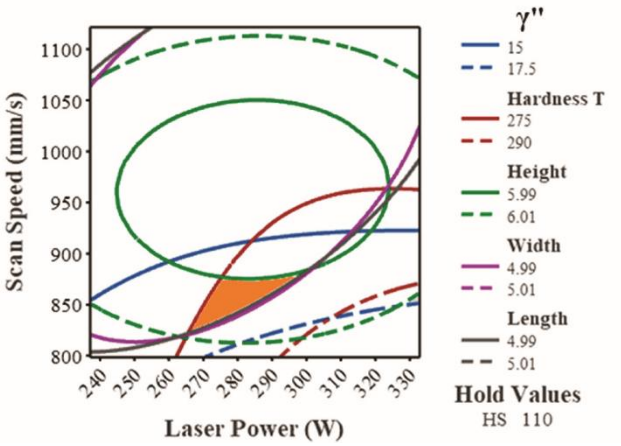

Fig. 13 Contour plot showing the optimal processing region of the laser process parameters for obtaining the best mechanical properties of Inconel 718 parts fabricated by L-PBF [159].

Liverani et al.[160] achieved over 98% density in 316L stainless steel using an energy density of 100 J/mm^3. Bang et al.[161] demonstrated that higher energy density (9.34 J/mm^3) is required to achieve 99.5% density in SUS316L, with increased energy reducing lattice distortion and residual stress. Tatiana Mishurova[162] observed in Ti-6Al-4V that lower energy densities led to higher residual stress, with 53.04 resulting in residual stress around 800 MPa, while higher energy density (291.74 J/mm^3) significantly reduced residual stress.

Overall, higher laser power or speed alters the substrate temperature and the size of the heat-affected zone, which may result in lower residual stresses. Although the energy density formula does not have mathematical proof, it can illustrate the relationship between several parameters and how the small changes in each can alter differences in the stability of the molten pool, mechanical properties, and residual stress.

Scanning strategy refers to the pattern, path, or sequence in which the laser travels over the build platform to melt the metal powder. This process parameter is one of the key parameters, along with laser power, that influences the thermal gradient, cooling rate, and residual stress during the fabrication process. To illustrate, consider a unidirectional scanning strategy (Fig. 14a). In this approach, when the laser reaches the end of the platform, it changes its direction and returns to the starting point of the platform to start the melting process. Conversely, in a non-unidirectional strategy, the laser starts the next track at the end of the previous one. Therefore, the temperature gradient generated by both scanning strategies will be different. Each scanning strategy generates a distinct temperature gradient and distribution based on its pattern, leading to residual stress within the part. The common used scanning strategies are depicted in Fig. 14.

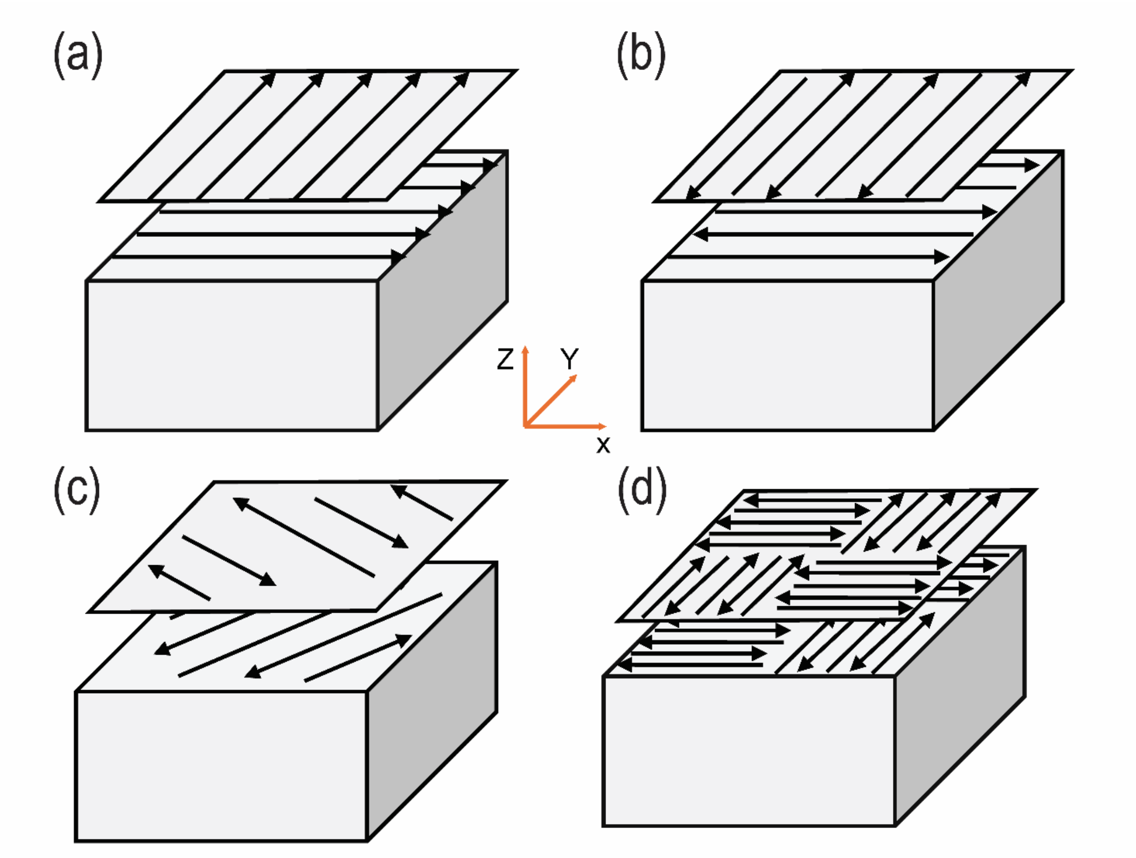

Fig. 14 The common scanning strategies used by researchers: a) unidirectional, b) un-unidirectional, c) ° rotation, and d) island scanning

These scanning strategies affect the temperature gradient, and the location of the affected zone in the plate also influences the distribution of residual stress. Various scanning strategies have been studied to assess their effect on the mitigating and distribution of residual stress.

As mentioned, the choice of scanning strategy influences the anisotropy of stress fields within individual layers. Parry et al.[57] observed that while the maximum stress magnitude was not affected by the choice between unidirectional and alternating scanning methods (Fig. 15a and 15b), the distribution of stress within the part was influenced (Fig. 15c-h).

Parry et al.[57] also demonstrated that reducing scanning path lengths and altering scanning direction can reduce and balance residual stress in L-PBF Ti6Al-4V samples. Jia et al.[163] explored the impact of different scanning strategies on the thermomechanical properties of Ti-6Al-4V fabricated via the L-PBF process. They analyzed three scanning strategies: the outer spiral, inner spiral, and Z-shaped strategies. Their findings revealed that the Z-shaped scanning strategy presented the highest residual equivalent stress (936 MPa) at the endpoint of the scanning path. By contrast, the peak residual equivalent stress for the outer spiral strategy was reported at 1551 MPa at the beginning of the scanning path. The inner spiral strategy saw its maximum residual equivalent stress at 762 MPa, located near the start of the scanning path. The inner spiral strategy was determined to present the most uniform distribution of equivalent residual stress. However, the Z-shaped scanning strategy and the outer spiral illustrated the least uniform field of equivalent residual stress[163].

Bian et al. [137] investigated the L-PBF fabrication of stainless steel 316L at a scanning speed of 600 mm/s, using two different scanning strategies (Fig. 15l and m). They understood that the cheeseboard strategy's residual stress is more in-depth than that of the stripe scanning strategy.

Researchers also analyzed specific scanning strategies. For example, Li et al.[164] developed the finite element method for thin-walled parts undergoing the AM process to examine the effect of path strategies depicted in Fig. 16a-c, including same direction motion (SDM), reciprocating motion (RM), and segmental reciprocating motion (SRM). Furthermore, the results were validated by X-ray diffraction measurement. They observed that different path strategies resulted in various stress contours (Fig. 16). For example, the SDM path strategy displayed non-uniform stress, whereas the RM path strategy led to a more uniform stress distribution. The SRM path strategy resulted in lower residual stress in specific areas, especially along line BC, compared to SDM and RM. Longitudinal stress along DE line in Fig. 16m showed a higher peak for SRM, indicating localized stress concentration. Transversal stress along FG line in Fig. 16n revealed significant boundary peaks for SRM, suggesting higher stress accumulation at edges. Normal stress along HI remained stable for SDM and RM, while SRM exhibits more fluctuations. These results highlighted the SRM's success in stress reduction but also indicated potential for concentrated stress peaks. Further optimization may be required to minimize stress accumulation at boundaries when using SRM[164].

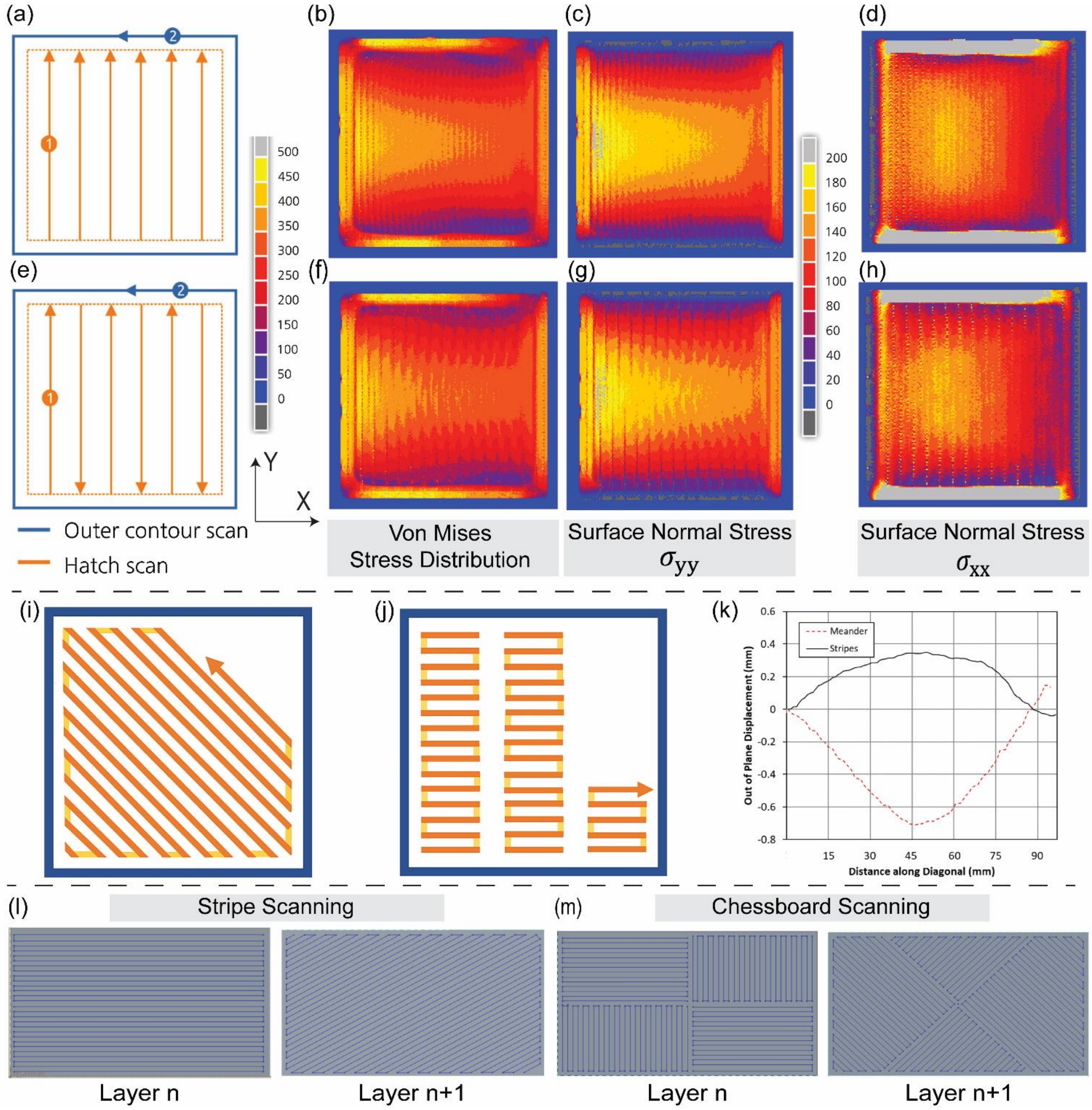

Fig. 15 a) Unidirectional scanning strategy. Profiles views of b) von Mises stress, c) surface normal stresses in y direction, and d) surface normal stresses in x direction for 3 mm × 3 mm test case when using unidirectional scanning strategy. e) Alternating scanning strategy. Profiles views of f) von Mises stress, g) surface normal stresses in y direction, and h) surface normal stresses in x direction for 3 mm × 3 mm test case when using alternating scanning strategy. The schematic of scanning strategies used by Patterson[36] : i) meander, j) stripes. k) Z-measurements from digital image correlation (DIC) along a diagonal of two test plates[36]. Different scanning strategies investigated by Peiying Bian[137] : l) stripe of 0° and 30° rotation, m) chessboard of 0° and 45°.

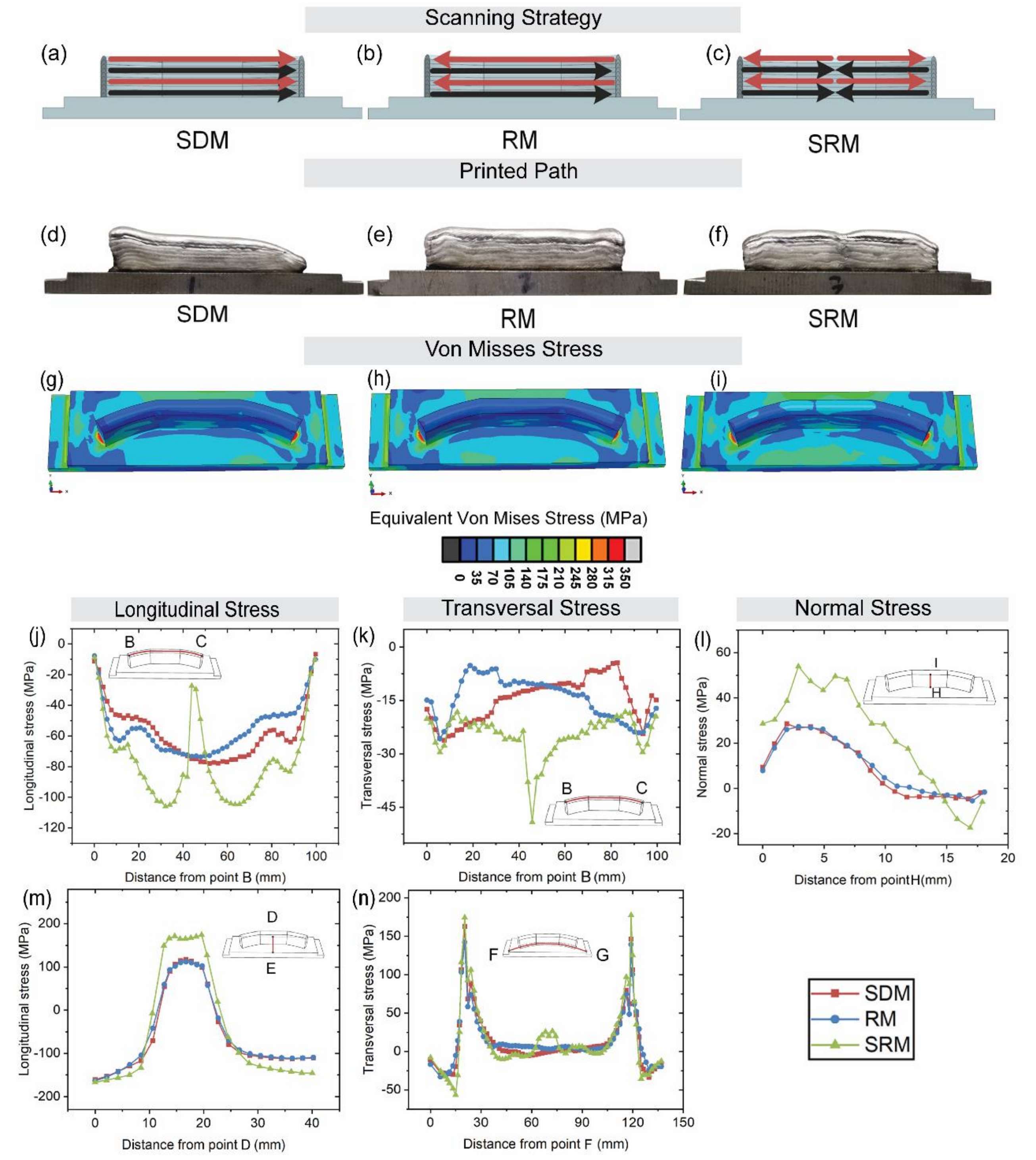

Fig. 16 Scanning strategies used in deposition and corresponding printed samples, von misses stress and stress analysis along different lines of the component[164] . Scanning strategies: a) SDM, b) RM, c) SRM. Printed sample by scanning strategies: d) SDM, e) RM, f) SRM. Contour of equivalent von mises stress for different scanning strategies: g) SDM, h) RM, i) SRM. Residual stress distribution along line BC in different scanning strategies: j) longitudinal stress, k) transversal stress. l) Normal stress distribution along line HI in different scanning strategies. m) Longitudinal stress distribution along line DE in different scanning strategies. n) Transversal stress distribution along line FG in different path strategies[164].

In Finite Element Method (FEM) simulations conducted by Cheng et al.[165], various scanning strategies (Fig. 17) were analyzed using Inconel 718, with a scanning speed set at 1000 mm/s and a laser power of 600 W. Temperature distribution plots, residual stress in the x- and *y*-directions for all scanning strategies are illustrated in Fig. 17. The simulations revealed that scanning along a 45° inclined line reduces deformation and in-plane residual stress. Similarly, the findings were confirmed by the FEM simulations conducted by Cheng et al.[165].

Zhang et al.[166] studied twelve different scanning strategies (Fig. 18) in multi-laser beam Powder Bed Fusion technology, setting up a 3D coupled thermomechanical model for Ti-6Al-4V. They described the 'S' scanning strategy as one in which the laser changes its scan direction after completing each track. Zhang reported that the parallel 'S' strategy without rotation generated a residual stress of 900.57 MPa, significantly reducing the maximum stress. Furthermore, applying a 90° rotation to the parallel 'S' strategy between layers was found useful in reducing residual stress and improving its uniformity. Moreover, a scanning technique involving a 45° rotation of the approaching beam resulted in the second-lowest residual stress level among all tested strategies (Fig. 18). Zhang also noted that the delayed scanning strategy produced the lowest average principal stress among all scanning strategies, at 772.30 MPa. Furthermore, residual stress mitigation in the edge regions of islands was higher than in their central zones[166].

Zou et al.[167] developed a 3D thermomechanical model for Ti-6Al-4V during L-PBF to analyze residual stress, examining 18 scanning strategies. Although increasing the number of lasers did not significantly reduce average stress, their findings highlighted the importance of scan sequence and sweeping direction in achieving a more uniform residual stress distribution.

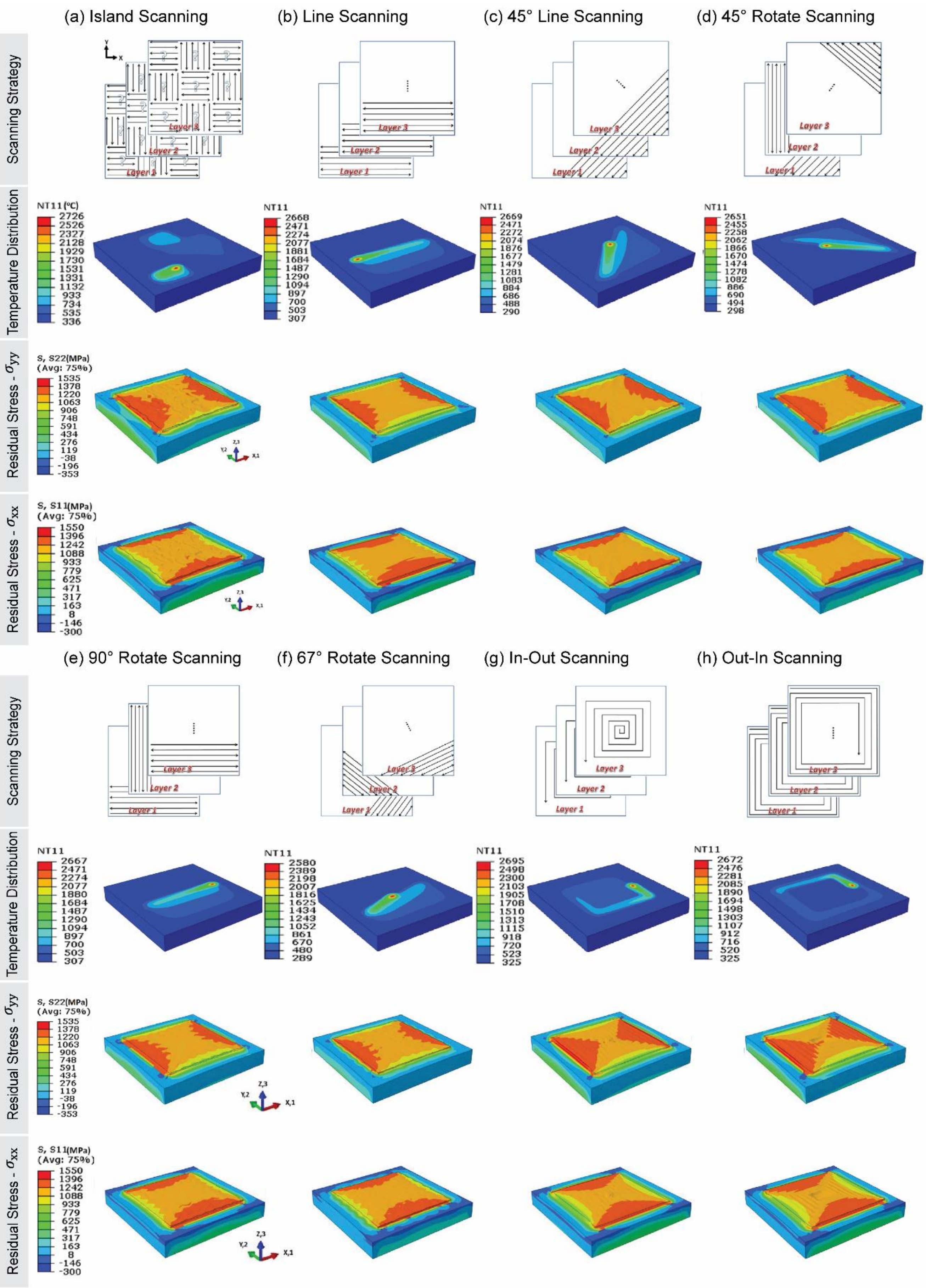

Fig. 17 Scanning strategies used by Cheng et al.[165] in the investigation of L-PBF fabrication of

Inconel 718 and their corresponding temperature distribution, residual stress in *y*-direction, and residual stress in *x*-direction: a) island scanning, b) line scanning, c) 45° line scanning, d) 45° rotate scanning, e) 90° rotate scanning, f) 67° rotate scanning, g) in-out scanning, h) out-in scanning.

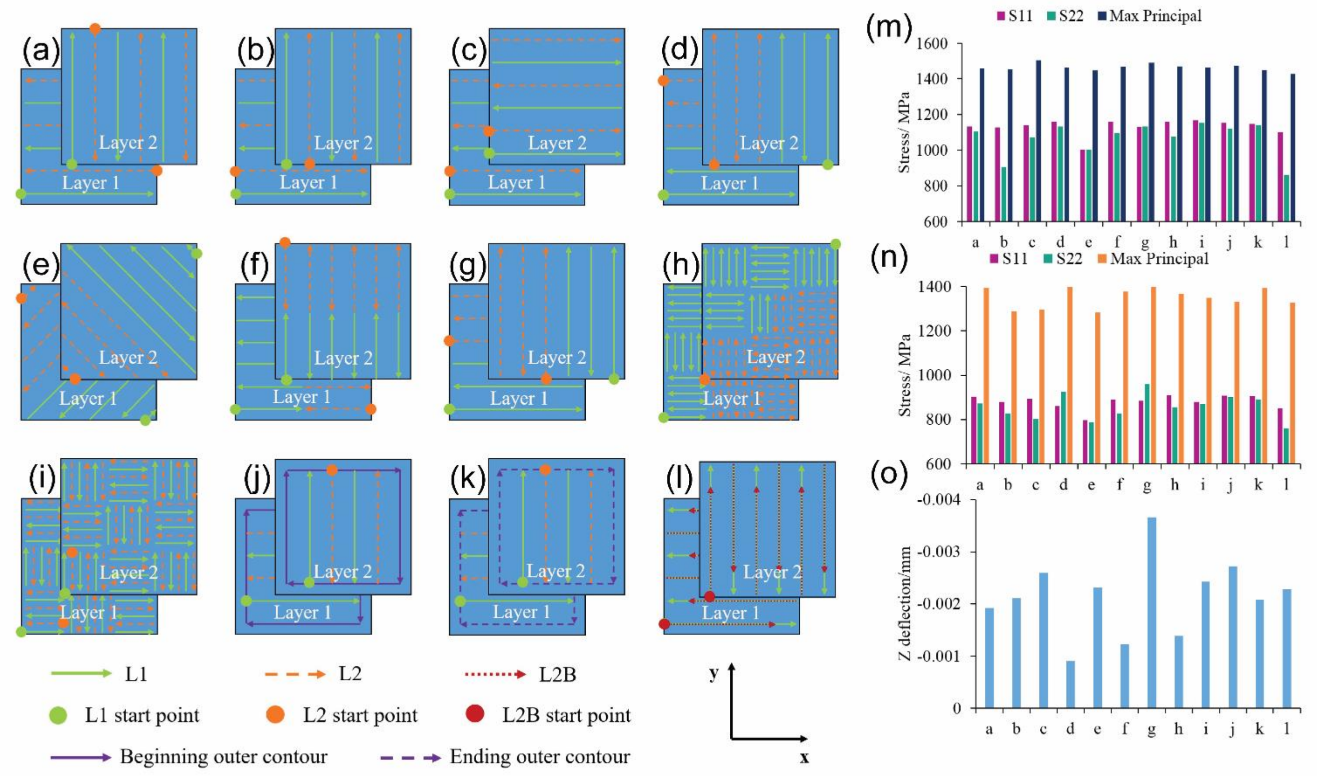

Fig. 18 Twelve different scanning strategies that Zhang et al. used in[166]: a) opposite S scanning, b) parallel S 90° scanning, c) parallel S no rotation scanning, d) 0 approaching beam scanning, e) 45° rotation approaching beam scanning, f) opposite halves scanning, g) parallel halves scanning, h) island approaching beam scanning, i) island mixed scanning, j) beginning contour fill, k) ending contour fill, and l) delayed laser scanning. m) The value of final average residual stress for each scanning strategy before releasing base plate constraints (S11, S22 and maximum principal stress and n) the value of final average residual stress for each scanning strategies releasing constraint (S11, S22 and maximum principal stress), and o) the value of deflection in *z*-direction occurred in each scanning strategies after releasing base plate constraints[166].

Zhan et al.[168] employed six scanning strategies to measure residual stress in Ti-6Al-4V parts fabricated by LAM (Fig. 19). The highest longitudinal stress was observed in the line spacing strategy (281.4 MPa), while the island strategy showed the lowest stress in both longitudinal (124.6 MPa) and transverse directions (31.1 MPa). These findings are illustrated in Fig. 19a-f.

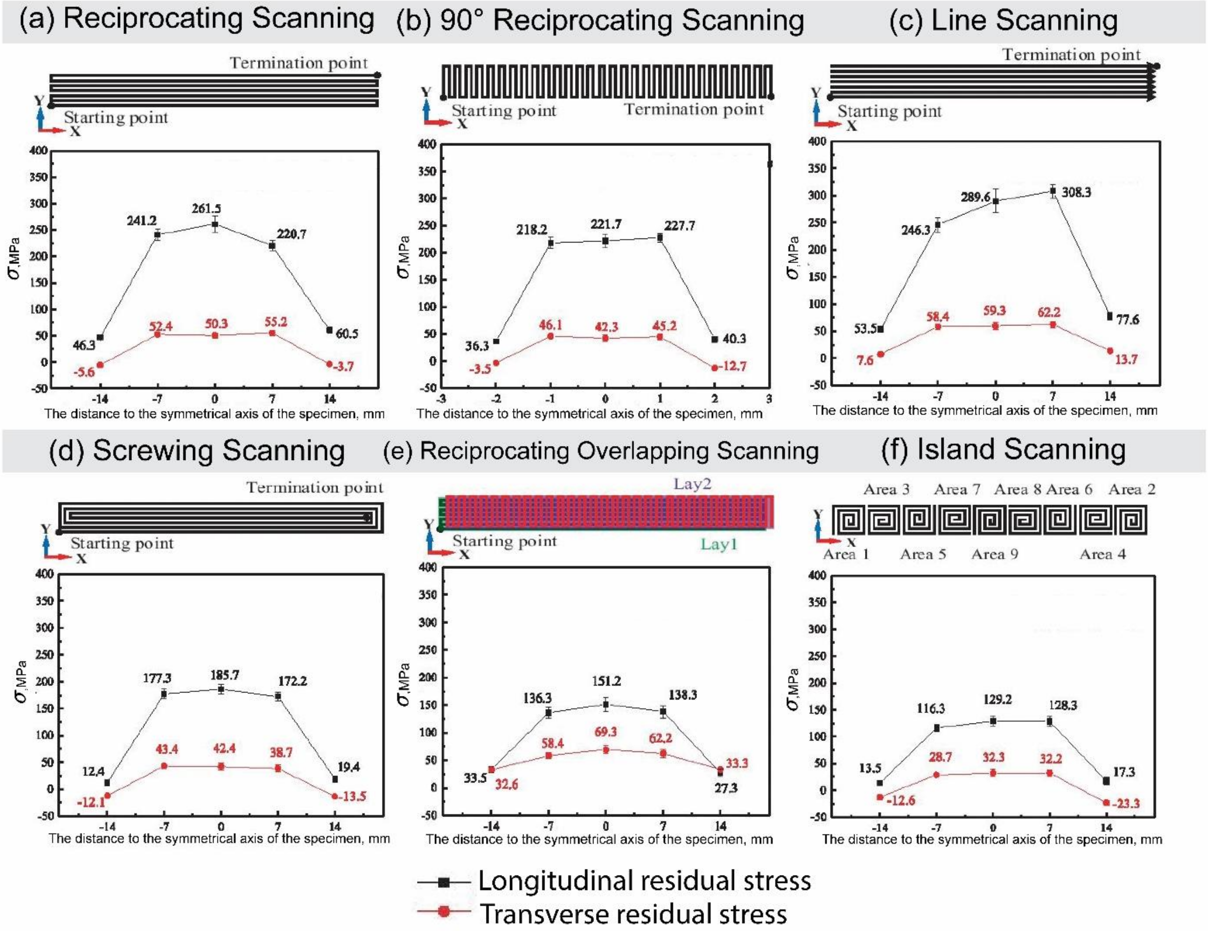

Fig. 19 The scanning strategies and the relative longitudinal and transverse residual stress investigated by Zhan et al. [168] : a) reciprocating scanning, b) 90° reciprocating scanning, c) line spacing, d) screwing scanning, e) reciprocating overlapping scanning, and f) island scanning.

Zhang et al.[169] studied six scanning strategies (Fig. 20) applied to Ti-6Al-4V plates using X-ray diffraction. Scanning strategies incorporating inclination angles led to more uniform stress distributions, with the 45° rotation strategy reducing stress by 46.23% compared to the island strategy (Table 5, Fig. 20).

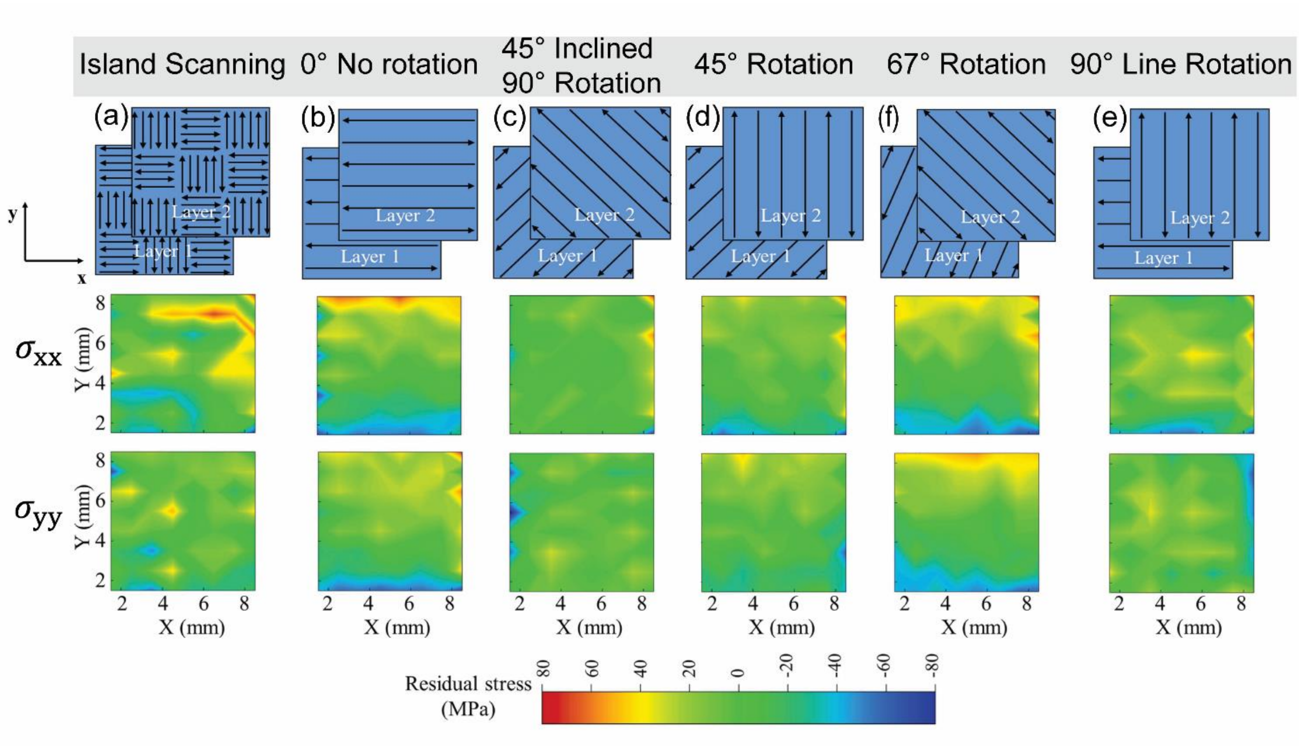

Fig. 20 Analyzing the effect of scanning strategy on residual stress by Zhang et al.[169], six scanning strategies and their corresponding experimental results of stresses in *x*-direction and *y*-direction are represented: a) island scanning, b) 0° no rotation, c) 45° inclined 90° rotation, d) 45° rotation, e) 90° line rotation, f) 67° rotation.

Table 5 Results for the residual stress obtained for different scanning strategies in PBF-LB fabrication Ti-6Al-4V by Zhang et al. [169]

Scanning strategy	Maximum σ_{xx} stress (MPa)	Stress reduction compared to island strategy (%)	Thickness (mm)
45° Rotation	37.02	46.23	1
90° Line Rotation	40.32	40.79	1
0° No rotation	68.10	1	1
Island scanning	68.85	-	1
45° Rotation	55.75	22.19	3
Island scanning	71.65	-	3
0° No rotation	76.40	-6.6	3

Serrano-Munoz et al.[170] compared two scanning strategies, Y-scan and Rot-scan, for L-PBF-produced Inconel 718 alloy parts. X-ray diffraction revealed that the Y-scan produced lower stress in the build direction, while the Rot-scan exhibited higher surface stress of approximately 400 MPa. Rotating scanning strategies, such as a 67° rotation, led to more uniform stress distribution.

Mugwagwa et al.[171] analyzed four scanning strategies—island, successive, successive chessboard, and LHI— in the L-PBF processing of tool steel. The successive chessboard strategy reduced residual stress by up to 40% compared to the island strategy, achieving the lowest average residual stress of 209 MPa with a laser power of 170 W and scanning speed of 1200 mm/s.

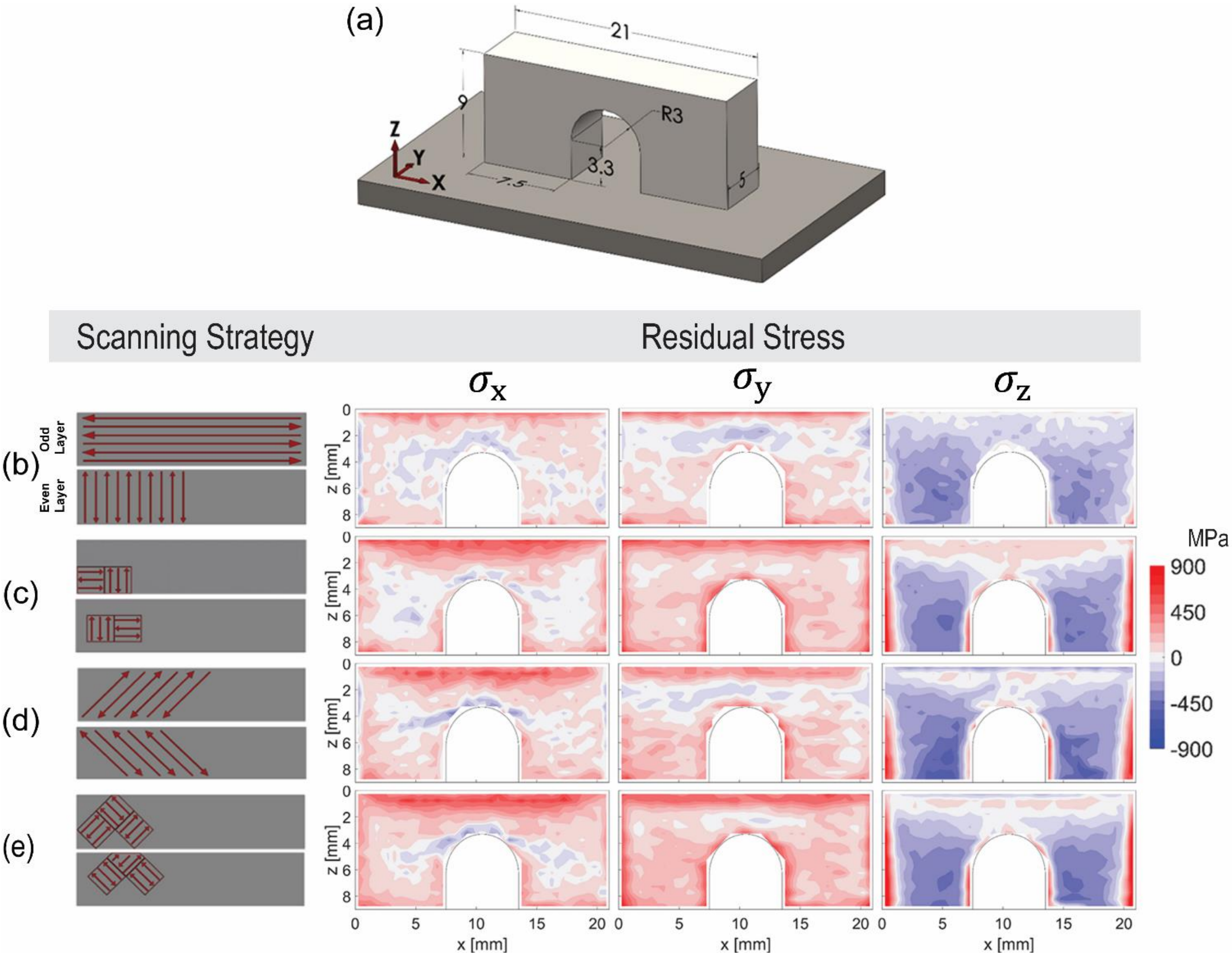

Fig. 21 Scanning strategies and relative stress maps over the investigated mid-plane of the sample used by Strantza et al.[172] in L-PBF fabrication of Ti-6Al-4V: a) schematic of the sample, b) continuous, c) island d) parallel e) island offset by 45°. Four scanning strategies and relative.

Strantza et al.[172] investigated scanning strategies as depicted in Fig. 21 for Ti-6Al-4V fabricated by L-PBF using high-energy X-ray diffraction. They found that continuous scanning effectively reduced residual stress, especially when combined rotations between layers. Shorter scan lengths led to higher stress due to rapid cooling, as shown in Fig. 21.

Furthermore, Yadroitsev and Yadroitsava[173] found that residual stress in stainless steel and Ti-6Al-4V samples fabricated through L-PBF was more significant along the beam scanning direction.

Certain scanning techniques can be combined to create additional patterns, such as a rotating island scanning pattern that incorporates alternating vector directions, often incorporating translational displacement of the pattern between layers. Island scanning, which divides each layer into smaller sections, has been shown to significantly lower residual stress compared to full-length scans[66], [174], [175]. Kruth et al.[176] noted that optimal scanning modes can significantly decrease thermal distortion. Wu et al.[149] recommended using 3×3 mm^2 islands for 316L stainless steel parts to reduce tensile residual stress. Lu et al.[175] found that a 5×5 mm^2 island size resulted in lower residual stress for L-PBF Inconel 718 parts. Smaller islands sizes resulted in the lowest RS, whereas larger islands exhibited inconsistent effects on RS.

Sarma et al.[177] found that increasing the island size in a hexagonal scanning strategy in fabricating 17-4 PH stainless steel using L-PBF resulted in larger residual stresses due to longer scanning tracks and a diminished pre-heating effect. However, further reductions in vector length within these islands have yielded mixed results. For instance, Simson et al.[155] and Robinson et al.[178] found that smaller island sizes increased RS.

In AM, the interaction between stress fields and ongoing cooling across layers significantly impacts stress distribution in subsequent layers. A study reported a 37.5% reduction in distortion by rotating the full-length raster 67° between layers, emphasizing the critical role of beam scanning strategy in influencing orientation, uniformity, and magnitude of the stress field. The scanning approach directly affects in-plane RS anisotropy on single and multiple-layer levels while limiting stress/strain in the build direction[149]. Nadammal et al.[179] explored the fabrication of Inconel 718 via L-PBF, utilizing four distinctive scanning methods (Fig. 22b-e). Two strategies involved scanning each layer independently, which resulted in distinct patterns and promoted the formation of elongated, columnar metal grains. An alternative strategy that merged the individual layer techniques yielded a finer metal structure with diminished stress. However, applying 67° rotation between layers demonstrated an innovative approach to achieving better metal structure and mitigating residual stress (Fig. 22). Based on Fig. 22, their findings indicated that the X-strategy induced relatively high residual stress values and stress gradients, whereas the Rotational Strategy was most effective in minimizing residual stress and producing symmetric stress gradients[179]. In Table 6, the results obtained by Nadmmal et al. are presented.

Hajnys et al.[180] investigated the effect of various scanning strategies, pre-heating, and laser power in L-PBF fabrication of stainless steel 316L. Their findings revealed that laser power plays a more dominant role than other parameters. They mentioned that a laser power of 300 W led to the lowest curling angle.

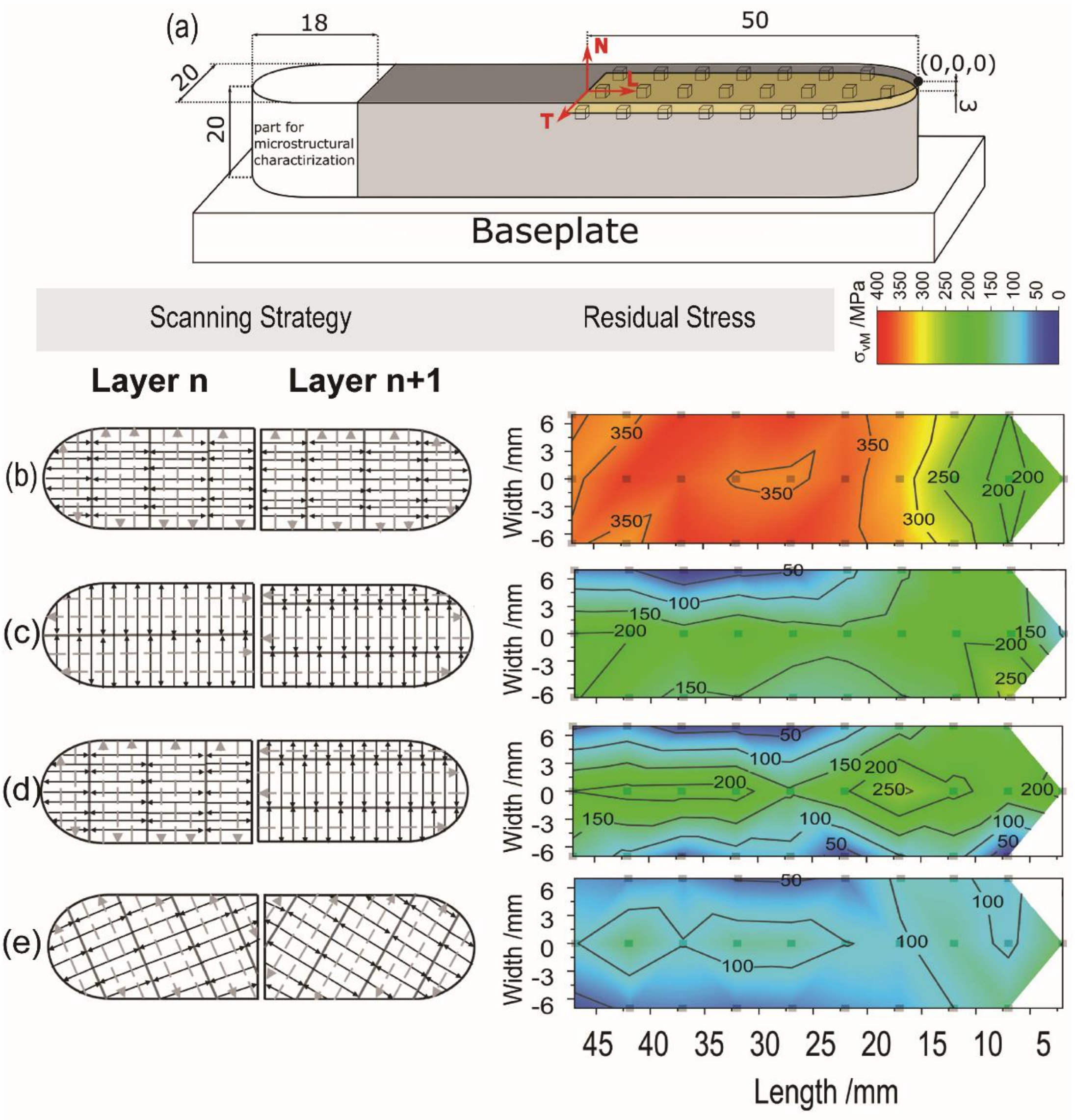

Fig. 22 Von Mises equivalent stresses in the top surface for the sample tested by Nadammal et al.[179]: a) the schematic of the sample, b) X-, c) Y-, d) alternating, and e) rotational strategy. The error is $\delta\sigma \leq 50$ MPa.

Table 6 Effect of different scanning strategies on the Inconel 718 via Laser Powder Bed Fusion (L-PBF) investigated by Nadammal et al. [179]

Strategy	Description	Impact on microstructure	Residual stress and stress gradients
X-strategy	Localization of fabrication stages with a short hatch length, melting a small volume of material at a time	Induces significant anisotropy	This leads to relatively high residual stress values and stress gradients
Y-strategy	90º rotation of scanning and hatching directions	Develops a different microstructure, absence of rotated cube component of texture	Implies a unique grain growth pattern that could affect stress
Alternating strategy	Alternates between different scanning strategies layer by layer	This leads to microstructure and texture like rotational strategy but with less prominent random grains	There is an intermediate amount of residual stress; the successive layer modifies the effects

Rotational strategy	Rotates scanning direction for each successive layer	Creates a microstructure with random grains due to complex thermal fields, disrupting the previous layer's deposition	Generates the least amount of residual stress and symmetric stress gradients

Several aspects of interaction of process parameters with residual stress within the component in the additive manufacturing process have been reviewed. Moreover, some factors still contribute to formation of stress fields, distortion, and mechanical inaccuracy in the produced parts, which are mainly analyzed together or in interaction with other parameters. For instance, the mechanical substrate can be critical in forming residual stress by imposing mechanical constraint and acting as a heat sink. The substrate functions as a solid cooling channel, which helps with heat dissipation. Its size, thickness, and design also affect the stress concentration and stiffness of the component. Reducing substrate stiffness by decreasing the size of the substrate results in reduction of the components' residual stress[181]. Gülcan et al.[182] reported that a thicker SAE304 substrate reduces heat accumulation and thermal gradient and increases resistance to residual stress formation during L-PBF. In some research, innovations in the design of substrate by introducing in-depth patterned grooves have been proven to be effective in the mitigation of residual stress as maximum tensile stress from 1600 MPa was reduced approximately by 50% in a new design and provided crack-free T-shape and bridge parts in L-PBF[183]. The effect of substrate stiffness is a matter of interest in studying other AM processes like DED. Lu et al.[181] investigated the optimal design for the substrate to reduce residual stress and maximum temperature gradient during DED fabrication of Ti-6Al-4V components. Their findings reported that hollow substrate reduces heat flow, and leads to a 62% reduction of maximum tensile residual stress in comparison to the solid and rectangular substrate.

During fabrication using metal AM techniques, when the laser moves from region to region without melting, it is called a “laser jump”, as shown in Fig. 23. This tactic plays a crucial role in forming residual stress but it has not received much attention due to the emphasis on scanning speed. Chen et al.[184] investigated the influence of laser jumping and its speed, alongside varying scan lengths, on the thermal distribution and resulting thermal stress in Ti-6Al-4V fabricated by L-PBF through 3D-thermomechanical numerical modelling. The study revealed that the speed of the laser jump had more impact on stresses perpendicular to the scanning direction rather than stresses parallel to the scanning direction. They found that increasing laser jump speed decreased residual stresses parallel to the scanning direction. On the other hand, residual stresses perpendicular to the scanning direction decreased when the laser jump changes from 200 mm/s to 1000 mm/s. Meanwhile, they obtained the opposite behavior when the laser jump speed was increased from 1000 mm/s to 10000 mm/s. Furthermore, when laser jump speed remained constant, the residual stress component parallel to the scanning direction surpasses that of the perpendicular component.

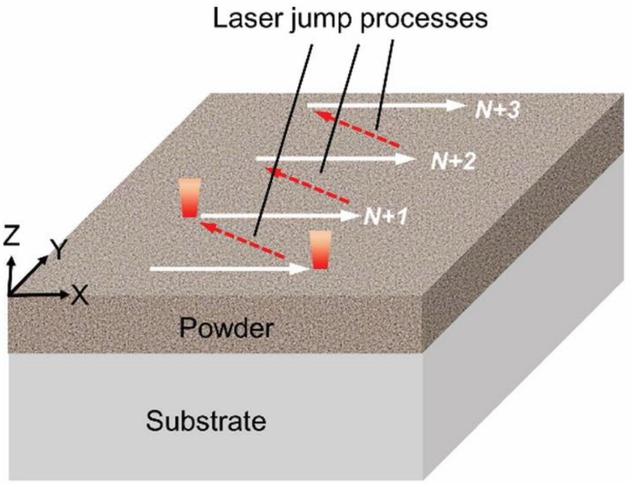

Fig. 23 Representation of laser jumping [184].

Pre-scanning and post-scanning have proven effective in mitigating residual stress during fabrication. Pre-scanning is a technique in which a certain region of powder is pre-heated to achieve a less intense temperature gradient before melting. Post-scanning involves passing a laser over a certain zone for a second time, so the residual stress formed by rapid solidification released. Kruth et al.[127] and Mercelis and Kruth[185] suggested that post-scanning could reduce part distortion by 8%, while pre-scanning could achieve a 6% reduction. Moreover, employing a post-scanning strategy with half the energy used for melting resulted in a remarkable 30% decrease in residual stress value. Luo et al.[186] developed an in-situ method for analyzing Ti-6Al-4V fabricated by L-PBF, employing a nano-indenter to measure residual stress across varying sheet thicknesses. Their findings indicated that residual stresses in specimens subjected to rescanning exhibited 33.5% to 38.0% lower than those of non-rescanned counterparts. Moreover, it was found that re-scanning is more effective in thicker sheet layers as the residual stress decreases with increasing sheet thickness.

Using a secondary laser beam with higher power rather than the main one, known as a dual laser beam technique, has been proven effective in reducing residual stress formation. Zhang et al.[187] investigated the effects of three different dual laser beam strategies with various laser powers: pre-heating, parallel heating, and post-heating on the cooling rate and residual stress mitigation of Ti-6Al-4V components fabricated by L-PBF. All three strategies were promising in achieving a more uniform thermal distribution. The post-heating configuration was the most effective technique to reduce residual stress by achieving a 10.41% compared to a single laser beam (from 1307 MPa to 1171 MPa). Furthermore, the higher secondary laser power results in better residual stress mitigation, with 90 W secondary laser power resulting in 1171 MPa. Other research by Heeling et al.[188] demonstrates a reduction in residual stress, better surface finish, and higher density in L-PBF fabrication of stainless steel 316L. Their findings reveal that the post-heating strategy homogenizes the temperature field and reduces the thermal gradient around the melt pool. Furthermore, post-heating techniques achieve 20–30% lower residual stresses, 50–70% smoother surfaces, and near-full density. Furthermore, the study revealed that the vertical post-heating strategy reduced the equivalent stress from 846.36 MPa to 655.48 MPa (22.55% reduction) in the L-PBF process of Ti-6Al-4V supports the effectiveness of dual laser beam in mitigation of residual stress[189].

Liu et al.[66] discovered that reducing the scan vector length from 42 mm to 18 mm reduced residual stress by over 50% at specific locations within the L-PBF part. Parry et al.[57]

observed a 28% reduction in von Mises stress when the scan vector length was shortened from 3 mm to 1 mm. Matsumoto et al.[190] demonstrated that shorter scan vectors reduced distortion.

Wu et al.[149] conducted experiments to understand the effect of process parameters on stainless steel 316L fabricated by L-PBF, using digital image correlation and neutron diffraction methods for residual stress measurement. They investigated different scanning island dimensions (3×3, 5×5, and continuous scanning strategies) and laser powers (100 W, 250 W, 400 W) and scanning speeds (400 mm/s, 1500 mm/s, 1800 mm/s) with various energy densities. Their results showed that reducing island size from 5×5 mm^2 to 3×3 mm^2 decreases tensile residual stresses, supporting findings that shorter scan vectors reduce residual stresses. Moreover, they discovered that shorter scan vectors result in lower residual stress and affect in-plane residual strains. This leads to decreased residual stresses with 45° off-axis scanning, positioning thermal stress in less critical locations relative to part structures[149].

Reviewing research reveals the importance of several process parameters in AM in forming, controlling, and mitigating residual stress. Direct modifications to energy input (such as beam power, scan speed, and scan vector length) and changes affecting thermal conditions (like pre-heating and pre-/re-scanning), or indirect modifications (including geometry, dwell time, and layer thickness) can significantly alter RS magnitude by modifying heat transfer conditions and cooling rates. However, optimizing these parameters involves tradeoffs between build cost, time, and quality. Finite element analysis to predict residual stress formation and adjust the parameters to reduce stress requires high-performance computers, which are costly and time-consuming. Applying efficient scanning strategies brings complexity to the production setup. Taghian et al.[29] reported that although scanning strategies such as island and chessboard alleviate residual stress, they add complexity to fabrication and reduce production efficiency. As discussed, increasing laser power will diminish residual stress. However, the range is typically between 100 W and 400 W due to the risk of material vaporization and energy cost. It is possible to reduce the built rate by doubling the scanning speed, but at the same time, there is a risk of incomplete melting cycles, which results in several defects in the final component. Furthermore, using real-time monitoring equipment such as thermal cameras and melt-pool analyzers to capture data enable researchers to optimize the process parameters to enhance mechanical properties but raise the expense during production[29].

Table 7 summarizes the key findings from researchers who investigated the effects of process parameters on the mitigation of residual stress, dimension of the molten pool, and mechanical properties of fabricated parts.

Table 7 Summarizing the researchers' work on investigation of effect of process parameters on residual stress, molten pool and mechanical properties of materials

Material	Fabrication Process	Parameter	Effect	Laser Power	Measurement Methods	Results	Reference
Ti–6Al–4V	DED	Dwell time	↑	Vary (2000 W, 1000 W , 1333 W , 2000 W , 3000 W)		Mitigation of residual stress by allowing more even cooling.	[120]
Inconel 625, Stainless Steel 316L	DED	Dwell time	↑	-	-	Pausing between layers increases bending and stress at top and edges of the part.	[125]
Co-based stellite SF6 alloy	DED	Dwell time	↑	1100 W, 800 W	Micro-analytical test / Optical and scanning electron microscopes	Increasing delay time increases residual stress due to larger temperature gradients.	[121]
Inconel 625	DED	Dwell time	↓	2000 W	Hole-drilling method	Inconel 625 shows decreased residual stress with longer dwell times due to different	[122]

Material	Fabrication Process	Parameter	Effect	Laser Power	Measurement Methods	Results	Reference
						responses to heat and phase transitions.	
Ti-6Al-4V	DED	Dwell time	↑	2000 W	Hole-drilling method	Ti-6Al-4V shows increased residual stress with longer dwell times due to different responses to heat and phase transitions.	[122]
Ti-6Al-4V	DED	Dwell time	↑	100 W, 150 W, 200 W	X-ray diffraction	Increased number of parts (dwell time) leads to higher thermal gradient and residual stress.	[124]
Maraging steel	L-PBF	Layer thickness	↑	200 W	Strain Gauges	Increasing layer thickness leads to reduced residual stress due to slower cooling rate.	[126]
tool steel 1.2709 (X3NiCoMoTi 18-9-5)	L-PBF	Layer thickness	↑	200 W	Neutron diffraction	Supported the conclusion that thicker	[56]

Material	Fabrication Process	Parameter	Effect	Laser Power	Measurement Methods	Results	Reference
						layers reduce residual stress.	
Ti–6Al–4V	L-PBF	Layer thickness	↑	42 W	Bridge curvature method	Found a reduction in residual stress with increased layer thickness.	[127]
Stainless Steel 316L	L-PBF	Layer thickness	↑	100 W	Bridge curvature method	Found a reduction in residual stress with increased layer thickness.	[125]
Inconel 718	L-PBF	Layer thickness	↑	150 W	X-ray diffraction	Found higher residual stress levels in samples with thicker layers (50 µm).	[128]
Ti–6Al–4V	L-PBF	Layer thickness	↑	195 W	Surface topography analyses with a laser scanning confocal microscope	Increasing the layer thickness will result in increasing the residual stress	[191]

Material	Fabrication Process	Parameter	Effect	Laser Power	Measurement Methods	Results	Reference
Iron-based	L-PBF	Layer thickness	↑	107 W, 200 W	-	Increasing layer thickness resulted in poorer mechanical properties.	[132]
Nickel-chromium alloy	L-PBF	Laser power / Scanning Strategy	↑	400 W		High laser power intensifies heating and cooling rates, influencing residual stress formation.	[36]
Ti–6Al–4V	L-PBF	Laser power	↑	Varying (20 W, 30 W and 50W)	-	An increase in laser power enlarges the molten pool and extends cooling duration, potentially mitigating residual stress.	[192]
Ti–6Al–4V	L-PBF	Laser power	↓	120 W-150 W	-	Increased laser power correlates with heightened residual stress; reduction in power reduces stress levels.	[136]

Material	Fabrication Process	Parameter	Effect	Laser Power	Measurement Methods	Results	Reference
Stainless Steel 316L	L-PBF	Laser power	Vary power	160 W-200 W	X-ray diffraction	Higher laser power increases in-depth residual stress: distribution varies with build height.	[137]
Stainless Steel 316L	L-PBF	Laser power	Vary power	100 W-350 W	-	Maximum residual stress values escalate with an increase in laser power; lower energy per unit length reduces stresses.	[42]
Stainless Steel 316L	L-PBF	Laser power	Optimize laser power	300 W	bridge curvature method	An optimal laser power of 300 W effectively minimizes curling angle and controls RS, highlighting laser power as a pivotal factor in RS management.	[180]
AISI 304 Stainless Steel	DED	Scanning speed	↓	-	-	Lower scanning speeds and temperature gradients reduce	[98]

Material	Fabrication Process	Parameter	Effect	Laser Power	Measurement Methods	Results	Reference
						residual stress in SS304 parts.	
JIS SCM440	L-PBF	Scanning speed	Vary speed	Average power: 50 W Peak power: 3 kW	Beam model	Residual stress decreases with increasing scan speed up to a threshold, beyond which it rises again.	[101]
Stainless Steel 316L	L-PBF	Scanning speed	↑	100 W	-	Melt pool length increases, but width and depth decrease with higher scanning speeds, indicating less cooling time.	[141]
Ti–6Al–4V	L-PBF	Scanning speed	↑	120 W-150 W	-	Increasing scanning speed reduces residual stress in fabricated layers, highlighting the importance of scanning speed in stress management.	[136]

Material	Fabrication Process	Parameter	Effect	Laser Power	Measurement Methods	Results	Reference
Stainless Steel 316L	L-PBF	Laser power, Scanning speed	Vary laser power and scanning speed	160 W-240 W	X-ray diffraction	Higher laser powers and slower scanning speeds increase residual stress; stripe scanning results in more stress than chessboard scanning.	[117]
Inconel 718	L-PBF	Laser power, Scanning speed, Hatch space	↑	Varied	X-ray diffraction	Increased energy density changes phase composition of IN718, potentially leading to unexpected part growth due to deeper melt pools.	[158]
Stainless Steel 316L	L-PBF	Laser power, Scanning speed	Optimize parameters	-	-	Identifies a safe range for laser power and scanning speed that ensures molten pool stability and higher densification levels.	[134]

Material	Fabrication Process	Parameter	Effect	Laser Power	Measurement Methods	Results	Reference
Stainless Steel 316L / Ti-6Al-4V / Inconel 718	LAM	Laser power, Scanning speed	Increase speed, Adjust power	190 W–270 W	-	Elevated laser power increases distortion and residual stress; higher scan speeds can mitigate these effects.	[139]
Ti-6Al-4V	L-PBF	Laser power, Scanning speed	Vary power and speed	100 W-300 W	X-ray diffraction, Hole drilling, Contour method	Lower scanning speed and higher laser power reduce residual stress due to slower cooling.	[135]
Stainless Steel 316L	L-PBF	Laser power, Scanning speed	Adjust power and speed	150 W, 350 W	-	Melt height larger at lower power and higher speed; increasing power and reducing speed enhance melt penetration and width.	[142]
Tungsten	L-PBF	Laser power, scanning speed, hatch spacing	Adjust parameters	200 W - 300 W	-	Surface morphology transitions to dense and flat with increased laser power, indicating densification improvement.	[144]

Material	Fabrication Process	Parameter	Effect	Laser Power	Measurement Methods	Results	Reference
Aluminum 2024 Alloy	L-PBF	Scanning speed, hatch spacing	Optimize scanning speed and hatch spacing	-	-	Optimal surface quality and reduced porosity achieved with slower scanning speeds and wider hatch spaces (80)	[145]
Stainless Steel 316L	L-PBF	Scanning speed, Island dimensions	Optimize scanning strategy	100 W - 400 W	Digital image correlation, Neutron diffraction	Reducing island size and employing shorter scan vectors decrease tensile residual stresses; 45-degree off-axis scanning aligns thermal stresses more favorably, reducing residual stresses.	[149]
Ti–6Al–4V	L-PBF	Laser jump speed	Varying jump speed and scan lengths	300 W	-	Laser jump speed significantly impacts stress distribution, with optimal speeds reducing stress perpendicular to the scanning direction. Increasing jump speed	[184]

Material	Fabrication Process	Parameter	Effect	Laser Power	Measurement Methods	Results	Reference
						beyond 1000 mm/s induces contrary effects.	
Stainless Steel 316L	L-PBF	Scan vector length	↓	200 W	X-ray diffraction	Reducing scan vector length from 42 mm to 18 mm decreases residual stress by over 50% at certain points.	[66]
Ti-6Al–4 V	L-PBF	Scan vector length	↓	40 W 82.5 W	-	A 28% reduction in Von Mises stress observed with scan vector length shortened from 3 mm to 1 mm.	[57]
-	L-PBF	Scan vector length	↓	1000 W	-	Demonstrated that shorter scan vectors significantly reduce distortion.	[190]
Stainless Steel 316L, Inconel 718	L-PBF	Scan vector orientation, Island size	Use 45° inclined scanning, Optimize island size	100-400	Digital image correlation, Neutron diffraction	Employing a 45° inclined line scanning technique and optimal island sizes reduces	[149]

Material	Fabrication Process	Parameter	Effect	Laser Power	Measurement Methods	Results	Reference
						deformation and residual stress.	
Stainless Steel 316L	L-PBF	Combination of parameters (Energy density)	Use specific energy density	-	-	Specific energy density achieves over 98% porosity, highlighting its significance in process optimization.	[160]
Stainless Steel 316L	L-PBF	Combination of parameters (Energy density)	↑	-	-	Higher minimum energy density required for >99.5% part density, influencing microstructure and mechanical properties.	[161]
Ti-6Al-4V	L-PBF	Combination of parameters (Energy density)	Adjust energy density	-	Synchrotron X-ray diffraction	Lower energy densities result in higher residual stress, with 53.0 $\frac{J}{mm^3}$,showing the highest stress, illustrating energy density's impact on residual stress.	[162]

Material	Fabrication Process	Parameter	Effect	Laser Power	Measurement Methods	Results	Reference
Ti-6Al-4V	Laser Beam Melting	Combination of parameters (Energy density)	Evaluate energy density reliability	-	X-ray diffraction	Parts with the same energy density but different scanning speeds and laser powers showed varying residual stresses, questioning energy density's reliability for comparisons.	[124]
SAE304 stainless steel (as substrate)	L-PBF	Substrate thickness	↑	180 W	3D scanning of specimens, dimensional deviations were measured using GOM Inspect software by comparing scanned data with original CAD geometry	Higher substrate thickness reduces dimensional deviation and residual stress formation	[182]

Material	Fabrication Process	Parameter	Effect	Laser Power	Measurement Methods	Results	Reference
Ti-6Al-4V	DED	Substrate design	Different substrate geometry: solid, hallow, rectangular	1500 W	Displacement sensor, Thermocouples, data logger	Hallow design resulted in 62 % reduction in residual stress.	[181]
Ti-6Al-4V	L-PBF	Dual – laser beam	Auxiliary laser: 30 W, 60 W, 90 W	120 W	Computational	Post-heating mode with 90 W auxiliary laser power and Δx = -0.1 mm achieved the lowest RS**.** Higher auxiliary laser power generally leads to lower RS due to more uniform temperature distribution and reduced cooling rates.	[187]
Stainless steel 316L	L-PBF	Dual – laser beam	Auxiliary laser: 100 W, 200 W at different offsets	200 W	-	Reducing cooling rate, mitigation of residual stress up to 30%, better surface finish, near full dense component.	[188]

Material	Fabrication Process	Parameter	Effect	Laser Power	Measurement Methods	Results	Reference
TI-6Al-4V	L-PBF	Dual – laser beam	Auxiliary laser: 100 W, 200 W, 300 W, 400 W, 500 W	300 W	X-ray diffraction	Vertical post-heating strategy reduced equivalent stress by 22.55%	[189]

2.3. Recent advancements

Finite element analysis (FEA) and experimental methods and trial-and-error approaches have been common methods to optimize process parameters to reach the minimum residual stress, distortion, and porosity in parts fabricated by laser-based metal additive manufacturing. Furthermore, the results obtained from them are beneficial to analyze and study the relationship and sensitivity between process parameters and mechanical properties of final components. However, both approaches confront challenges such as long computation time, high energy consumption and expenses. In recent years, machine learning (ML) algorithms have been recognized as practical, accurate and powerful techniques to establish relations between the process parameters such as laser power, scanning speed, and hatch space, laser beam diameter, and outputs like melt pool geometry, residual stress, or any mechanical properties. Liu et al.[193] reviewed ML algorithms used to optimize process parameters such as laser power, scanning speed, and hatch space to predict melt-pool geometry, fatigue life, and porosity of the final component. For instance, in one study, Gaussian Process Regression (GPR) predicts melt pool depth with less than 3% error based on laser power, scanning speed, beam size, and absorptivity[194]. Tapia et al.[195] modeled a GP-based framework to forecast melt pool depth in L-PBF of 316 stainless steel using laser power, scanning speed, and laser beam diameter as input achieving mean absolute errors ranging from 6 to 11 µm.

Thakur et al.[196] attempted to optimize the laser power, scanning speed, and hatch spacing to reduce the residual stress and distortion in AlSi10Mg alloy fabricated by L-PBF. They used nonlinear regression analysis and a residual stress value of 385.58 MPa was obtained using a laser power of 80 W, scanning speed of 950 mm/s and hatch spacing of 70 µm. Their model was trained with 80% of data and predicted stresses with an accuracy of 94.85%.

A recent review by Wu et al.[197] claimed the accuracy and enhanced temporal efficiency of ANN, CNN, and nonlinear regression analysis to predict residual stress and optimize process parameters for the reduction of residual stress compared to FEA. Also, deep learning methods offer time and cost-saving solutions in the analysis of melt pool dimensions and prediction of residual stress distribution. For instance, Woo and Ki[198] developed Conditional Generative Adversarial Network (cGAN) and fed laser power, beam diameter, and exposure time into model and predicted residual stress distributions and molten pool dimension in carbon steel. They trained the model on data from over 800 numerical simulations and achieved R^2 values between 0.975 to 0.999 while each single prediction took 0.13 s.

In conclusion, Machine learning algorithms such as ANN, CNN, and GPR accurately predict melt pool geometry, residual stress, and distortion in additive manufacturing. Therefore, these advancements make them candidates to replace traditional approaches like FEA to optimize process parameters, reduce defects, and enhance mechanical properties in the final parts. However, providing a high-quality data set, practical data elaboration, and the development of novel techniques to increase accuracy and reduce prediction error require continued research efforts.

3. Material and methods

3.1. Material

Several metals have been used in the metal additive manufacturing process to fabricate the product. Among all, Ti-6Al-4V has been chosen to be used in this study due to its special features. The characteristics such as its high strength-to-wight ratio, excellent corrosion resistance, and biocompatibility provide its widespread use in aerospace, biomedical, and automotive applications. During the thermal analysis, Ti-6Al-4V is considered as two states: 1) Powder, 2) Soild. The thermal and mechanical properties of Ti-6Al-4V are different in these two states. Therefore, the relevant thermal properties of Ti-6Al-4V, including temperature dependent thermal conductivity, specific heat, density, Poisson ratio and thermal expansion coefficient for both powder and solid were adopted from literature and presented in Table 8, 9, 10, 11. These properties were implemented in the simulation model to accurately capture the transient thermal behavior and the development of residual stresses during the build process.

Table 8 Solidus and liquidus temperatures of Ti-6Al-4V used for defining the phase change range in the thermal simulation[199]

Property	Unit	Values
Solidus temperature, T_s	K	1878
Liquidus temperature, T_L	K	1928
Latent Heat	$\frac{J}{kg}$	280000

Table 9 Temperature-dependent thermal and physical properties of Ti-6Al-4V used in the thermal simulation, including thermal conductivity, specific heat, and density of the solid phase. These values were implemented to model transient heat transfer behavior during the L-PBF process[199]

Temperature (K)	Thermal conductivity ($\frac{W}{m\cdot K}$)	Specific heat* ($\frac{J}{kg\cdot K}$)	Density ($\frac{kg}{m^3}$)
293.15	7	546	4420
373.15	7.45	562	4406
773.15	12.6	651	4350
1273.15	19.3	641	4282

1873.15	27	750	4198
1923.15	28.4	759	4189
1933.15	33.4	831	3920
2173.15	34.6	831	3750
3073.15	34.6	831	3138

*Can be used for both powder and solid

Table 10 Temperature-dependent thermal conductivity and density values of Ti-6Al-4V powder used in the thermal simulation[199]

Temperature (K)	Thermal conductivity $(\frac{W}{m\cdot K})$	Density $(\frac{W}{m\cdot K})$
293.15	0.2	0.2
1878.15	19.4	19.4
1923.15	28.3	28.3

Table 11 Poisson ratio values of Ti-6Al-4V powder used in the thermal simulation[200]

Temperature (K)	Poisson's Ratio
300	0.31
600	0.33
900	0.35
1200	0.39
1500	0.41
1800	0.43
2100	0.45
2400	0.45
2700	0.45
3000	0.45
3300	0.45
3600	0.45

3.2. Additive manufacturing process

To evaluate the effect of scanning strategies on the mitigation of residual stress in parts fabricated via L-PBF, 23 Ti-6Al-4V samples with dimensions of 20 mm × 20 mm × 15 mm were fabricated using the PrintSharp 250, a PBF machine designed for medium-volume applications (Fig. 24c) [201]. A detailed overview of the machine's technical features is provided in Table 12.

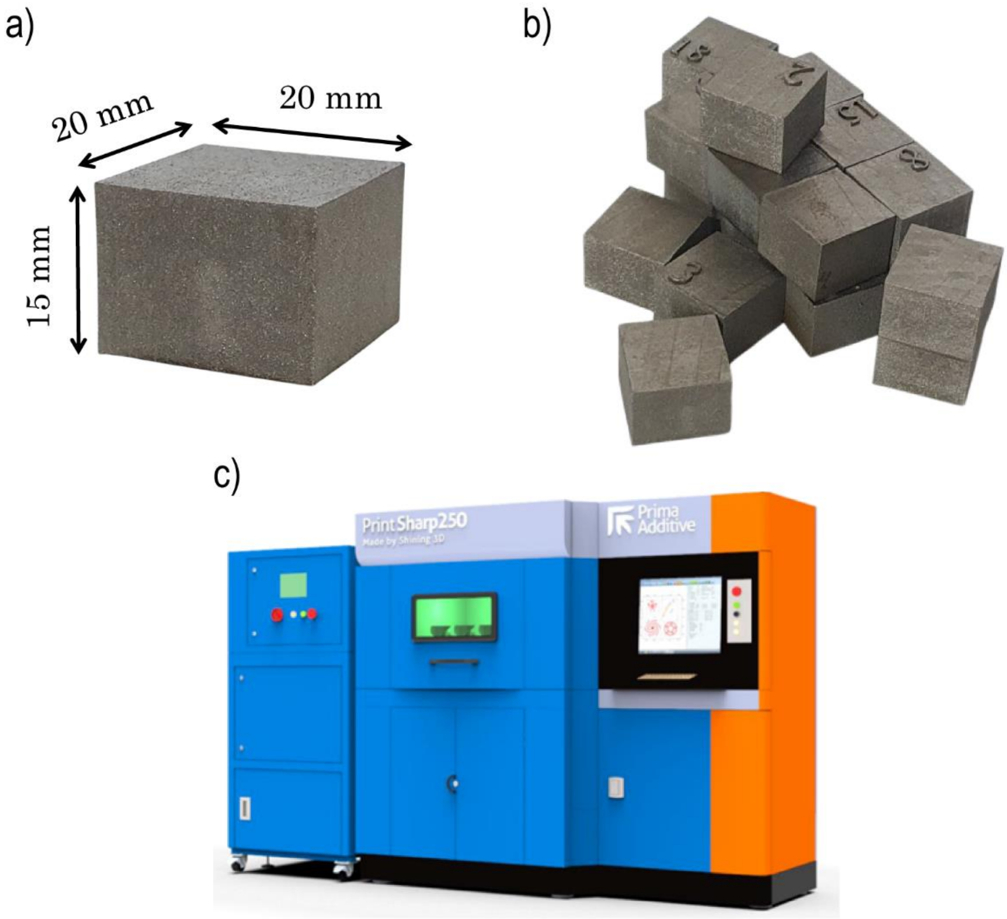

Fig. 24 a) geometry of the printed samples. b) schematic of printed samples. c) schematic of PrintSharp 250, a PBF machine

Table 12 Technical Specifications of the PrintSharp 250, a PBF machine

Category	Specification
Dimensions (L×W×H)	3500 (L) – 1100 (W) – 2450 (H) mm
Weight	2000 kg
Power Supply	380 V / 50 Hz / 8 kW
Type of Laser	Yb (Ytterbium) Fiber Glass
Laser Power	200 W / 500 W (Optional)
Laser Focus Diameter	70 – 100 µm
Beam Wavelength	1060 – 1080 nm
Building Volume	250 × 250 × 300 mm
Beam Deflection Speed	8 m/s
Positioning Speed	10 m/s
Build Rate	12 – 30 cm^3/h

Layer Thickness	0.02 – 0.1 mm
Layer Width	0.1 mm (single line width)
Recoater Specs	Travel: 650 mm
Building Platform z-axis	Travel: 300 mm / Speed max: 6 mm/s / Res: 0.01 mm
Heating Platform	Up to 200°C
Monitoring of O_2 Level	Below 100 ppm
Permissible Room Temperature	15 – 30°C
Gas (Consumption – running/filling)	7 l/min (running), 20 l/min (up to filling)
System Fill Consumption	20 l/min (up to filling)
CAM Software	Materialise Magics
Control & Other Software	Eplus control software (EPC)
Industrial Interfaces	Ethernet

To achieve our objective, the samples were printed with same process parameters such as laser power of 200 W, a scanning speed of 1000 mm/s , a layer thickness of 0.03 mm, and a hatch spacing of 0.08 mm, but with different scanning strategies. 45° rotation, 67° rotation, and unidirectional scanning strategies both in the continuous and discontinuous modes were implemented. However, they varied in the hatch angle rotation schemes, which are crucial for analyzing the effects of scan rotation on thermal gradients and residual stress distribution. The hatch orders for each of the scanning strategies are:

- Continuous 45° rotation: starting from 0° up to 360° in 45° steps (0°, 45°, 90°, 135°, 180°, 225°, 270°, 315°, 360°).
- Continuous 67° rotation: rotation pattern with hatch angles of 12°, 79°, 146°, 213°, 280°, and 347°.
- Continuous unidirectional rotation strategy, with hatch angles of 0°, 90°, 180°, 270°, and 360°.

The remaining discontinuous strategies followed the same three hatch angle rotation strategies—45°, 67°, and 90° patterns—as described above but implemented them in a discontinuous manner. To summarize, the fabrication parameters have been reported in Table 13 and the schematic of scanning strategies are depicted in Fig. 25 and 26.

Table 13 Sample dimensions and fabrication parameters

Parameter	Value
Sample dimensions	20 mm × 20 mm × 15 mm
Laser power	200 W
Scanning speed	$1000\,\frac{\mathrm{mm}}{\mathrm{s}}$
Layer thickness	30 µm
Hatch spacing	80 µm
Spot size	80 µm
Pre-heating	100 ℃

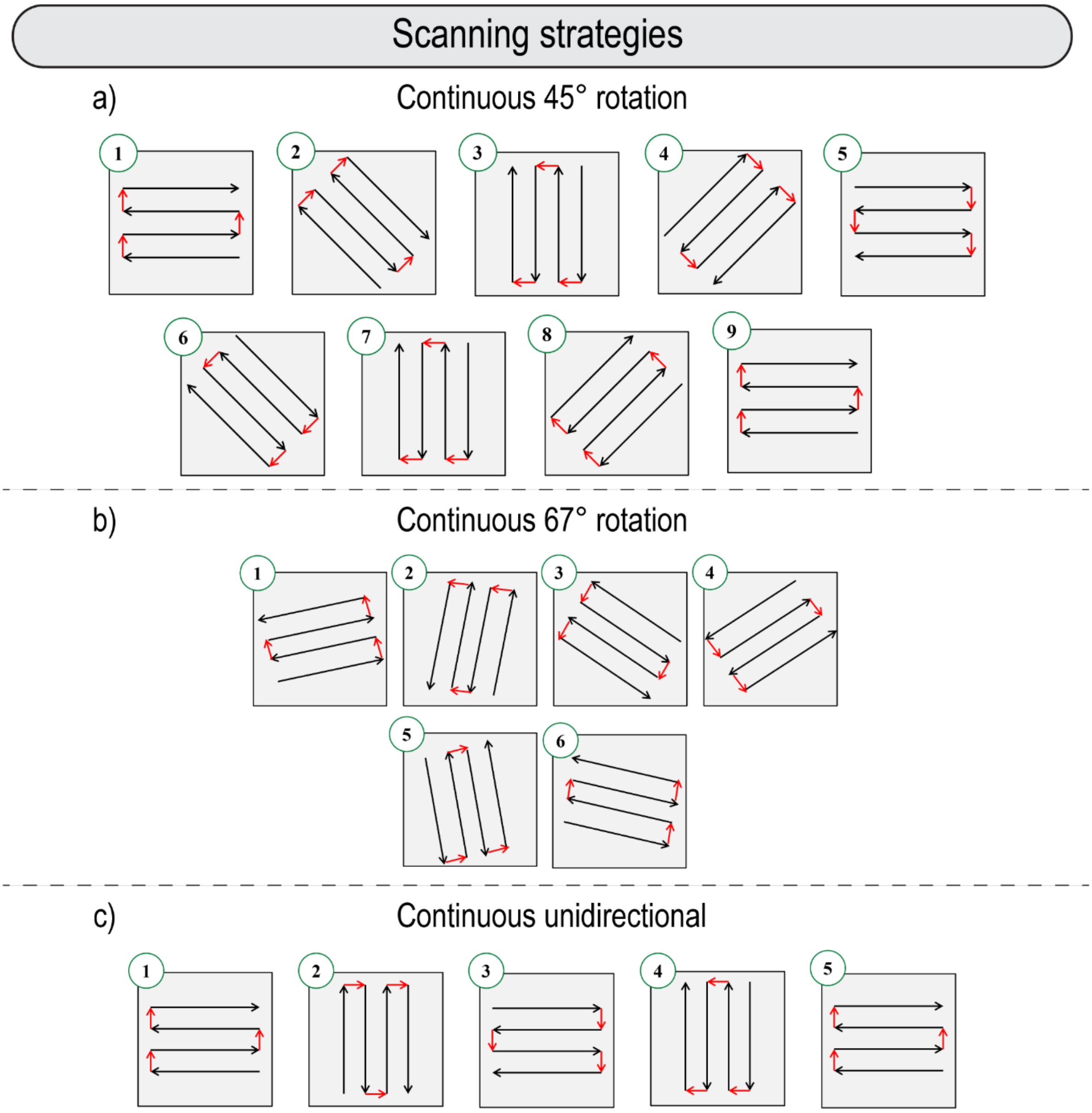

Fig. 25 Illustration of scanning strategies used in fabrication of process: a) continuous 45° rotation, b) continuous 67° rotation, c) continuous unidirectional

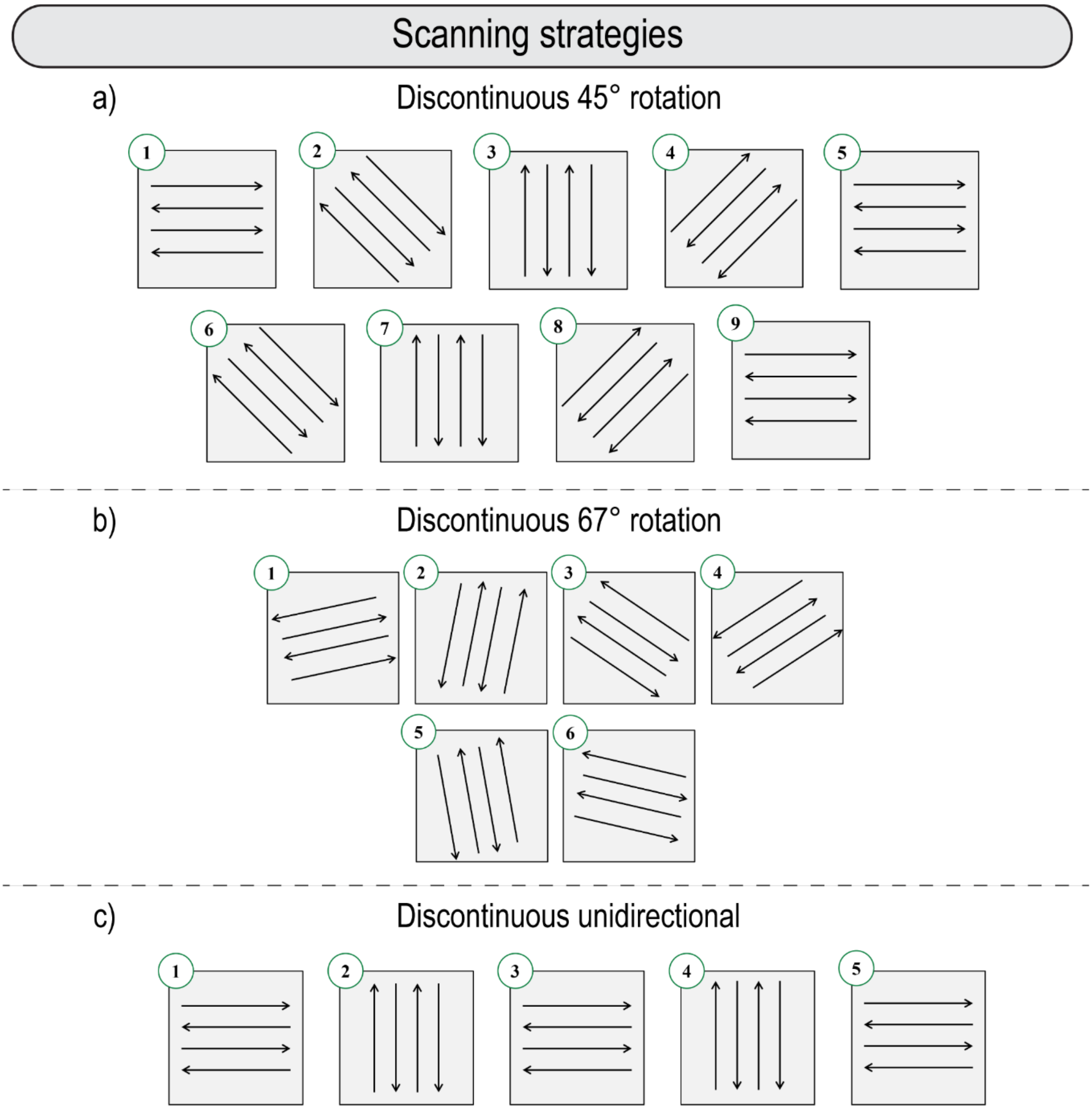

Fig 26 Illustration of scanning strategies used in fabrication of process: a) discontinuous 45° rotation, b) discontinuous 67° rotation, c) discontinuous unidirectional

3.3. Computed Tomography

X-ray computed tomography (XCT) was employed to characterize porosity in selected samples fabricated with different scanning strategies. Six samples, each representing a unique scanning strategy—including continuous and discontinuous modes with varying rotation angles—were chosen for analysis to obtain a more accurate, three-dimensional assessment of internal porosity. The XCT analysis provided detailed information on pore volume fraction, spatial distribution, and pore morphology within each sample, enabling a deeper understanding of how scan strategy influences defect formation in L-PBF components. The schematic of the equipment used for the measurement is shown in Fig. 27.

This analysis was necessary to investigate the stability of the molten pool and to verify the printability of the samples, which is essential before proceeding to the next step—analyzing residual stress in the fabricated components.

Fig 27 The X-ray computed tomography (XCT) system used for porosity analysis[201]

3.4. Numerical Simulation

To investigate the effect of residual stress in L-PBF, a computational model was developed in Abaqus for finite element analysis (FEA). In this simulation, two layers of powder were modeled over the baseplate. To reduce computational cost, the first layer was modeled as a subsection of the baseplate (Fig. 28a), meaning a separate section was applied to the top surface of the baseplate with a thickness equivalent to the powder layer, and powder properties were assigned to it. The dimensions and material properties of the powder layer and baseplate are summarized in Table 14.

To accurately capture the thermal interaction between the powder layer, the baseplate, and the melt pool geometry, the scanning region (powder layer) was discretized using a fine mesh. Specifically, the region was divided into 100 elements along both the x and y directions, and into 5 elements in the depth (z) direction, resulting in an element size of 20 µm × 20 µm × 6 µm. The baseplate was meshed with a coarser element size compared to the powder layer to reduce computational cost. However, to ensure proper thermal continuity, the mesh lines along the x and y directions were aligned with those of the scanning region, maintaining the same number of elements along each axis. The powder layer was meshed using hexahedral (brick) elements, generated using the sweep meshing technique to ensure structured 8-node linear thermal brick elements (DC3D8 in Abaqus). The geometry and mesh configuration used in the thermal simulation is depicted in Fig. 28.

Table 14 Geometrical dimensions and material assignment of the baseplate and powder layer used in the simulation model.

	Baseplate	Layer powder
Dimension (x,y,z)	3 mm × 3 mm × 0.5 mm	2 mm × 3 mm × 0.03 mm
Material	Ti-6Al-4V	Ti-6Al-4V

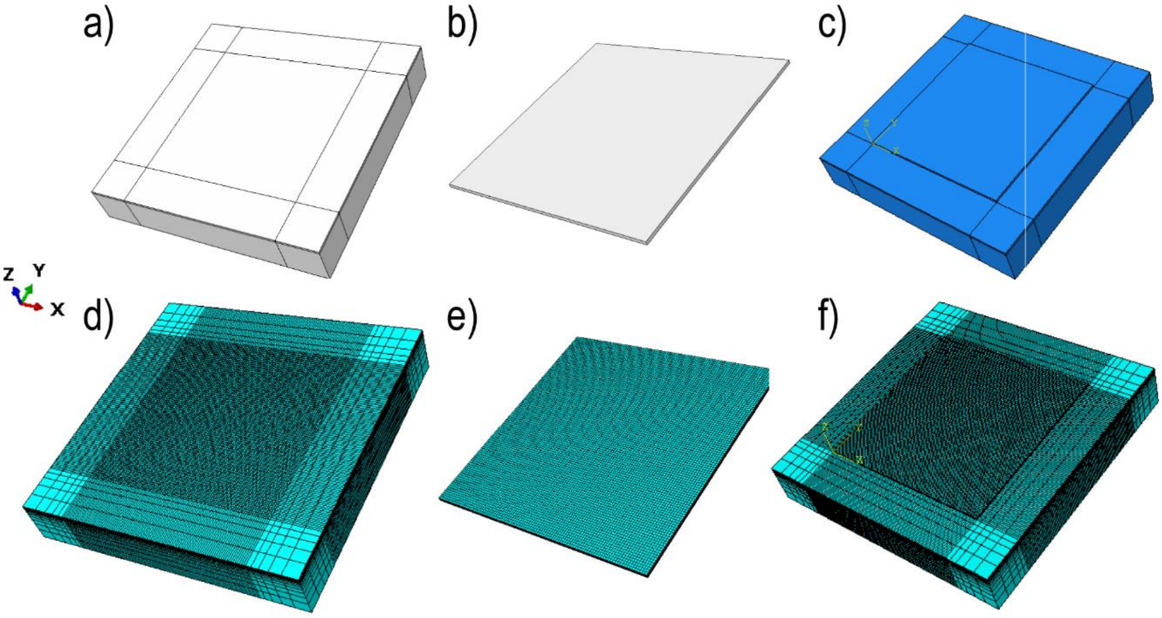

Fig 28 Geometry and mesh configuration used in the thermal simulation: (a) baseplate and first powder layer inside it, (b) second powder layer (scanning region), (c) assembly of powder layer on baseplate, (d) meshed baseplate with fine elements in the scanning region, (e) mesh of the second powder layer, and (f) complete meshed model showing mesh

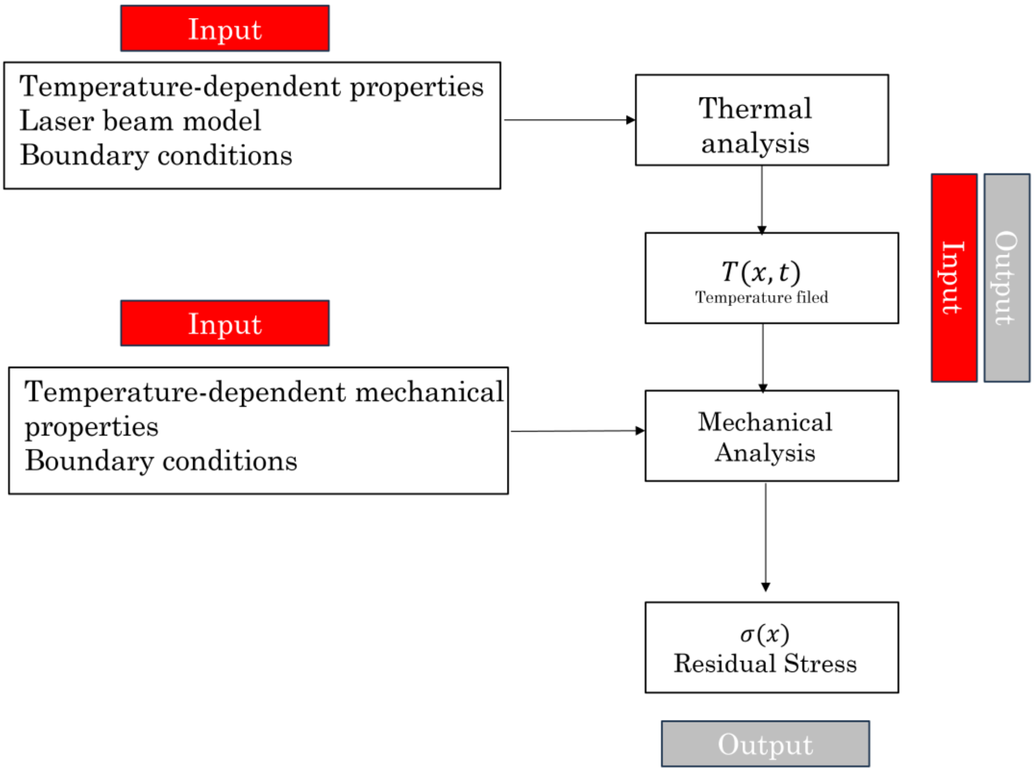

Fig 29 Workflow of the thermo-mechanical simulation framework in Abaqus.

Fig. 29 represents the workflow of the simulation section. As it is illustrated, the simulation has two stages:

1) Thermal analysis

2) Mechanical analysis

In the first stage, the goal is to capture the transient temperature distribution during the laser scanning and deposition of the layers. The inputs for this stage are temperature-dependent thermal properties such as thermal conductivity and specific heat, laser beam, and thermal boundary conditions for instance convection or radiation. Hence, by finishing the first stage, temperature field (T(x,t)) is provided.

In the second stage, the temperature field will be input for the mechanical simulation. The other inputs are temperature dependent mechanical properties such as Young`s modulus and mechanical boundary conditions and constraints. The final output of this stage is the residual stress field (σ) within the part. This approach is called coupled thermomechanical simulation, which allows for more accurate prediction of residual stresses generated during the L-PBF process.

3.4.1. Thermal Analysis

As it is shown in the Figure 26, The first step of the simulation is to obtain the temperature distribution by running thermal analysis. To do so, DFLUX subroutine was implemented to control and move the heat source over baseplate and layer powder. In the DFLUX subroutine, a 3D gaussian moving heat source was assumed to apply heat flux to the region. This heat source model captures the localized and rapidly varying heat input typical of laser-based additive manufacturing and is effective for predicting the resulting melt pool characteristics and thermal gradients.

The subroutine allows for spatial and temporal control over the heat input, enabling the laser to move along a predefined path that replicates the scanning strategies used in the experimental builds. The energy distribution of the laser beam was modeled based on the Eq. (8):

$$q(x, y, z, t) = \frac{\sqrt[5]{2}\,\eta P}{\pi^{1.5}.a.b.c} \exp\left(-2.\left(\frac{(x - x_c)^2}{a^2} + \frac{(y - y_c)^2}{b^2} + \frac{(z - z_c)^2}{c^2}\right)\right. \tag{8}$$

In this equation, η. represents the absorptivity, P is the laser power, and a, b, and c denote the semi-axes of the Gaussian heat source distribution along the x, y, and z directions, respectively. The parameters x_c, $y_c$and z_c indicate the coordinates of the moving laser center. The numerical coefficient (e.g. $\sqrt[5]{2}$) directly influences the peak intensity of the heat source. Increasing this coefficient results in a higher peak intensity, while decreasing it leads to a broader distribution with a lower peak. Additionally, the exponent coefficient controls the spatial spread of the heat input. Due to its negative sign in the exponential term, both the pre-factor and exponent can be tuned, provided that the total energy input into the powder bed remains equal to ηP.

By maintaining this energy balance, the exponent and pre-factor can be adjusted without altering the total heat introduced to the material. A higher exponent value narrows the Gaussian distribution, thereby increasing the peak temperature and steepening the thermal gradient. These parameters are critical and can be optimized during the simulation process to match the thermal behavior observed experimentally, ensuring more accurate prediction of thermal history and residual stresses.

Once the laser parameters and heat source are modeled, the next step is to solve the governing heat transfer equation to compute the transient temperature field. The thermal model is based on 3D transient heat conduction equation which is depicted as in Eq. (9):

$$\rho c \frac{\partial T}{\partial t} = Q + \frac{\partial}{\partial x}\left(k \frac{\partial T}{\partial x}\right) + \frac{\partial}{\partial}\left(k \frac{\partial T}{\partial y}\right) + \frac{\partial}{\partial z}(k \frac{\partial T}{\partial z}) \tag{9}$$

Where:

- ρ is the material density ($\frac{\mathrm{kg}}{\mathrm{m}^3}$)
- c is the specific heat capacity ($\frac{J}{kgK}$)
- T is the temperature (K)
- t is the time (s)
- Q is volumetric heat input ($\frac{W}{mK}$), and

- k is the thermal conductivity ($\frac{W}{mK}$)

Also, it is needed to simulate heat loss to the ambient environment. In this study natural convection to the ambient environment was applied to the top surface of the powder bed, which can be expressed by Eq. (10) :

$$-\mathrm{k}\frac{\partial \mathrm{T}}{\partial \mathrm{z}} = \mathrm{h_{conv}}(\mathrm{T} - \mathrm{T_\infty}) \tag{10}$$

Where:

- $\mathrm{T_\infty}$ is the ambient temperature (taken 300.15 K)
- $\mathrm{h_{conv}}$ is the convective heat transfer coefficient, assumed to be 20 ($\frac{\mathrm{W}}{\mathrm{m^2K}}$) [202].

To accurately capture the thermal history of the layers and make the simulation representative of the actual L-PBF process, the USDFLD subroutine was implemented in Abaqus. This user-defined subroutine enables the assignment of different material states based on field variables, allowing for the simulation of state transitions during the build. In this study, two states—powder and solid—were defined for the powder layer. When heat flux is applied and the temperature of the powder increases, it initially behaves based on the temperature-dependent properties of the Ti-6Al-4V powder. Once the temperature exceeds the melting point of Ti-6Al-4V, the material state is updated, and the element transitions to the solid (or molten) state, behaving according to the temperature-dependent properties of Ti-6Al-4V solid. This technique ensures a more realistic simulation of material behavior during the L-PBF process.

To implement the thermal analysis, a constant laser power of 200 W and a scanning speed of 1 mm/s were applied throughout the simulation. The scanning area comprised six parallel tracks, each 1.5 mm in length, with a hatch spacing of 0.2 mm. As mentioned above, model consists of two layers, each layer has layer thickness of 0.03 mm. The laser absorptivity was set to 0.3, consistent with reported values for Ti-6Al-4V powder. A Gaussian heat source was employed with semi-axes of 56 μm in the x and y directions (a and b), and 100 μm in the z direction (c), to represent the spatial energy distribution within the melt pool.

The baseplate was preheated at a temperature of 373.15 K (100 °C). To investigate the effect of scanning strategy on thermal distribution and residual stress, six different scanning strategies in two layers were modeled:

- 45° rotation (Fig. 30a,b)
  - Continuous
  - Discontinuous
- 67° rotation (Fig. 30c,d)
  - Continuous
  - Discontinuous
- Unidirectional rotation (Fig. 30e,f)
  - Continuous
  - Discontinuous

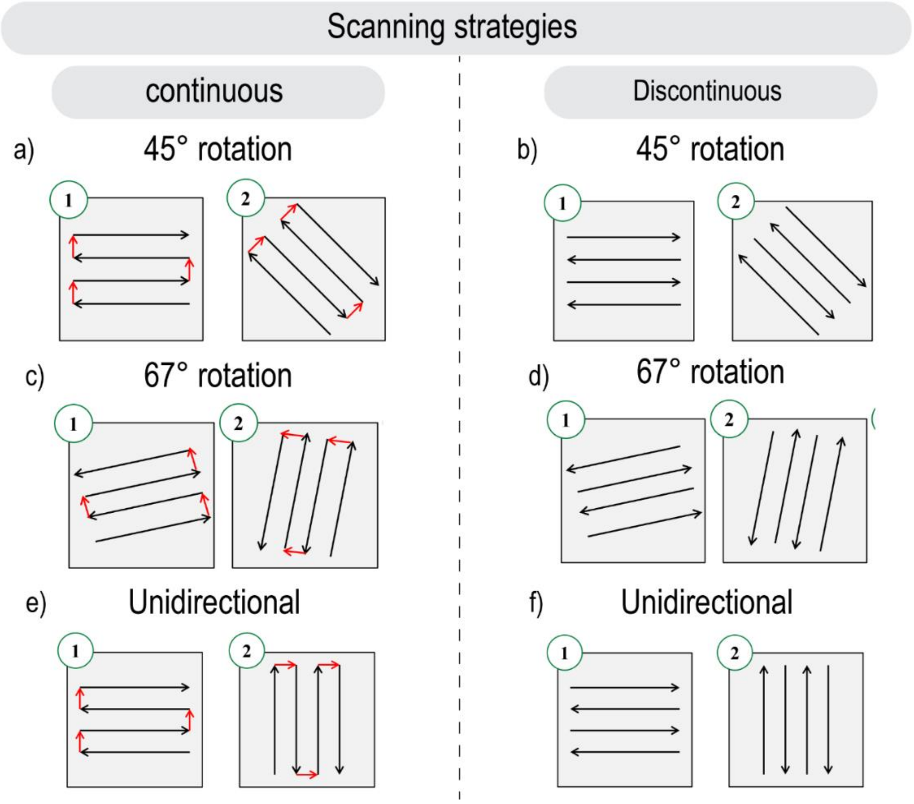

Fig 30 Schematic representation of the scanning strategies used in the simulation. The strategies are categorized into continuous (left column) and discontinuous (right column) modes, each applied over two layers: (a, b) 45° rotation, (c, d) 67° rotation, and (e, f) unidirectional. Red arrows indicate laser movement direction with continuous motion between scan lines, while black arrows represent individual scan vectors. Layer 1 and Layer 2 are labeled accordingly

The thermal analysis was structured into four sequential steps: (1) scanning of the first layer, (2) deposition of the second layer, (3) scanning of the second layer, and (4) a final cooling period. For the second-layer deposition, an interlayer time of 0.001 s was introduced to simulate the brief pause between successive layers. In the final step, a cooling duration of 0.1 s was applied to account for thermal relaxation after laser exposure. Overall, this modeling framework enabled the analysis of transient thermal field variations under different scanning strategies, providing insights into in-process residual stress mitigation. The full list of simulation parameters used is summarized in Table 15.

Table 15. Simulation process parameters

Parameter	Value
Laser power	200 W
Scanning speed	1 mm/s
Hatch space	0.2 mm
Number of tracks	6
Number of layers	2
Track length	2 mm
Absorptivity	0.30
Initial temperature	373.15 K
Interlayer time	0.001s
Cooling time	0.1 s

3.4.2. Mechanical Analysis

After obtaining the temperature field from the thermal analysis, the next stage involved mechanical simulation. The temperature history was imported into a *static general* step in Abaqus as a time-dependent thermal load. A temperature-dependent elastic–plastic material model was assigned to Ti-6Al-4V to accurately capture its mechanical response under thermal loading. The temperature-dependent properties, namely, Young’s modulus, yield strength, and coefficient of thermal expansion—were defined based on values reported in the literature, as summarized in Table 16.

Table 16 Temperature-dependent mechanical properties of Ti-6Al-4V used in the mechanical simulation, including Young's modulus, yield strength, and coefficient of thermal expansion.

Temperature (K)	Young modulus (MPa)	Yield stress (MPa)	Expansion coefficient ($1/c \times 10^{-6}$)
293.15	114000	1061	8.2
373.15	109000	933.7	9.2
473.15	100000	742.7	9.9
588.15	93000	668.4	1.05
703.15	84000	615.4	1.1
813.15	57000	477.5	1.14
1923.15	0.1000	1	2.01
3073.15	0.1000	1	2.01

The governing mechanical behavior was described by the equilibrium equation under quasi-static conditions:

$$\nabla . \sigma + f = 0 \tag{11}$$

Where:

- σ is the Cauchy stress tensor, and
- f is the body force vector, (negligible in small-scale additive manufacturing models)

The mechanical model incorporated thermo-elasto-plastic behavior based on the von Mises yield criterion with isotropic hardening, appropriate for high-temperature processing of metals. The strain increment at each integration point was decomposed as:

$$d\varepsilon^{\mathrm{Total}} = d\varepsilon^{\mathrm{el}} + d\varepsilon^{\mathrm{pl}} + d\varepsilon^{\mathrm{th}} \tag{12}$$

The thermal strain was calculated by:

$$d\varepsilon^{th} = \alpha(T).\Delta T.I \tag{13}$$

Where:

- $\alpha(T)$ is the temperature-dependent coefficient of thermal expansion
- ΔT is the temperature increment and
- I is the identity tensor.

The stress-strain relationship followed Hooke’s law for temperature-dependent isotropic elasticity:

$$\sigma = C(\varepsilon^{Total} - \varepsilon^{pl} - \varepsilon^{th}) \tag{14}$$

Mechanical boundary conditions were applied by fully constraining the bottom surface of the baseplate in all degrees of freedom, simulating rigid clamping during printing. There is no constraint defined in top and side surfaces, therefore there are free to deform and distort in response to thermal loading.

The static steps in the mechanical simulation followed the same sequence as those defined in the thermal analysis, resulting in four consecutive steps:

1. Layer 1 scanning
2. Deposition of layer 2
3. Layer 2 scanning
4. Cooling time

The temperature fields obtained from each step of the thermal analysis were applied as time-dependent inputs to the corresponding mechanical steps. This ensured consistent temporal mapping between thermal and mechanical simulations. After the final cooling step, the residual stress field was extracted. The primary mechanical outputs included the Von Mises stress, principal stresses, and directional stress components ($\sigma_{xx}, \sigma_{yy},$), which were analyzed to evaluate the influence of different scanning strategies on residual stress mitigation.

4. Result and discaussion

This section presents the result gathered from both experimental measurement and numerical simulation, focusing on the influence of scanning strategies on mitigation of residual stress. 23 samples were printed via L-PBF. To evaluate the print quality, a subset of six samples—each produced with a different scanning strategy—was selected for detailed analysis. These analyses consist of porosity analysis, surface roughness measurement, hardness, and residual stress measurement using XRD method. Then, the simulation reveals information related to temperature distribution and stress fields attributed to each scanning strategies. These simulations provide insights into the mechanisms driving residual stress formation and offer predictive understanding of the effectiveness of each strategy in stress mitigation.

4.1. Computed tomography (CT) analysis

Fig. 31 presents a comprehensive 3D X-ray computed tomography (CT) analysis of six Ti-6Al-4V samples fabricated via laser powder bed fusion (L-PBF). The continuous 45° rotation strategy exhibits a relative density of 97%, the lowest among all strategies. This finding suggests that the continuous 45° rotation may result in insufficient thermal overlap between successive tracks and layers, leading to keyhole formation and inadequate fusion. In contrast, the discontinuous 45° rotation strategy shows an increase in relative density, possibly due to the segmented thermal load, which promotes improved cooling and more uniform temperature distribution. Both continuous 67° rotation and unidirectional strategies (Fig. 31b and 31c) achieved 99% relative density, with likely smaller pores compared to the continuous 45° rotation, attributed to better track overlap and more efficient heat distribution, resulting in enhanced fusion and fewer defects.

The discontinuous 67° rotation results (Fig. 31e) reveal a combination of both high relative density (99%) and porosity elimination, even though a few pores (~1.4 mm and 1.2 mm) exist at the corners. Finally, the discontinuous unidirectional strategy (Fig. 31f) performs the best in terms of high density and pore elimination, as the relative density reaches 99% and no pores larger than 0.7 mm are present.

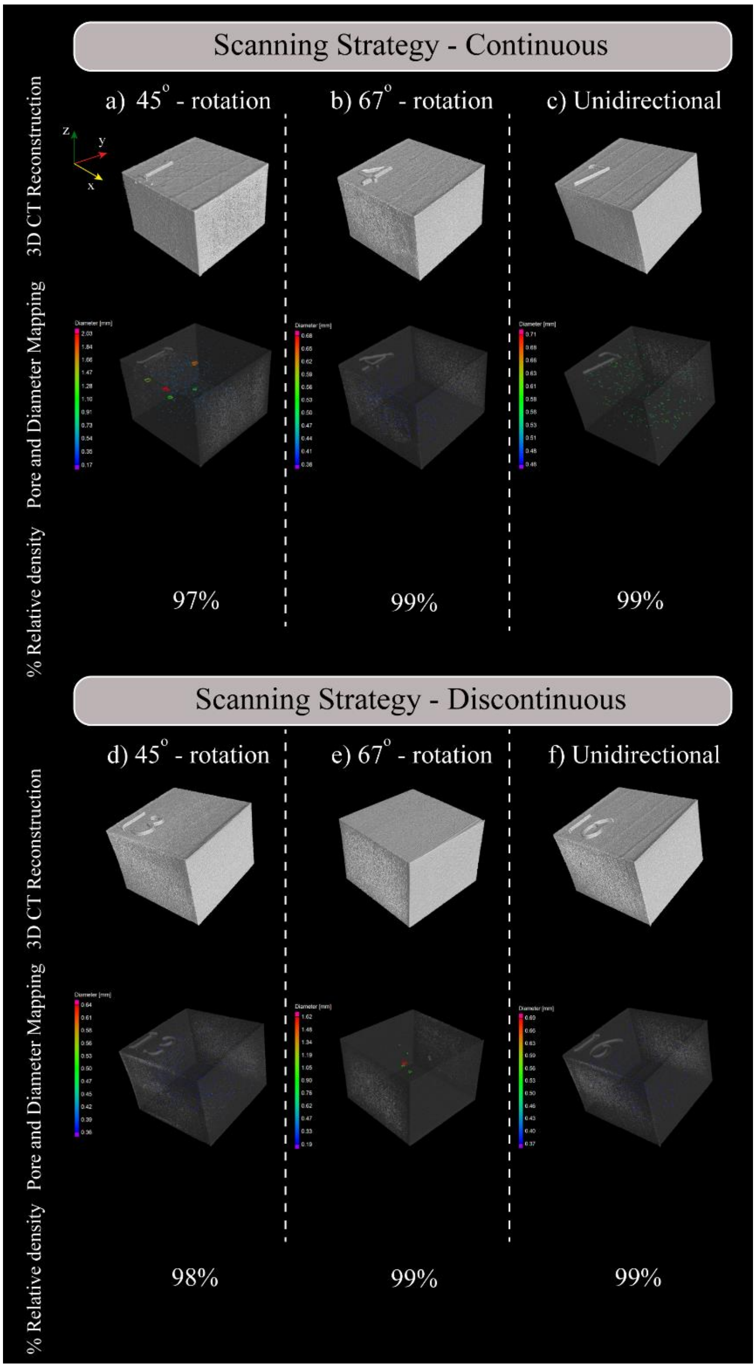

Fig. 31 3D CT reconstructions and pore mapping of samples fabricated with different scanning strategies in L-PBF. a) 45° rotation – continuous, b) 67° rotation – continuous, , c) Unidirectional – continuous d) 45° rotation – discontinuous, e) 67° rotation – discontinuous f) Unidirectional – discontinuous

Overall, implementing discontinuous scanning strategies improves porosity characteristics, as indicated by the CT images, which reveal fewer and smaller pores. This outcome indicates that discontinuous patterns may help reduce heat accumulation by introducing time delays between adjacent scan vectors. As depicted, both the discontinuous 67° rotation and unidirectional strategies yield a relative density of 99%.

Therefore, the quality of the printed samples and stability of molten pool are confirmed to be high, and the microstructural integrity is sufficient to ensure that the results obtained from residual stress measurements and subsequent analyses are reliable and representative of the actual process behavior.

4.2. Surface roughness

Surface roughness (R_a), which represents the arithmetic mean of surface height deviations, was measured using the RTP80 contact profilometer to assess the effect of scanning strategy on the surface quality of the printed samples. For clarity in graphical representation and future reference, Table 17 lists the sample names along with their corresponding scanning strategies.

Table 17 Sample names and their corresponding scanning strategies are used for experimental analysis.

Sample name	Scanning strategy
S1	Continuous 45° rotation
S4	Continuous 67° rotation
S7	Continuous unidirectional
S10	Discontinuous 45° rotation
S13	Discontinuous 67° rotation
S16	Discontinuous unidirectional

As shown in Fig. 32, S10 resulted in Ra of 3.07 µm, yielded the smoothest surface among all the samples. On the other hand, S1 produced the highest roughness among rotated scans with Ra value of 3.80 µm. S4 achieved a good average roughness of 3.52 µm, but noticeable variability. Meanwhile, S13 (discontinuous 67° rotation) showed higher mean Ra (3.63 µm). In the case of unidirectional scanning, S7 resulted in a slightly rougher surface (Ra = 3.59 µm) probably due to uninterrupted scan lines. However discontinuous unidirectional (S16) performed the worst overall, with a mean Ra of 4.97 µm and high scatter.

Overall, the results illustrated that discontinuous scanning strategies improve surface quality for rotated scanning strategies. However, for unidirectional scanning, the island-based approach may introduce geometric discontinuities which lead to poor surface finish.

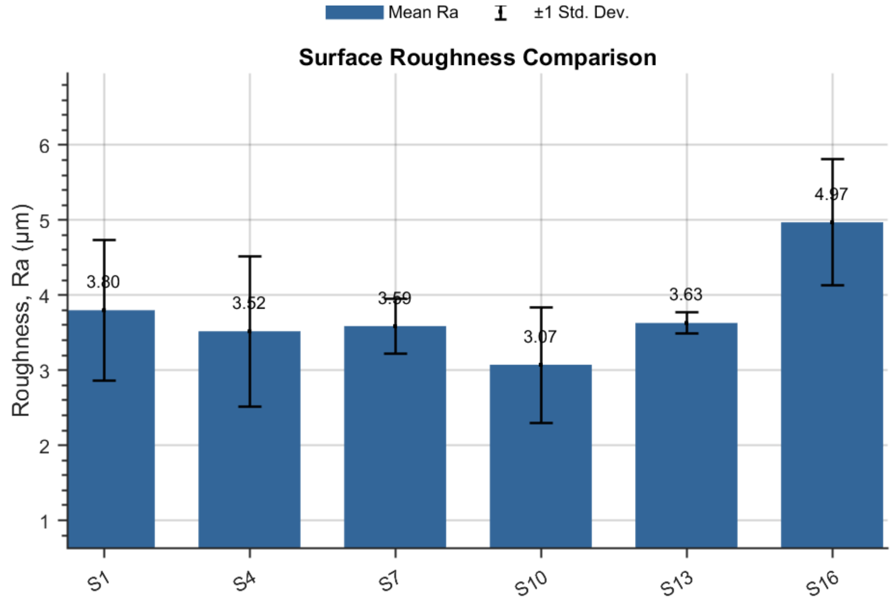

Fig 32 Comparison of mean roughness (Ra) across samples with different scanning strategies

4.3. *Hardness test*

Macrohardness measurement were conducted on as-built Ti-6Al-4V samples. The goal is to investigate the effects of scanning strategies on hardness of the samples and verify the stability of the molten pool, therefore the quality of the pinted samples are verified for the XRD measurements. Five tests were taken on each sample at predefined positions as shown in Fig. 33.

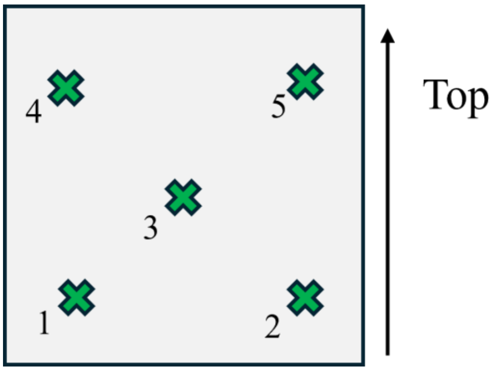

Fig. 33 Indentation locations for macrohardness testing of as-built Ti-6Al-4V samples, used to assess scanning strategy effects

Table 18 presents the hardness values of as-built Ti-6Al-4V samples fabricated using different scanning strategies and rotation angles in an L-PBF process. Both Rockwell hardness (HRC) and the corresponding Brinell hardness (HB) values are reported, along with the standard deviation. Sample S7, built with a continuous unidirectional scanning strategy, achieved the highest hardness (35.7 HRC / 331 HB). S13 exhibited the most consistent hardness (SD = 0.57) among all samples, benefiting from a continuous 45° rotation which likely caused by stable thermal gradients and uniform microstructure formation. These data are consistent with literature, as Khorasani et al. [203] reported value of 270 HB to 410 HB for the as built fabricated parts via L-PBF. In another study, Al-Rubaie et al. [204] reported the value of value of 390 HB as the highest value for the hardness for the as-biult Ti-6Al-4V parts via L-PBF.

Samples using discontinuous strategies (S-O, S16) generally exhibited higher variability, while continuous strategies (S1, S4, S7, S13) yielded more stable hardness profiles, confirming that scan continuity plays a vital role in achieving mechanical consistency. These results confirm that scanning strategy directly affects the mechanical integrity of L-PBF parts, and the selected samples exhibit suitable quality for subsequent XRD characterization, as their macrohardness values fall within the expected range for Ti-6Al-4V parts fabricated by L-PBF.

Table 18 Rockwell hardness (HRC) and Brinell Hardness (HB) values of as-built Ti-6Al-4V samples fabricated using different scanning strategies and rotation angles.

Sample name	Scanning strategy	Rotation	Mean Rockwell (HRC)	Brinell Hardness (HB)	Standard deviation
S1	Continuous	45° rotation	33.9	314	0.94
S4		67° rotation	33.2	308	1.69
S7		Unidirectional	35.7	331	1.03
S13	Discontinuous	45° rotation	34.5	322	0.57
S-O		67° rotation	32.1	300	2.57
S16		Unidirectional	34.8	322	2.18

4.4. XRD measurements of residual stress

Residual stress measurements were performed using the X-ray diffraction (XRD) technique to investigate the effect of scanning strategies on the residual stress in the fabricated parts. The results, summarized in Table 19, reveal that the discontinuous 67° rotation strategy exhibited the lowest residual stress of 220 MPa, performing the best scanning strategy to mitigate the residual stress. In the second level, still 67° rotation shows effective even in the continuous mode with residual stress of 280 MPa.

On the other hand, the continuous unidirectional scanning strategy resulted in the highest residual stress (648 MPa), presenting the limitations of using a fixed scan path without variation across layers. All samples were processed using identical parameters, such as laser power, scanning speed, and layer thickness, meaning that the only varying factor was the scanning strategy.

Continuous unidirectional scanning applies repetitive thermal loading in the same direction, which leads to localized heat accumulation, directional thermal gradients, and limited opportunities for stress redistribution. Without variation between layers, each new layer reinforces the stress patterns formed in previous ones. In contrast, introducing rotation between layers, particularly at larger angles like 67°, can interrupt this accumulation by redistributing the thermal flux and neutralizing stress concentration zones. This effect is especially pronounced in discontinuous strategies, where the laser scan is broken into segments that allow for partial cooling, further reducing the intensity of stress fields and make it more uniform.

The discontinuous 67° rotation strategy, which produced the lowest residual stress of 220 MPa, provides both the directional variation and the natural stress-relief intervals during the fabrication. These findings suggest that strategic rotation between layers not only produce uniform heat distribution but can also counteract or balance thermal effects from previous layers, resulting in a more homogeneous and lower-stress final part.

Table 19. Residual stress values measured by X-ray diffraction (XRD) for samples fabricated using different scanning strategies.

Continuous/Discontinuous	Rotation angle	Residual stress (MPa)	Stress level (lowest to highest)
Continuous	45° rotation	645	5
Continuous	67° rotation	280	2
Continuous	Unidirectional	648	6
Discontinuous	45° rotation	412	3
Discontinuous	67° rotation	220	1
Discontinuous	Unidirectional	494	4

4.5. Thermal analysis

The thermal analysis of one layer containing six laser tracks in laser powder bed fusion of Ti-6Al-4V have been conducted. Six different scanning strategies have been simulated. The corresponding peak temperature and temperature contours related to each scanning strategies are represented in several conditions. For instance, Fig.34 depicts the simulated temperature distribution for six different scanning strategies.

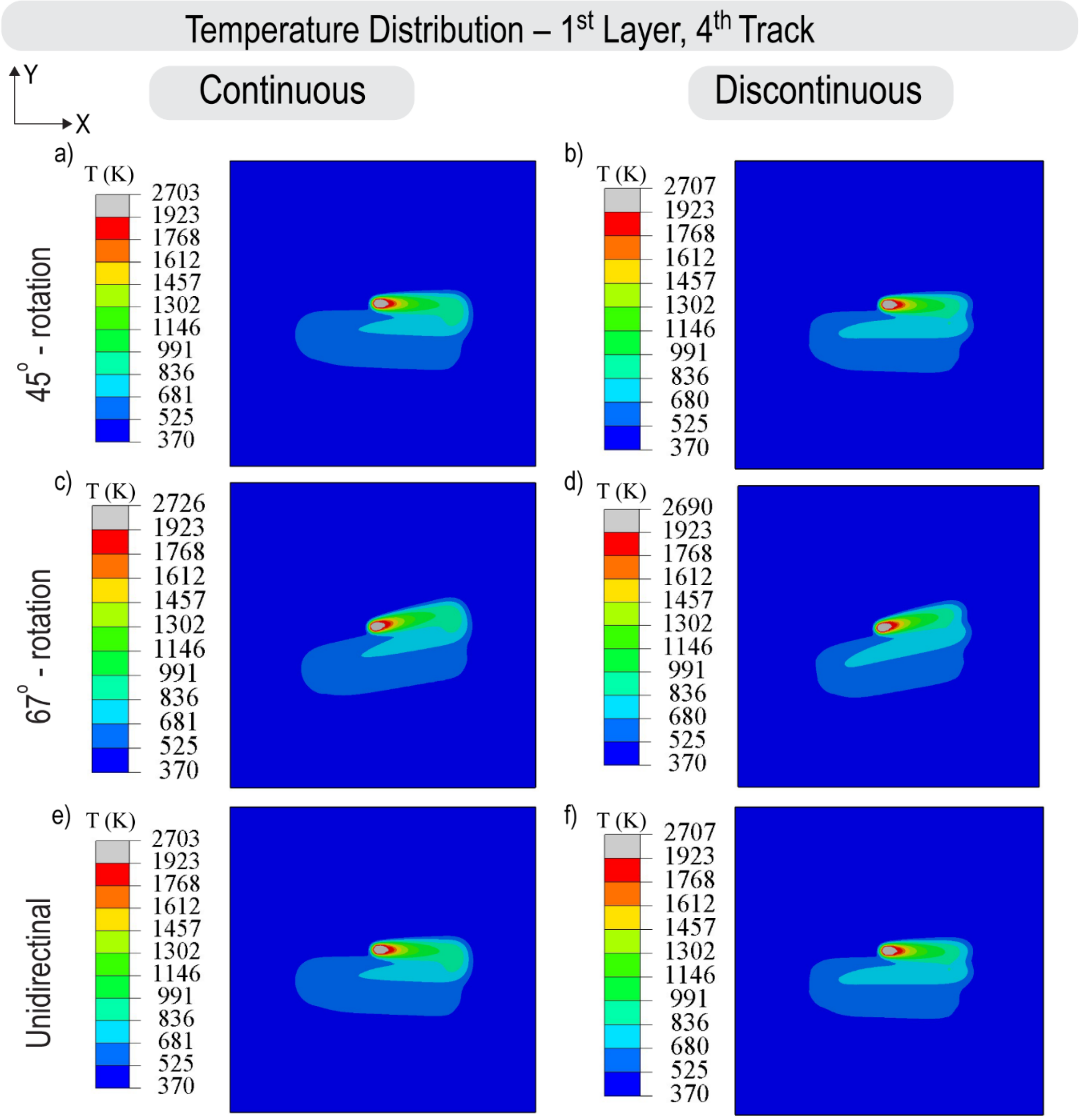

Fig. 34 Simulated temperature distributions for the 1st layer, 4th track in L-PBF under different scanning strategies. The left column shows continuous scanning strategies, and the right column shows discontinuous counterparts. Each row corresponds to a different rotation type: (a, b) 45° rotation, (c, d) 67° rotation, and (e, f) unidirectional scanning strategy.

The left column consists of continuous 45° rotation, 67° rotation, and unidirectional scanning strategies and the right columns include the discontinuous ones. The temperature ranges from 370 K (pre-heating temperature) to over 2700 K. The zones with temperature higher than 1923 K (melting temperature of Ti-6Al-4V) are colored as gray to represent molten pool. The shape and extent of the melt pool is almost similar. In continuous 45° rotation, the thermal profile is asymmetric.

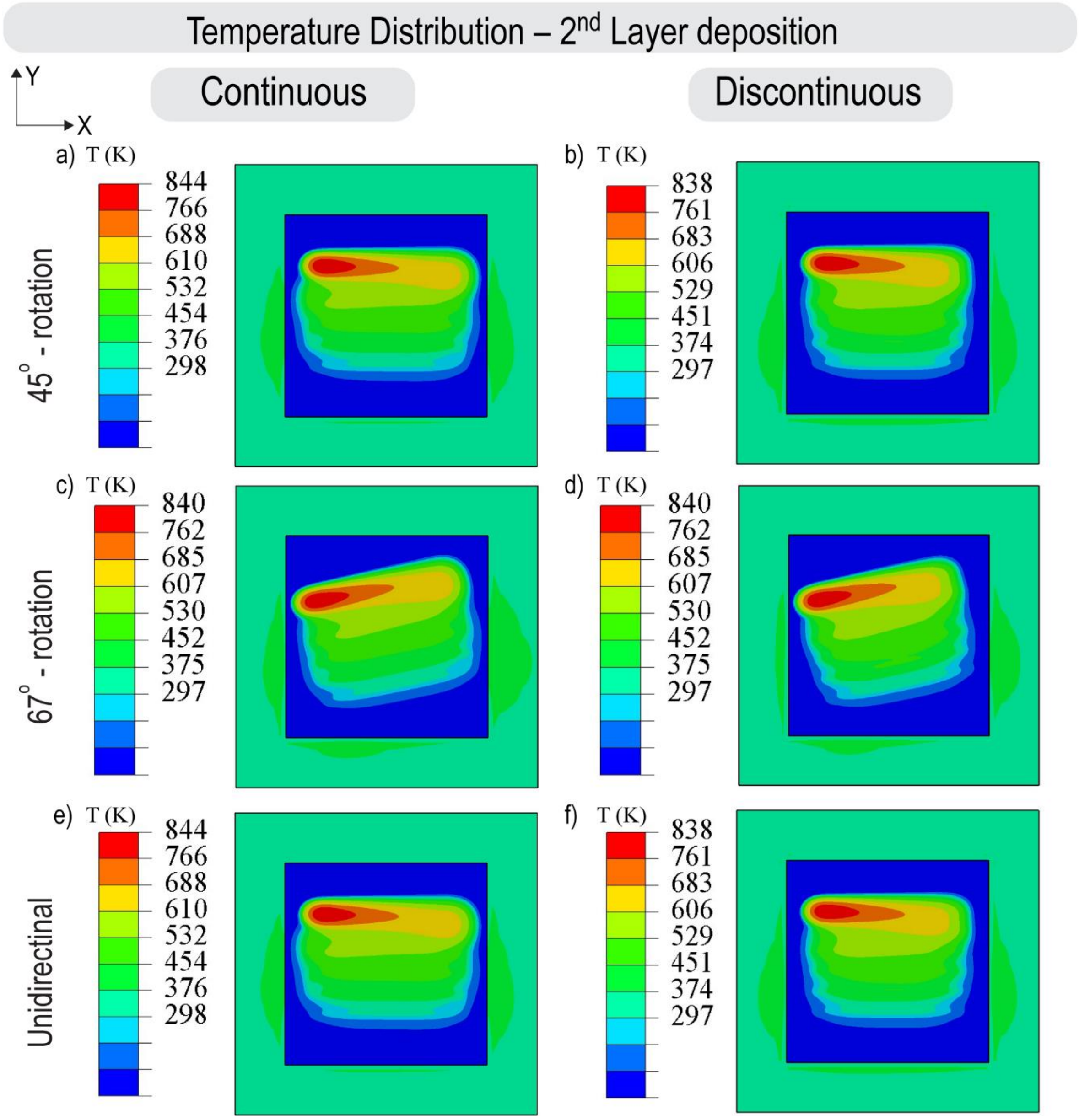

Fig 35 Simulated temperature distributions during the 2nd layer deposition for different scanning strategies in L-PBF. The left column shows results for continuous scanning, and the right column for discontinuous scanning. Each row represents a distinct scanning pattern: (a, b) 45° rotation, (c, d) 67° rotation, and (e, f) unidirectional scanning.

Then, after completing the first layer, the second layer is deposited with an interlayer time of 0.001 s, as depicted in Fig. 35. When the second layer is deposited, the thermal load is transferred into it. While the first-layer scanning vectors of the 45° rotation and unidirectional strategies appear similar (Fig. 34a, b, e, and f), their long-term thermal behavior and stress outcomes differ.

Over successive layers, the rotational scanning pattern helps distribute heat more evenly and reduce directional thermal gradients, which contributes to slightly lower residual stress in the 45° rotation strategy compared to the unidirectional one, as confirmed by experimental results. It is challenging to clearly distinguish differences in the uniformity and homogeneity of the temperature contours between the continuous and discontinuous scanning strategies. In the continuous contours (Fig. 35a, 35c, and 35e), regions shaded in light green (approximately $T > 600$ K) are longer and narrower compared to those in the discontinuous strategies. This is due to the absence of heat flux in the hatch direction between adjacent scan tracks. The percentage of regions experiencing temperatures above 500 K is slightly higher in the discontinuous strategy, while the peak temperature is slightly lower. Therefore, temperature contours in continuous scanning patterns appear more uniform and homogeneous, a smaller area reaches high temperatures compared to the discontinuous pattern.

However, continuous patterns may lead to greater heat accumulation and delayed cooling during the fabrication (500 layers), which results in larger thermal contraction between the layers. On the other hand, the discontinuous strategies allow stress relaxation during the scanning by applying interruption which may yield to lower residual stress.

Although continuous hatching produces a more homogeneous temperature field at the inter-layer wait time, the greater heat accumulation and delayed cooling give rise to larger thermal-contraction mismatches; the discontinuous pattern interrupts that build-up, allowing in-process stress relaxation and therefore yields lower residual stresses, as confirmed by XRD.

Fig. 36 shows the end of the 6th laser track in layer 2. Due to the different scanning patterns in the second layer, the temperature contours for the 45° rotation strategy differ from those of the unidirectional strategy.

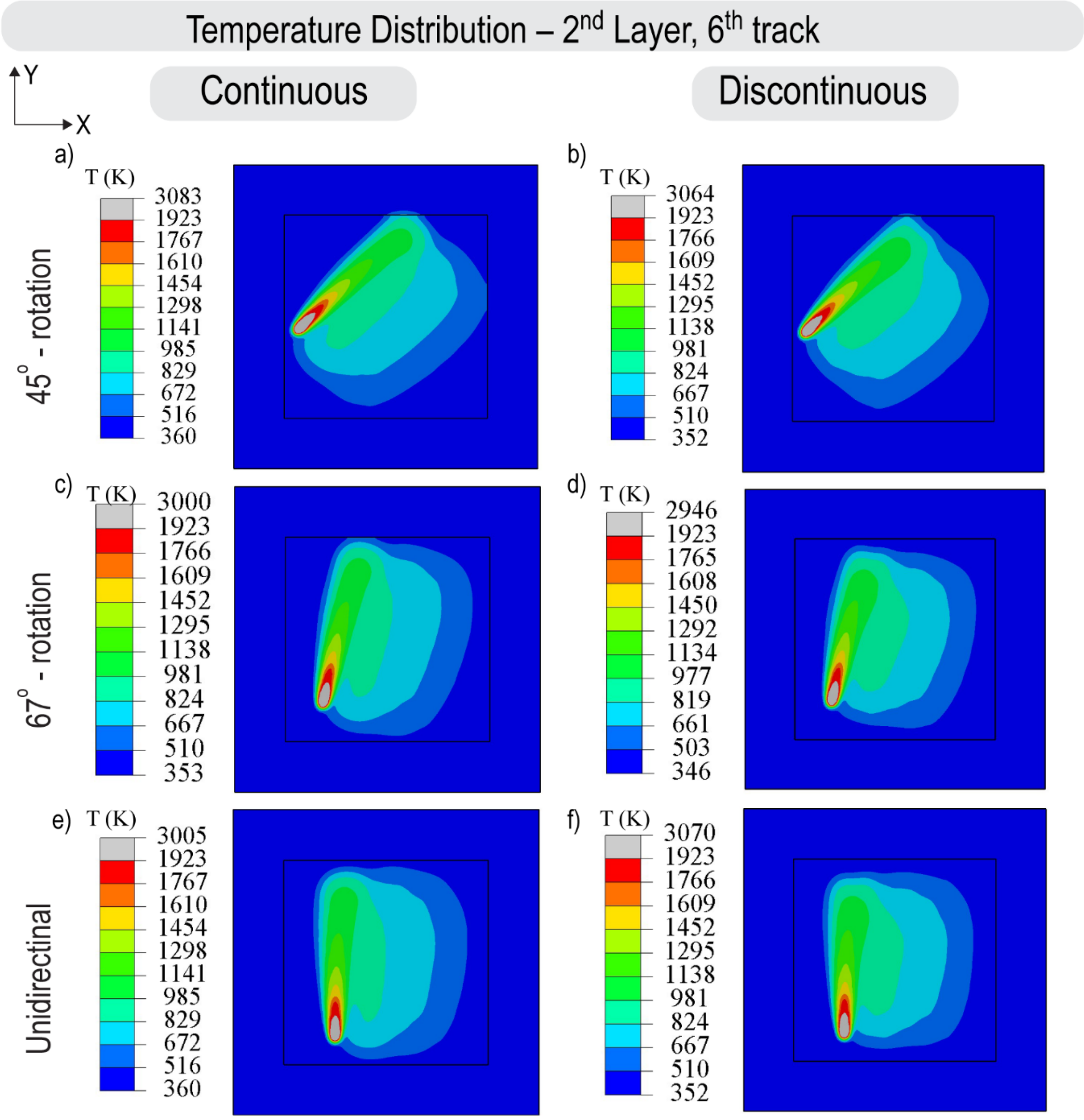

Fig. 36 Temperature distributions in the 2nd layer, 6th track of the L-PBF process for various scanning strategies. The left column represents continuous scanning, and the right column shows discontinuous scanning. Each row corresponds to a specific scan pattern: (a, b) 45° rotation, (c, d) 67° rotation, and (e, f) unidirectional.

The continuous scanning patterns still exhibit better temperature gradients, as the entire region remains relatively hot. In contrast, the discontinuous patterns display more tightly packed contours, indicating steeper local gradients but lower average and peak temperatures compared to the continuous case. For example, the peak temperature for the continuous 45°

strategy reaches 3083 K, while it is slightly lower at 3064 K for the discontinuous 45° strategy (Fig. 36a and 36b). As discussed earlier, this difference can be attributed to the uninterrupted motion of the laser in continuous scanning, which results in more efficient heat input and greater thermal accumulation.

Once again, the shape and extent of the high-temperature regions vary depending on the scanning pattern. Continuous strategies tend to produce more elongated melt pools and hot zones aligned with the laser path, whereas discontinuous strategies lead to more localized, confined hot regions.

Although continuous scanning promotes a more uniform and homogeneous temperature distribution at the track scale, the uninterrupted laser movement leads to higher peak temperatures and greater heat accumulation over time. This can increase thermal contraction mismatches and thus elevate residual stress levels — especially in long builds with many layers. On the other hand, discontinuous scanning introduces brief cooling periods between each laser track, which can help reduce thermal gradients and slightly lower the peak temperatures. For example, the peak temperature for the discontinuous 67° rotation is 2946 K (Fig. 34d) which is the lowest among all. It's important to note that these observations are based on simulations of just two layers, whereas actual components are typically fabricated using around 500 layers.

Table 20 summarizes the findings relating to the peak temperatures (in K) at the end of the first and second layers during the simulation of different scanning strategies in the L-PBF process. The results show that the peak temperatures at the end of the first layer are relatively similar across all strategies, with only minor variations. This is expected, as all simulations used the same laser power, scanning speed, and laser beam radius, and the initial layer interacts directly with the baseplate, which acts as a strong heat sink. In contrast, more significant differences appear at the end of the second layer, due to heat accumulation and changes in the scanning pattern and heat flux direction. Among the continuous strategies, the 67° rotation exhibits the lowest peak temperature (3000 K), notably lower than both the continuous 45° rotation (3083 K) and the continuous unidirectional strategy (3005 K). This suggests that rotation alone — even without interruption — contributes to more efficient heat distribution and reduced thermal buildup. This observation is consistent with the experimental data, where continuous 67° rotation produced a residual stress of 280 MPa, which is significantly lower than the other continuous strategies. Overall, discontinuous scanning strategies exhibit lower peak temperatures than their continuous counterparts, suggesting that the interruption in laser movement allows for partial cooling and reduces thermal accumulation during the fabrication.

Table 20. Peak temperatures (in K) at the end of the first and second layers for different scanning strategies in simulation of L-PBF.

		Peak temperature (K) at end of:	
Scanning strategy		First layer	Second layer
Continuous	45° rotation	2735	3083
	67° rotation	2715	3000
	Unidirectional	2735	3005
Discontinuous	45° rotation	2728	3064
	67° rotation	2717	2946
	Unidirectional	2728	3070

4.6. Static analysis

Thermal analysis reveals essential information about the thermal history of the part and its temperature distribution. However, static analysis is still essential to evaluate the residual stresses induced during the fabrication process. Fig. 37 illustrates Von Mises' stress contours for the different scanning strategies. The left column represents continuous scanning strategies, and the right column represents discontinuous ones. The Von Mises stress is an equivalent stress that reveals information about the overall stress state of the component.

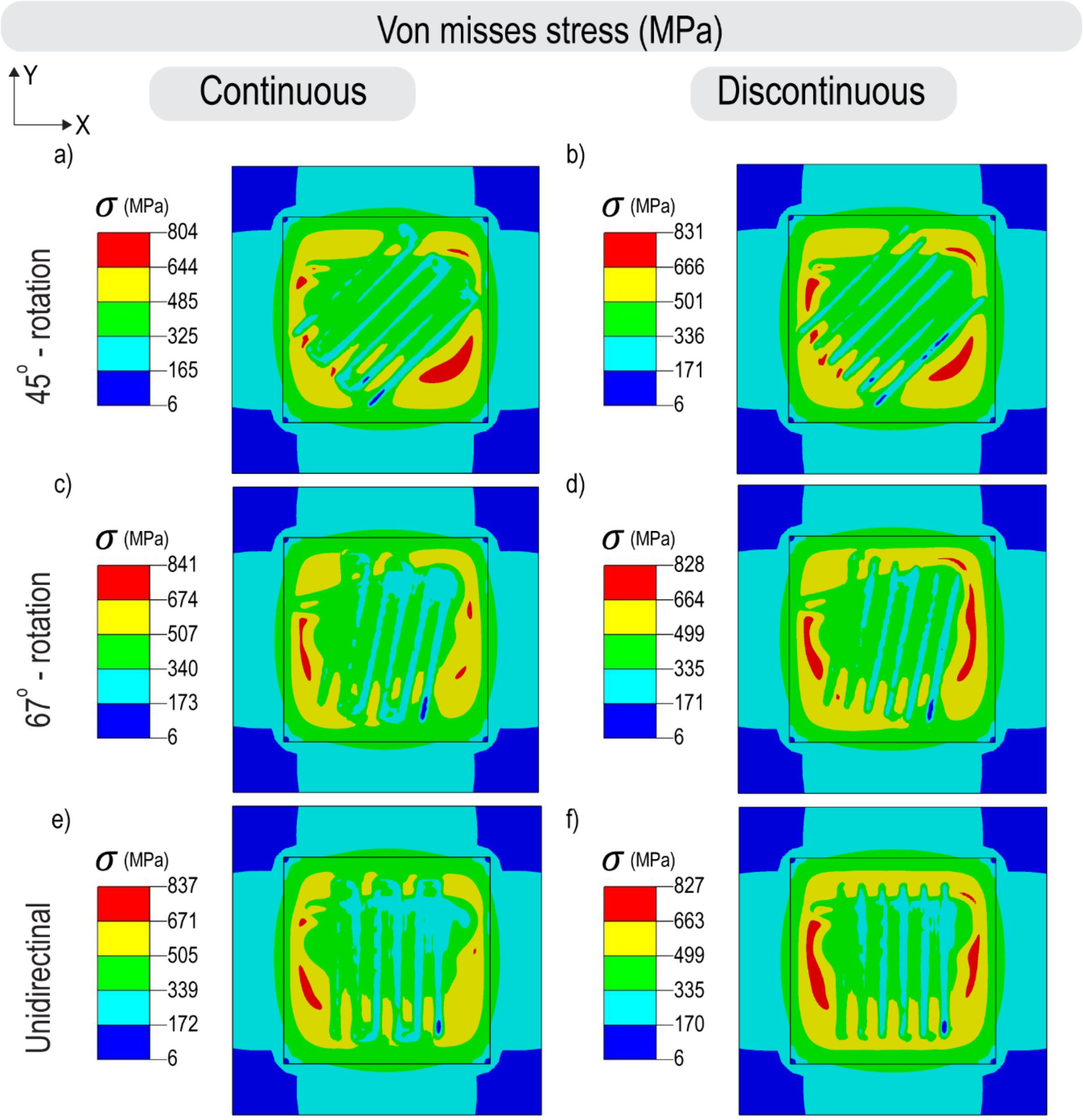

Fig. 37 Simulated von Mises stress distribution (in MPa) in top surface for different scanning strategies. The left column illustrates continuous scanning modes, while the right column corresponds to discontinuous counterparts. Each row represents a different scanning strategy: (a, b) 45° rotation, (c, d) 67° rotation, and (e, f) unidirectional.

There are three primary ways to analyze the residual stress fields: (1) the maximum stress value, (2) the overall distribution and extent of high-stress zones (typically visualized in red and yellow), and (3) the transitions between stress regions. Based on Fig. 37, the continuous 67° rotation strategy exhibited the best performance in mitigating residual stress among the continuous scanning strategies. As shown in Fig. 37c, the red regions representing high tensile stress are less extensive compared to other continuous patterns. A direct comparison between the continuous 67° rotation (Fig. 37c) and the continuous unidirectional pattern (Fig. 37e) reveals that the stress distribution is more uniform in Fig. 37c. This is evident from the smoother transition between the green and light blue areas in the continuous 67° scanning strategy. Furthermore, although the continuous 45° rotation exhibits more concentrated red regions—indicative of high tensile stress—the peak tensile stress is limited to 804 MPa. A more uniform stress pattern is also observed in the top-right area of the scan, where a smooth transition exists between stress levels ranging from 325 MPa to 485 MPa.

On the other hand, despite the results obtained from XRD measurements, discontinuous scanning strategies do not necessarily perform better than continuous ones. For instance, in Fig. 37d, although the peak tensile stress is reduced, the red zones—indicating higher stress concentrations—have become larger. However, one advantage of discontinuous strategies is improving uniformity of the stress field. For example, in both the discontinuous 67° rotation and discontinuous unidirectional patterns, the transition between scanning paths (from blue to green regions) is smoother, indicating a lower stress gradient and a more homogeneous stress distribution in comparison to the continuous ones.

Among the discontinuous strategies, the unidirectional pattern appears less effective in mitigating residual stress, as it shows a larger area with approximately 350 MPa, providing a higher stress gradient. The 45° rotation strategy enhances stress uniformity but also leads to a larger red region (~831 MPa) compared to the 67° rotation pattern. Overall, the discontinuous 67° rotation scanning strategy may demonstrate the best balance between reducing peak stress and achieving a uniform stress distribution.

Nevertheless, Fig. 37 reveals that discontinuous scanning strategies tend to produce more uniform stress fields but may also introduce regions with higher localized stress. Therefore, it is challenging to definitively conclude whether continuous or discontinuous strategies perform better in mitigating residual stress, based solely on Fig. 37 and compare the finidngs with the measurement data obtained from XRD. Moreover, although X-ray diffraction is a widely used technique for residual stress measurement, its application to components fabricated via L-PBF involves several limitations that can affect accuracy.

One major source of error is the surface roughness of as-built L-PBF parts, which can lead to irregular X-ray scattering. Additionally, the shallow penetration depth of X-rays—typically limited to just a few micrometers—may not accurately capture subsurface or bulk residual stress states. The position of the equipment and the location where the data are collected also play a significant role in measurement accuracy. Plus, it should be noted that residual stress results from both thermal load and stresses accumulation over time. The current model simulated only two layers of fabrication, whereas real printed parts consist of hundreds of layers (e.g., ~500 layers), which could significantly influence the final residual stress state.

In conclusion, Table 21 ranks the different scanning strategies based on their effectiveness in reducing high tensile regions (represented in red and yellow) and achieving a more uniform stress field. A rank of 1 indicates the most effective strategy, while a rank of 6 represents the least effective.

Table 21 Qualitative comparison of residual stress distribution in Ti-6Al-4V parts fabricated by L-PBF under different scanning strategies, based on the number of high-stress regions and the of stress uniformity (lower values indicate better performance)

Scanning strategy		High stress regions	Uniformity
Continuous	45° rotation	3	3
	67° rotation	1	5
	Unidirectional	2	6
Discontinuous	45° rotation	6	4
	67° rotation	4	1
	Unidirectional	5	2

Table 21 highlights a key trade-off between minimizing high-stress regions and achieving uniformity. While some continuous strategies—such as the 67° rotation continuous—perform very well in reducing high-stress areas (ranked 1), they often fall short in terms of uniformity (ranked 5). On the other hand, discontinuous strategies, particularly the 67° rotation discontinuous, excel in producing a more uniform stress field (ranked 1) but tend to show slightly more high-stress regions (ranked 4).

When it comes to effectively mitigating residual stress, the most desirable outcome is a uniformly distributed compressive stress field. Among the strategies evaluated, the discontinuous 67° rotation stands out as the most promising in this regard. Although Table 21 indicates it may have more high-stress regions compared to its continuous counterpart, its uniformity offers a major advantage. A uniform stress field reduces variability and minimizes the risk of localized weak points that could lead to distortion or failure.

For further investigation, the stresses along the x-direction and y-direction are presented in Fig. 38 and Fig. 39. As shown in Fig. 38, continuous scanning strategies tend to produce a wider and more concentrated compressive stress region (indicated by dark blue areas). In contrast, discontinuous strategies result in a more balanced and uniform stress distribution, with less stress concentration—evidenced by an increased percentage of green and light blue regions. For example, in the continuous 45° rotation strategy, the maximum compressive stress (~−700 MPa) covers approximately 13% of the surface area. However, when the strategy shifts to a discontinuous pattern, the coverage of the maximum compressive region decreases to around 8%.

Despite this improvement, high-stress regions (represented in red) are still visible in Fig. 38b, highlighting the limited effectiveness of the 45° rotation strategy in reducing these areas. The 45° continuous rotation exhibits high-stress concentrations along the diagonal direction, perpendicular to the scanning tracks. This is evident from the sharp division between light blue and green areas, indicating that it may be the least effective continuous strategy for achieving uniform stress distribution. Furthermore, the continuous 67° rotation performs better than the continuous unidirectional strategy in reducing high tensile regions, with a lower maximum tensile value of 37 MPa compared to 56 MPa.

Among the continuous patterns, the 67° rotation strategy demonstrates a more uniform stress distribution, with smoother transitions between green and blue regions, in contrast to the continuous unidirectional strategy.

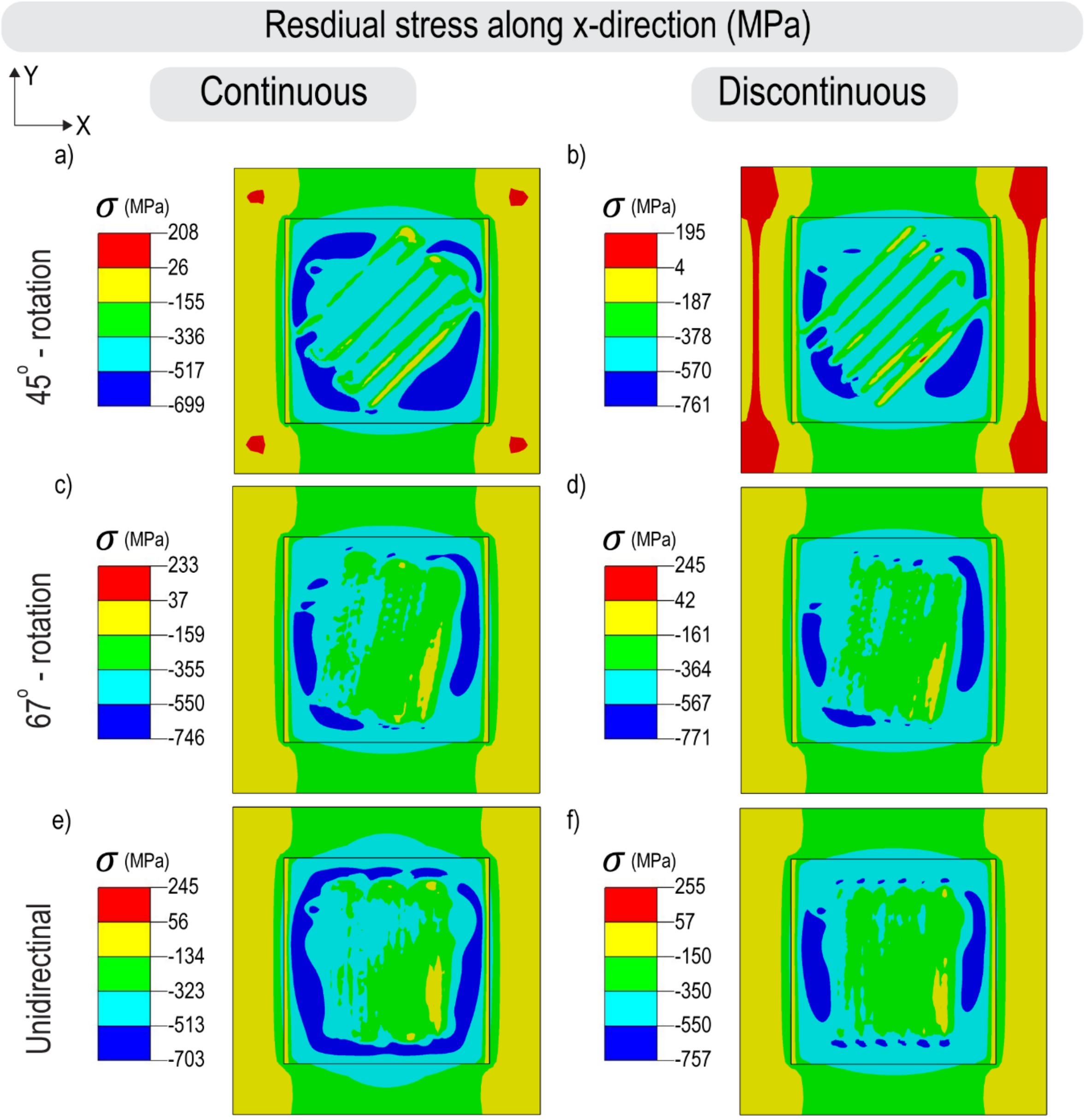

Fig 38 Simulated residual stress distribution along the X-direction (in MPa) in top surface for different scanning strategies. The left column illustrates continuous scanning modes, while the right column corresponds to discontinuous counterparts. Each row represents a different scanning strategy: (a, b) 45° rotation, (c, d) 67° rotation, and (e, f) unidirectional.

Similar to the von Mises stress results, discontinuous scanning strategies perform better in achieving a more uniform stress field compared to continuous ones. However, while the discontinuous 67° rotation pattern presents a lower high tensile stress (~42 MPa), it simultaneously shows reduced uniformity, with sharp transitions between compressive stress regions, particularly near the center of the scanned area. This trade-off suggests that the discontinuous unidirectional strategy is more effective in mitigating localized high tensile stresses in the x-direction, offering a good balance between stress reduction and field uniformity. The discontinuous 67° rotation also demonstrates a relatively effective approach for reducing residual stress in the x-direction, though with some loss in uniformity.

In contrast, both the continuous and discontinuous 45° rotation strategies appear to be the least effective in mitigating residual stress along the x-direction. They result in the lowest level of uniformity among all scanning strategies considered, making them less suitable for applications where consistent stress distribution is critical.

Fig. 39 presents the residual stress distribution in the y-direction for different scanning strategies. As shown in Fig. 38a, the continuous 45° rotation strategy exhibits the largest region of high tensile residual stress among all the scanning patterns. Similarly, the discontinuous 45° rotation displays a larger yellow region compared to other strategies, indicating a higher presence of tensile stress.

In contrast, both the 67° rotation and unidirectional strategies perform well in reducing high tensile stress regions and promoting a more uniform stress field. Among all simulated strategies, the discontinuous unidirectional pattern offers the most desirable stress profile—approximately 24% of the surface area is under compressive stress, with a peak compressive value of −757 MPa. This improved performance is likely related to the laser track orientation, which minimizes direct shrinkage along the y-axis and helps balance residual stress accumulation. Only a narrow yellow tensile region appears near the edge (~84 MPa), which may serve to compensate for residual contraction at the boundary.

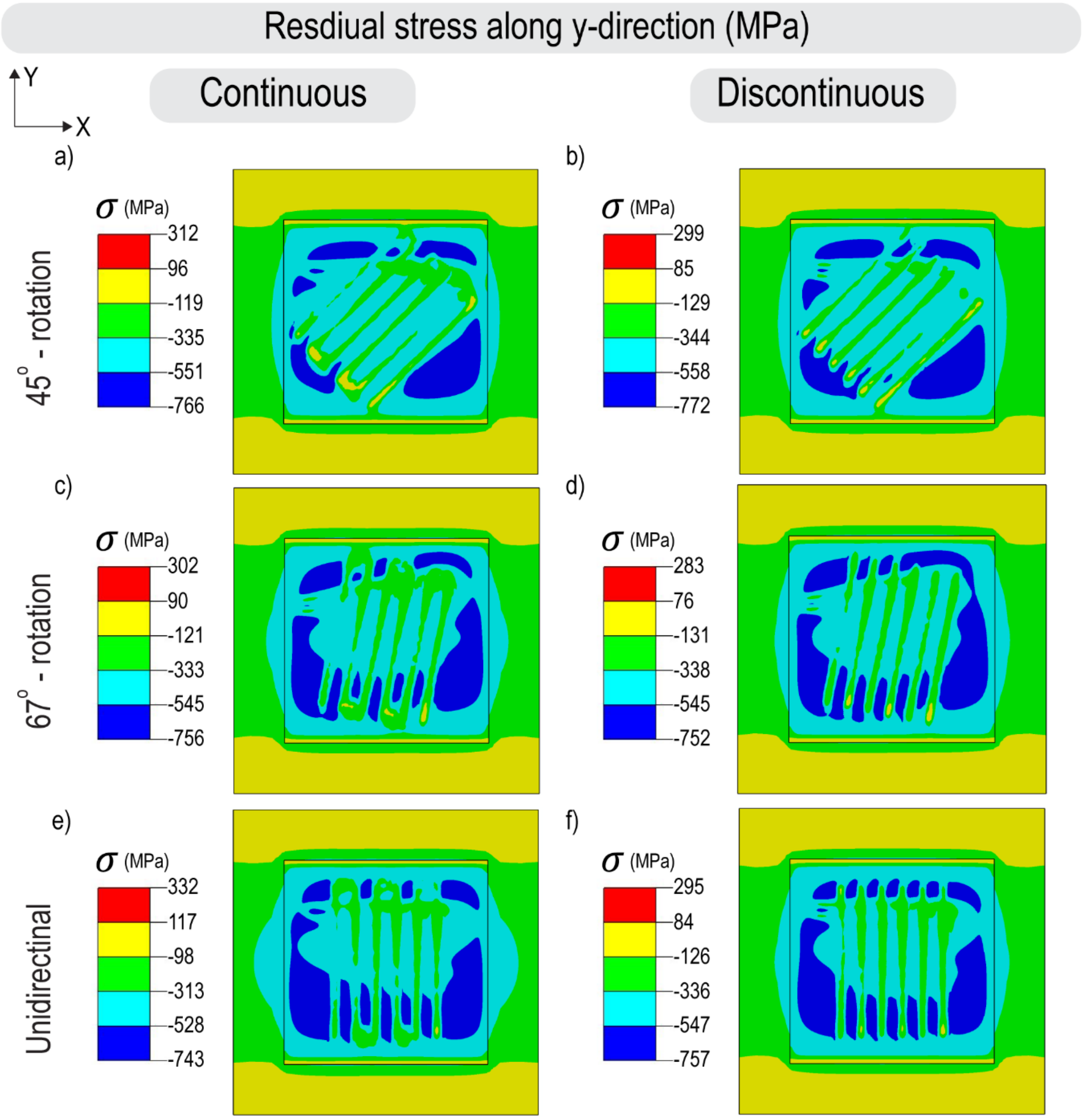

Fig. 39 Simulated residual stress distribution along the Y-direction (in MPa) in top surface for different scanning strategies. The left column illustrates continuous scanning modes, while the right column corresponds to discontinuous counterparts. Each row represents a different scanning strategy: (a, b) 45° rotation, (c, d) 67° rotation, and (e, f) unidirectional.

The discontinuous 67° rotation also performs effectively, generating a relatively uniform stress profile by reducing large concentrated compressive zones (dark blue) and shifting them toward more moderate compressive regions (green), especially when compared to its continuous one. This change may indicate a useful redistribution of stress, helping to reduce local gradients and minimize distortion risk along the y-direction.

Table 22 represents comparative ranking of scanning strategies for mitigation of residual stress in general. Based on Table 22, discontinuous 67° rotation scanning strategy performs the best in mitigation of residual stress, by producing the most uniform and balanced residual stress field with minimized σ_{vm} and σ_x, while reducing compressive σ_y areas. In contrast, continuous unidirectional scanning exhibits the least effective approach to mitigate residual stress due to heat accumulation along long tracks and extensive high stress zones.

Table 22 Ranking of scanning strategies based on their effectiveness in residual stress mitigation during the simulation.

Scanning Strategy	Level	Details
67° rotation – Discontinuous	1	• Best overall performance: low σ_{vm} , uniform field, low σ_x, moderate σ_y
67° rotation – Continuous	2	• Very low σ_{vm}, best among continuous, but less uniform in σ_y
Unidirectional– Discontinuous	3	• Good stress balance; high compressive σ_y, minimal high tensile zones
45° rotation – Discontinuous	4	• Moderate uniformity but high peak σ_{vm} and σ_y
45° rotation – Continuous	5	• Diagonal stress bands, low uniformity, high σ_y and stress gradients
Unidirectional – Continuous	6	• Least effective: high σ_{vm}, severe directional accumulation, poor stress redistribution

5. Conclusion and future aspects

This study tried to investigate the effects of various scanning strategies on mitigation of residual stress and temperature distribution in Ti-6Al-4V parts fabricated using Laser Powder Bed Fusion (L-PBF). A combination of experimental analyses, including 3D X-ray CT, surface roughness, hardness test, and XRD residual stress measurement and numerical simulations were applied to evaluate six different scanning strategies. Three continuous and three discontinuous with rotation angles of 45°, 67°, and unidirectional paths.

The results revealed that discontinuous scanning strategies generally perform better in mitigating defects and reducing residual stress. For instance, the discontinuous 67° rotation strategy exhibited the most balanced performance, achieving a high relative density of 99%, lowest residual stress of 220 MPa, uniform stress distribution, and reduced peak temperatures.

Furthermore, CT analysis demonstrated 45° rotation yielded the lowest density (97%) due to poor overlap and potential keyhole formation, whereas discontinuous approaches reduced porosity. Similarly, surface roughness data indicated that discontinuous scanning improves surface finish in rotated strategies.

Moreover, thermal simulations showed that continuous scanning generates more uniform temperature fields but leads to higher peak temperatures and more thermal accumulation in successive layers, possibly resulting in increasing residual stress. In contrast, discontinuous strategies reduced peak temperatures, effectively lowering stress concentrations.

Thermal–mechanical simulations provided deeper insights into the stress distribution and validated the trends observed in the experiments. Analysis of von Mises stress, along with residual stress in the x- and y-directions, demonstrated that discontinuous scanning strategies generally lead to more uniform stress fields, although they may introduce localized high-stress regions. In contrast, continuous strategies, particularly unidirectional ones, often resulted in concentrated tensile stress zones and poor uniformity due to repetitive heat input along fixed paths.

Among all scanning strategies, the discontinuous 67° rotation approach emerged as the most effective in achieving a balanced and homogeneous residual stress field, with favorable performance across all evaluated stress components. While some continuous strategies, such as 67° rotation continuous, also performed well in reducing peak stress, they were less effective in promoting uniform stress distribution. Furthermore, the numerical model, which simulated only two layers, does not fully capture the cumulative effects seen in real builds with hundreds of layers. Despite these limitations, the combined experimental and simulation results provide a valuable framework for understanding and optimizing scanning strategies in L-PBF.

In summary, the outcome of this research emphasizes the importance of scanning strategy, particularly the use of rotational and discontinuous patterns in mitigation of residual stress and improving build quality in L-PBF.

For future work, with provided thermal and static analysis, the influence of scanning strategy on the fatigue life of printed components can be investigated. Both high-cycle and low-cycle fatigue tests can be conducted to correlate residual stress distributions with crack initiation and propagation behavior under cyclic loading.

While this study focused on two-layer simulations for computational efficiency, adding more layers and defining more rotations between the successive layers would provide more accurate temperature distribution and stress field.

Integration of data-driven models, such as machine learning, with simulation and experimental data could accelerate the optimization of scanning strategies by predicting residual stress and under varying parameters such as scanning strategy and laser powers.

Data availability: Not Applicable

Conflict of interest: The authors declare that they have no conflicts of interest to disclose.

6. References

[1] C. W. Hull and C. Arcadia, “United States Patent (19) Hull (54)(75)(73) 21) 22 (51) 52)(58)(56) APPARATUS FOR PRODUCTION OF THREE-DMENSONAL OBJECTS BY STEREO THOGRAPHY,” 1984, *Aug.*

[2] P. Pradel, Z. Zhu, R. Bibb, and J. Moultrie, “Complexity Is not For free : The impact of component complexity on additive manufacturing build time This item was submitted to Loughborough University ’ s Institutional Repository of component complexity on additive manufacturing,” 2017. [Online]. Available: https://hdl.handle.net/2134/24338

[3] E. Lannunziata, M. H. Mosallanejad, M. Galati, G. Piscopo, and A. Saboori, “Analyzing the Interplay of Sintering Conditions on Microstructure and Hardness in Indirect Additive Manufacturing of 17-4PH Stainless Steel,” *Acta Metall. Sin. (English Lett.*, vol. 37, no. 9, pp. 1611–1620, 2024, doi: 10.1007/s40195-024-01745-6.

[4] A. Behjat *et al.*, “A novel titanium alloy for load-bearing biomedical implants: Evaluating the antibacterial and biocompatibility of Ti536 produced via electron beam powder bed fusion additive manufacturing process,” *Biomater. Adv.*, vol. 163, p. 213928, 2024, doi: https://doi.org/10.1016/j.bioadv.2024.213928.

[5] P.-H. Lee, H. Chung, S. W. Lee, J. Yoo, and J. Ko, “Review: Dimensional Accuracy in Additive Manufacturing Processes,” Jun. 09, 2014. doi: 10.1115/MSEC2014-4037.

[6] S. Yang, Y. Tang, and Y. F. Zhao, “A new part consolidation method to embrace the design freedom of additive manufacturing,” *J. Manuf. Process.*, vol. 20, pp. 444–449, 2015, doi: https://doi.org/10.1016/j.jmapro.2015.06.024.

[7] A. behjat, A. Saboori, M. Galati, and L. Iuliano, “The electrochemical behaviour of Ti-48Al-2Cr-2Nb produced by electron beam powder bed fusion process,” *Intermetallics*, vol. 175, p. 108472, 2024, doi: https://doi.org/10.1016/j.intermet.2024.108472.

[8] M. S. Safavi, A. Bordbar-Khiabani, J. Khalil-Allafi, M. Mozafari, and L. Visai, “Additive Manufacturing: An Opportunity for the Fabrication of Near-Net-Shape NiTi Implants,” 2022. doi: 10.3390/jmmp6030065.

[9] M. Sæterbø and W. D. Solvang, “Evaluating the cost competitiveness of metal additive manufacturing – A case study with metal material extrusion,” *CIRP J. Manuf. Sci. Technol.*, vol. 45, pp. 113–124, 2023, doi: https://doi.org/10.1016/j.cirpj.2023.06.005.

[10] S. Galjaard, S. Hofman, and S. Ren, “New Opportunities to Optimize Structural Designs in Metal by Using Additive Manufacturing BT - Advances in Architectural Geometry 2014,” P. Block, J. Knippers, N. J. Mitra, and W. Wang, Eds., Cham: Springer International Publishing, 2015, pp. 79–93.

[11] J. Nyika and M. O. Dinka, “Additive manufacturing for sustainable use of resources,” in *Utilizing Technology for Sustainable Resource Management Solutions*, IGI Global, 2024, pp. 59–73. doi: 10.4018/979-8-3693-2346-5.ch005.

[12] A. Saboori, D. Gallo, S. Biamino, P. Fino, and M. Lombardi, “An Overview of Additive Manufacturing of Titanium Components by Directed Energy Deposition: Microstructure and Mechanical Properties,” 2017. doi: 10.3390/app7090883.

[13] O. Santoliquido, P. Colombo, and A. Ortona, “Additive Manufacturing of ceramic components by Digital Light Processing: A comparison between the ‘bottom-up’ and the ‘top-down’ approaches,” *J. Eur. Ceram. Soc.*, vol. 39, no. 6, pp. 2140–2148, 2019, doi: https://doi.org/10.1016/j.jeurceramsoc.2019.01.044.

[14] M. H. Mosallanejad, B. Niroumand, A. Aversa, and A. Saboori, “In-situ alloying in laser-based additive manufacturing processes: A critical review,” *J. Alloys Compd.*, vol. 872, p. 159567, 2021, doi: https://doi.org/10.1016/j.jallcom.2021.159567.

[15] J. Huang, Q. Qin, and J. Wang, “A Review of Stereolithography: Processes and

Systems," 2020. doi: 10.3390/pr8091138.

[16] J. Nandy, H. Sarangi, and S. Sahoo, "A Review on Direct Metal Laser Sintering: Process Features and Microstructure Modeling," *Lasers Manuf. Mater. Process.*, vol. 6, no. 3, pp. 280–316, 2019, doi: 10.1007/s40516-019-00094-y.

[17] M. H. Mosallanejad, R. Ghanavati, A. Behjat, M. Taghian, A. Saboori, and L. Iuliano, "Untapped Opportunities in Additive Manufacturing with Metals: From New and Graded Materials to Post-Processing," 2024. doi: 10.3390/met14040425.

[18] M. Galati, M. Giordano, A. Saboori, and S. Defanti, "Electron beam powder bed fusion of Ti-6Al-2Sn-4Zr-2Mo lattice structures: morphometrical and mechanical characterisations," *Int. J. Adv. Manuf. Technol.*, vol. 131, no. 3, pp. 1223–1239, 2024, doi: 10.1007/s00170-024-13148-z.

[19] S. Hossein Nedjad, M. Yildiz, and A. Saboori, "Solidification behaviour of austenitic stainless steels during welding and directed energy deposition," *Sci. Technol. Weld. Join.*, vol. 28, no. 1, pp. 1–17, Jan. 2023, doi: 10.1080/13621718.2022.2115664.

[20] A. Abdali, S. Hossein Nedjad, H. Hamed Zargari, A. Saboori, and M. Yildiz, "Predictive tools for the cooling rate-dependent microstructure evolution of AISI 316L stainless steel in additive manufacturing," *J. Mater. Res. Technol.*, vol. 29, pp. 5530–5538, 2024, doi: https://doi.org/10.1016/j.jmrt.2024.03.008.

[21] A. Saboori *et al.*, "Effect of heat treatment on microstructural evolution of additively manufactured inconel 718 and cast alloy," 2019. [Online]. Available: https://www.researchgate.net/publication/336642913_Effect_of_heat_treatment_on_microstructural_evolution_of_additively_manufactured_Inconel_718_and_cast_alloy

[22] F. Calignano, M. Pavese, A. Saboori, M. Galati, and L. Iuliano, "Additive manufacturing of copper with a single mode IR fiber laser," *Procedia CIRP*, vol. 118, pp. 649–653, 2023, doi: https://doi.org/10.1016/j.procir.2023.06.111.

[23] P. Mofazali, M. Atapour, M. Nakamura, M. Sheikholeslam, M. Galati, and A. Saboori, "Surface modification of additive manufactured Ti6Al4V scaffolds with gelatin/alginate- IGF-1 carrier: An effective approach for healing bone defects," *Int. J. Biol. Macromol.*, vol. 265, p. 131125, 2024, doi: https://doi.org/10.1016/j.ijbiomac.2024.131125.

[24] A. Dagkolu, I. Gokdag, and O. Yilmaz, "Design and additive manufacturing of a fatigue-critical aerospace part using topology optimization and L-PBF process," *Procedia Manuf.*, vol. 54, pp. 238–243, 2021, doi: https://doi.org/10.1016/j.promfg.2021.07.037.

[25] M. R. Bandekhoda, M. H. Mosallanejad, M. Atapour, L. Iuliano, and A. Saboori, "Investigation on the Potential of Laser and Electron Beam Additively Manufactured Ti–6Al–4V Components for Orthopedic Applications," *Met. Mater. Int.*, vol. 30, no. 1, pp. 114–126, 2024, doi: 10.1007/s12540-023-01496-6.

[26] M. Salmi, K.-S. Paloheimo, J. Tuomi, J. Wolff, and A. Mäkitie, "Accuracy of medical models made by additive manufacturing (rapid manufacturing)," *J. Cranio-Maxillofacial Surg.*, vol. 41, no. 7, pp. 603–609, 2013, doi: https://doi.org/10.1016/j.jcms.2012.11.041.

[27] A. Saboori, A. Aversa, G. Marchese, S. Biamino, M. Lombardi, and P. Fino, "Application of Directed Energy Deposition-Based Additive Manufacturing in Repair," 2019. doi: 10.3390/app9163316.

[28] R. Leal *et al.*, "Additive manufacturing tooling for the automotive industry," *Int. J. Adv. Manuf. Technol.*, vol. 92, no. 5, pp. 1671–1676, 2017, doi: 10.1007/s00170-017-0239-8.

[29] M. Taghian, M. H. Mosallanejad, E. Lannunziata, G. Del Greco, L. Iuliano, and A. Saboori, "Laser powder bed fusion of metallic components: Latest progress in productivity, quality, and cost perspectives," *J. Mater. Res. Technol.*, vol. 27, pp. 6484–

6500, 2023, doi: https://doi.org/10.1016/j.jmrt.2023.11.049.

[30] M. Tebianian *et al.*, “A Review of the Metal Additive Manufacturing Processes,” 2023. doi: 10.3390/ma16247514.

[31] A. Behjat *et al.*, “Enhanced surface properties and bioactivity of additively manufactured 316L stainless steel using different post-treatments,” *Mater. Today Proc.*, vol. 70, pp. 188–194, 2022, doi: https://doi.org/10.1016/j.matpr.2022.09.019.

[32] I. Aiza *et al.*, “Effects of build orientation and inclined features on physical, microstructural and mechanical properties of powder bed fusion additively manufactured metallic parts,” *Prog. Mater. Sci.*, vol. 147, p. 101357, 2025, doi: https://doi.org/10.1016/j.pmatsci.2024.101357.

[33] A. Abdi, M. S. Salehi, S. A. Fatemi, L. Iuliano, and A. Saboori, “Microstructure-induced anisotropic tribological properties of Sc-Zr modified Al–Mg alloy (Scalmalloy®) produced via laser powder bed fusion process,” *Int. J. Adv. Manuf. Technol.*, vol. 130, no. 1, pp. 755–779, 2024, doi: 10.1007/s00170-023-12691-5.

[34] J. Boban, P. M. Abhilash, A. Ahmed, and M. A. Rahman, “10.11 - An overview on post-processing of metal additive manufactured components,” S. B. T.-C. M. P. (Second E. Hashmi, Ed., Oxford: Elsevier, 2024, pp. 231–270. doi: https://doi.org/10.1016/B978-0-323-96020-5.00241-7.

[35] M. Kasprowicz, A. Pawlak, P. Jurkowski, and T. Kurzynowski, “Ways to increase the productivity of L-PBF processes,” *Arch. Civ. Mech. Eng.*, vol. 23, no. 3, p. 211, 2023, doi: 10.1007/s43452-023-00750-3.

[36] E. A. Patterson, J. Lambros, R. Magana-Carranza, and C. J. Sutcliffe, “Residual stress effects during additive manufacturing of reinforced thin nickel–chromium plates,” *Int. J. Adv. Manuf. Technol.*, vol. 123, no. 5, pp. 1845–1857, 2022, doi: 10.1007/s00170-022-10256-6.

[37] C. Bellini, F. Berto, V. Di Cocco, F. Iacoviello, L. P. Mocanu, and N. Razavi, “Additive manufacturing processes for metals and effects of defects on mechanical strength: a review,” *Procedia Struct. Integr.*, vol. 33, pp. 498–508, 2021, doi: https://doi.org/10.1016/j.prostr.2021.10.057.

[38] A. Behjat *et al.*, “Microstructure-electrochemical behavior relationship in post processed AISI316L stainless steel parts fabricated by laser powder bed fusion,” *J. Mater. Res. Technol.*, vol. 23, pp. 3294–3311, 2023, doi: https://doi.org/10.1016/j.jmrt.2023.01.229.

[39] T. DebRoy *et al.*, “Additive manufacturing of metallic components – Process, structure and properties,” *Prog. Mater. Sci.*, vol. 92, pp. 112–224, 2018, doi: https://doi.org/10.1016/j.pmatsci.2017.10.001.

[40] A. Behjat, E. Lannunziata, E. Gadalińska, L. Iuliano, and A. Saboori, “Improving the surface quality and mechanical properties of additively manufactured AISI 316L stainless steel by different surface post-treatment,” *Procedia CIRP*, vol. 118, pp. 771–776, 2023, doi: https://doi.org/10.1016/j.procir.2023.06.132.

[41] J. Li and S. Wang, “Distortion caused by residual stresses in machining aeronautical aluminum alloy parts: recent advances,” *Int. J. Adv. Manuf. Technol.*, vol. 89, no. 1, pp. 997–1012, 2017, doi: 10.1007/s00170-016-9066-6.

[42] M. Kaess, M. Werz, and S. Weihe, “Residual Stress Formation Mechanisms in Laser Powder Bed Fusion—A Numerical Evaluation,” 2023. doi: 10.3390/ma16062321.

[43] J. V Gordon, C. V Haden, H. F. Nied, R. P. Vinci, and D. G. Harlow, “Fatigue crack growth anisotropy, texture and residual stress in austenitic steel made by wire and arc additive manufacturing,” *Mater. Sci. Eng. A*, vol. 724, pp. 431–438, 2018, doi: https://doi.org/10.1016/j.msea.2018.03.075.

[44] H. Vemanaboina, P. Ferro, B. S. Babu, E. Gundabattini, K. Kumar, and F. Berto, “Residual Stress Distribution in Selective Laser Melting of SS316L Parts,” *Adv. Mater.*

Sci. Eng., vol. 2022, 2022, doi: 10.1155/2022/5687407.

[45] S. Srivastava, R. K. Garg, A. Sachdeva, and V. S. Sharma, "Distribution of Residual Stress in Wire-Arc Additively Manufactured Small-Scale Component: Single- Versus Multi-Level Heat Input," *J. Manuf. Sci. Eng.*, vol. 145, no. 2, Sep. 2022, doi: 10.1115/1.4055569.

[46] W.-J. Lai, A. Ojha, Z. Li, C. Engler-Pinto, and X. Su, "Effect of residual stress on fatigue strength of 316L stainless steel produced by laser powder bed fusion process," *Prog. Addit. Manuf.*, vol. 6, no. 3, pp. 375–383, 2021, doi: 10.1007/s40964-021-00164-8.

[47] K. Zeng *et al.*, "Layer by layer validation of geometrical accuracy in Additive Manufacturing processes," *24th Int. SFF Symp. - An Addit. Manuf. Conf. SFF 2013*, pp. 76–87, 2013, [Online]. Available: http://dx.doi.org/10.26153/tsw/15415

[48] S. Liu and Y. C. Shin, "Additive manufacturing of Ti6Al4V alloy: A review," *Mater. Des.*, vol. 164, p. 107552, 2019, doi: https://doi.org/10.1016/j.matdes.2018.107552.

[49] I. van Zyl, I. Yadroitsava, and I. Yadroitsev, "Residual stress in TI6AL4V objects produced by direct metal laser sintering," *South African J. Ind. Eng.*, vol. 27, no. 4, pp. 134–141, 2016, doi: 10.7166/27-4-1468.

[50] H. Ali, L. Ma, H. Ghadbeigi, and K. Mumtaz, "In-situ residual stress reduction, martensitic decomposition and mechanical properties enhancement through high temperature powder bed pre-heating of Selective Laser Melted Ti6Al4V," *Mater. Sci. Eng. A*, vol. 695, pp. 211–220, 2017, doi: https://doi.org/10.1016/j.msea.2017.04.033.

[51] A. H. Maamoun, M. A. Elbestawi, and S. C. Veldhuis, "Influence of Shot Peening on AlSi10Mg Parts Fabricated by Additive Manufacturing," 2018. doi: 10.3390/jmmp2030040.

[52] J. L. Bartlett, B. P. Croom, J. Burdick, D. Henkel, and X. Li, "Revealing mechanisms of residual stress development in additive manufacturing via digital image correlation," *Addit. Manuf.*, vol. 22, pp. 1–12, 2018, doi: https://doi.org/10.1016/j.addma.2018.04.025.

[53] D. Hu, N. Grilli, L. Wang, M. Yang, and W. Yan, "Microscale residual stresses in additively manufactured stainless steel: Computational simulation," *J. Mech. Phys. Solids*, vol. 161, p. 104822, 2022, doi: https://doi.org/10.1016/j.jmps.2022.104822.

[54] A. Ulbricht *et al.*, "Separation of the Formation Mechanisms of Residual Stresses in LPBF 316L," 2020. doi: 10.3390/met10091234.

[55] M. H. Mosallanejad, H. Gashmard, M. Javanbakht, B. Niroumand, and A. Saboori, "A novel feature engineering approach for predicting melt pool depth during LPBF by machine learning models," *Addit. Manuf. Lett.*, vol. 10, p. 100214, 2024, doi: https://doi.org/10.1016/j.addlet.2024.100214.

[56] M. F. Zaeh and G. Branner, "Investigations on residual stresses and deformations in selective laser melting," *Prod. Eng.*, vol. 4, no. 1, pp. 35–45, 2010, doi: 10.1007/s11740-009-0192-y.

[57] L. Parry, I. A. Ashcroft, and R. D. Wildman, "Understanding the effect of laser scan strategy on residual stress in selective laser melting through thermo-mechanical simulation," *Addit. Manuf.*, vol. 12, pp. 1–15, 2016, doi: https://doi.org/10.1016/j.addma.2016.05.014.

[58] A. Saboori, G. Piscopo, M. Lai, A. Salmi, and S. Biamino, "An investigation on the effect of deposition pattern on the microstructure, mechanical properties and residual stress of 316L produced by Directed Energy Deposition," *Mater. Sci. Eng. A*, vol. 780, p. 139179, 2020, doi: https://doi.org/10.1016/j.msea.2020.139179.

[59] X. X. Yao and Z. Zhang, "Laser-particle interaction-based heat source model of laser powder bed fusion additive manufacturing," *Opt. Laser Technol.*, vol. 155, no. January, p. 108402, 2022, doi: 10.1016/j.optlastec.2022.108402.

[60] Y. Yang, Z. J. Li, Y. Yao, and H. L. Dai, “Thermo-mechanical modeling and behavior analysis of titanium-matrix composites via laser powder bed fusion,” *Mech. Mater.*, vol. 206, no. March, p. 105342, 2025, doi: 10.1016/j.mechmat.2025.105342.

[61] T. T. Wohlers, *Wohlers Report...: 3D Printing and Additive Manufacturing, State of the Industry, Annual Worldwide Progress Report*. Wohlers Associates Incorporated, 2014.

[62] W. Gao *et al.*, “The status, challenges, and future of additive manufacturing in engineering,” *Comput. Des.*, vol. 69, pp. 65–89, 2015, doi: https://doi.org/10.1016/j.cad.2015.04.001.

[63] P. Rangaswamy *et al.*, “Residual stresses in LENS® components using neutron diffraction and contour method,” *Mater. Sci. Eng. A*, vol. 399, no. 1, pp. 72–83, 2005, doi: https://doi.org/10.1016/j.msea.2005.02.019.

[64] A. L. Vyatskikh *et al.*, “Residual stress mitigation in directed energy deposition,” *Mater. Sci. Eng. A*, vol. 871, p. 144845, 2023, doi: https://doi.org/10.1016/j.msea.2023.144845.

[65] J. L. Bartlett and X. Li, “An overview of residual stresses in metal powder bed fusion,” *Addit. Manuf.*, vol. 27, pp. 131–149, 2019, doi: https://doi.org/10.1016/j.addma.2019.02.020.

[66] Y. Liu, Y. Yang, and D. Wang, “A study on the residual stress during selective laser melting (SLM) of metallic powder,” *Int. J. Adv. Manuf. Technol.*, vol. 87, no. 1, pp. 647–656, 2016, doi: 10.1007/s00170-016-8466-y.

[67] G. R. Kumar, A. Muralidharan, G. Rajyalakshmi, and S. Swaroop, “Atom probe tomography analysis of hydrogen distribution in laser peened Ti6Al4V alloy to control hydrogen embrittlement,” *Int. J. Adv. Manuf. Technol.*, vol. 114, no. 5, pp. 1395–1408, 2021, doi: 10.1007/s00170-021-06951-5.

[68] V. Y. Gertsman and S. M. Bruemmer, “Study of grain boundary character along intergranular stress corrosion crack paths in austenitic alloys,” *Acta Mater.*, vol. 49, no. 9, pp. 1589–1598, 2001, doi: https://doi.org/10.1016/S1359-6454(01)00064-7.

[69] P. J. Withers and H. K. D. H. Bhadeshia, “Residual stress. Part 1 – Measurement techniques,” *Mater. Sci. Technol.*, vol. 17, no. 4, pp. 355–365, Apr. 2001, doi: 10.1179/026708301101509980.

[70] L. Pintschovius, V. Jung, E. Macherauch, and O. Vöhringer, “Residual stress measurements by means of neutron diffraction,” *Mater. Sci. Eng.*, vol. 61, no. 1, pp. 43–50, 1983, doi: https://doi.org/10.1016/0025-5416(83)90124-6.

[71] C. J. Lammi and D. A. Lados, “Effects of Processing Residual Stresses on Fatigue Crack Growth Behavior of Structural Materials: Experimental Approaches and Microstructural Mechanisms,” *Metall. Mater. Trans. A*, vol. 43, no. 1, pp. 87–107, 2012, doi: 10.1007/s11661-011-0879-5.

[72] M. Dutta, “Residual Stress Measurement in Engineering Materials and Structures Using Neutron Diffraction,” Open University (United Kingdom) PP - England, England, 2000. [Online]. Available: https://www.proquest.com/dissertations-theses/residual-stress-measurement-engineering-materials/docview/304673100/se-2?accountid=28840

[73] J. D. Almer, J. B. Cohen, and B. Moran, “The effects of residual macrostresses and microstresses on fatigue crack initiation,” *Mater. Sci. Eng. A*, vol. 284, no. 1, pp. 268–279, 2000, doi: https://doi.org/10.1016/S0921-5093(99)00779-0.

[74] A. Lodh, K. Thool, and I. Samajdar, “X-ray Diffraction for the Determination of Residual Stress of Crystalline Material: An Overview,” *Trans. Indian Inst. Met.*, vol. 75, no. 4, pp. 983–995, 2022, doi: 10.1007/s12666-022-02540-6.

[75] G. S. Schajer, *Practical residual stress measurement methods*. John Wiley & Sons, 2013.

[76] C. Lachmann, T. H. Nitschke-Pagel, and H. Wohlfahrt, “Nondestructive characterization of residual stress relaxation and fatigue processes in cyclically loaded

welded joints," in *Proceedings of the 6th international conference on residual stress. Oxford. UK pp1400-1409*, Citeseer, 2000.

[77] X. Zheng, J. Li, and Y. Zhou, "X-ray diffraction measurement of residual stress in PZT thin films prepared by pulsed laser deposition," *Acta Mater.*, vol. 52, no. 11, pp. 3313–3322, 2004, doi: https://doi.org/10.1016/j.actamat.2004.02.047.

[78] I. Robinson, P. Eng, and R. Schuster, "Origin of the Surface Sensitivity in Surface X-Ray Diffraction," 1994. doi: 10.12693/aphyspola.86.513.

[79] A. Mishchenko, L. Wu, V. K. da Silva, and A. Scotti, "Analysis of residual stresses resulting from the surface preparation for X-ray diffraction measurement," *J. Brazilian Soc. Mech. Sci. Eng.*, vol. 40, no. 2, p. 94, 2018, doi: 10.1007/s40430-018-1036-5.

[80] P. S. Prevéy, "Current applications of XRD diffraction residual stress measurement," 1996.

[81] G. A. Webster and R. C. Wimpory, "Non-destructive measurement of residual stress by neutron diffraction," *J. Mater. Process. Technol.*, vol. 117, no. 3, pp. 395–399, 2001, doi: 10.1016/S0924-0136(01)00802-0.

[82] J. L. Finney, "The complementary use of X-ray and neutron diffraction in the study of crystals," *Acta Crystallogr. Sect. B Struct. Sci.*, vol. 51, no. 4, pp. 447–467, 1995, doi: 10.1107/S0108768195002734.

[83] H. J. Bunge, "Advantages of Neutron Diffraction in Texture Analysis," *Texture, Stress. Microstruct.*, vol. 10, no. 4, p. 756108, Jan. 1989, doi: https://doi.org/10.1155/TSM.10.265.

[84] C. Casavola, L. S.Campanelli, and C. Pappalettere, "Experimental analysis of residual stresses in the selective laser melting process," Orlando, FL, 2008.

[85] A. Giri and M. M. Mahapatra, "On the measurement of sub-surface residual stresses in SS 304L welds by dry ring core technique," *Measurement*, vol. 106, pp. 152–160, 2017, doi: https://doi.org/10.1016/j.measurement.2017.04.043.

[86] E. Valentini and D. Vangi, "An automatic system for measuring residual stresses by the drilled-hole method," *Weld. Int.*, vol. 8, no. 7, pp. 532–535, Jan. 1994, doi: 10.1080/09507119409548642.

[87] P. Vourna, A. Ktena, P. Tsarabaris, and E. Hristoforou, "Magnetic Residual Stress Monitoring Technique for Ferromagnetic Steels," 2018. doi: 10.3390/met8080592.

[88] S. M. Zadvorkin and L. S. Goruleva, "Evaluation of Residual Stresses in Steel Products Using Magnetic Methods," *J. Mach. Manuf. Reliab.*, vol. 50, no. 2, pp. 118–132, 2021, doi: 10.3103/S1052618821020151.

[89] S. I. Tiitto, "Barkhausen noise method for stress and defect detecting in hard steel," *J. Acoust. Soc. Am.*, vol. 82, no. 4, p. 1472, 1987, doi: 10.1121/1.395209.

[90] H. Singh, M. S. Niranjan, and R. Wattal, "Experimental Investigation into Residual Stress in Ball End Magne-Torheological Finishing," *J. Eng. Res.*, vol. 10, pp. 82–94, 2022, doi: 10.36909/jer.ICAPIE.15097.

[91] Q. He, X. K. Gao, and C. J. Zhou, "Study on the Application of Ultrasonic Nondestructive Testing Method for Residual Stress of Autofrettaged Barrel," *J. Phys. Conf. Ser.*, vol. 2460, no. 1, p. 12054, 2023, doi: 10.1088/1742-6596/2460/1/012054.

[92] A. Ebrahimi, M. Bayat, and E. Norouzi, "Measurement of Residual Stress Using the Ultrasonic Method in Aluminum Welding: FE Analysis and Experimental Study," *Russ. J. Nondestruct. Test.*, vol. 57, no. 8, pp. 669–678, 2021, doi: 10.1134/S1061830921080027.

[93] A. Irina, F. Alexey, B. Vladimir, and B. Igor, "Acoustoelasticity Method with Thermo-optical Generation of Ultrasonic Vibrations for Control of Residual Stresses in Special Pipes," in *2022 International Conference on Information, Control, and Communication Technologies (ICCT)*, 2022, pp. 1–5. doi: 10.1109/ICCT56057.2022.9976513.

[94] N. S. Rossini, M. Dassisti, K. Y. Benyounis, and A. G. Olabi, “Methods of measuring residual stresses in components,” *Mater. Des.*, vol. 35, pp. 572–588, 2012, doi: 10.1016/j.matdes.2011.08.022.

[95] J. GUO, H. FU, B. PAN, and R. KANG, “Recent progress of residual stress measurement methods: A review,” *Chinese J. Aeronaut.*, vol. 34, no. 2, pp. 54–78, 2021, doi: 10.1016/j.cja.2019.10.010.

[96] D. J. Corbin, A. R. Nassar, E. W. Reutzel, A. M. Beese, and P. Michaleris, “Effect of Substrate Thickness and Preheating on the Distortion of Laser Deposited Ti–6Al–4V,” *J. Manuf. Sci. Eng.*, vol. 140, no. 6, Mar. 2018, doi: 10.1115/1.4038890.

[97] X. Lu *et al.*, “Residual stress and distortion of rectangular and S-shaped Ti-6Al-4V parts by Directed Energy Deposition: Modelling and experimental calibration,” *Addit. Manuf.*, vol. 26, pp. 166–179, 2019, doi: https://doi.org/10.1016/j.addma.2019.02.001.

[98] A. Vasinonta, J. L. Beuth, and M. Griffith, “Process Maps for Predicting Residual Stress and Melt Pool Size in the Laser-Based Fabrication of Thin-Walled Structures,” *J. Manuf. Sci. Eng.*, vol. 129, no. 1, pp. 101–109, Mar. 2006, doi: 10.1115/1.2335852.

[99] M.-P. Hong and Y.-S. Kim, “Residual Stress Reduction Technology in Heterogeneous Metal Additive Manufacturing,” 2020. doi: 10.3390/ma13235516.

[100] T. Mishurova *et al.*, “An Assessment of Subsurface Residual Stress Analysis in SLM Ti-6Al-4V,” 2017. doi: 10.3390/ma10040348.

[101] M. Shiomi, K. Osakada, K. Nakamura, T. Yamashita, and F. Abe, “Residual Stress within Metallic Model Made by Selective Laser Melting Process,” *CIRP Ann.*, vol. 53, no. 1, pp. 195–198, 2004, doi: https://doi.org/10.1016/S0007-8506(07)60677-5.

[102] H. Ali, H. Ghadbeigi, and K. Mumtaz, “Effect of scanning strategies on residual stress and mechanical properties of Selective Laser Melted Ti6Al4V,” *Mater. Sci. Eng. A*, vol. 712, pp. 175–187, 2018, doi: https://doi.org/10.1016/j.msea.2017.11.103.

[103] S. Waqar, K. Guo, and J. Sun, “Evolution of residual stress behavior in selective laser melting (SLM) of 316L stainless steel through preheating and in-situ re-scanning techniques,” *Opt. Laser Technol.*, vol. 149, no. December 2021, p. 107806, 2022, doi: 10.1016/j.optlastec.2021.107806.

[104] Q. Chao, S. Thomas, N. Birbilis, P. Cizek, P. D. Hodgson, and D. Fabijanic, “The effect of post-processing heat treatment on the microstructure, residual stress and mechanical properties of selective laser melted 316L stainless steel,” *Mater. Sci. Eng. A*, vol. 821, p. 141611, 2021, doi: https://doi.org/10.1016/j.msea.2021.141611.

[105] H. V Atkinson and S. Davies, “Fundamental aspects of hot isostatic pressing: An overview,” *Metall. Mater. Trans. A*, vol. 31, no. 12, pp. 2981–3000, 2000, doi: 10.1007/s11661-000-0078-2.

[106] L. A. Godlewski, X. Su, T. M. Pollock, and J. E. Allison, “The Effect of Aging on the Relaxation of Residual Stress in Cast Aluminum,” *Metall. Mater. Trans. A*, vol. 44, no. 10, pp. 4809–4818, 2013, doi: 10.1007/s11661-013-1800-1.

[107] S. Das, M. Wohlert, J. J. Beaman, and D. L. Bourell, “Producing metal parts with selective laser sintering/hot isostatic pressing,” *JOM*, vol. 50, no. 12, pp. 17–20, 1998, doi: 10.1007/s11837-998-0299-1.

[108] V. Cruz, Q. Chao, N. Birbilis, D. Fabijanic, P. D. Hodgson, and S. Thomas, “Electrochemical studies on the effect of residual stress on the corrosion of 316L manufactured by selective laser melting,” *Corros. Sci.*, vol. 164, p. 108314, 2020, doi: 10.1016/j.corsci.2019.108314.

[109] R. Husson, C. Baudouin, R. Bigot, and E. Sura, “Consideration of residual stress and geometry during heat treatment to decrease shaft bending,” *Int. J. Adv. Manuf. Technol.*, vol. 72, no. 9, pp. 1455–1463, 2014, doi: 10.1007/s00170-014-5688-8.

[110] S. Y. Kwak and H. Y. Hwang, “Effect of heat treatment residual stress on stress behavior

of constant stress beam," *J. Comput. Des. Eng.*, vol. 5, no. 1, pp. 137–143, Jan. 2018, doi: 10.1016/j.jcde.2017.07.001.

[111] S. Santa-Aho *et al.*, "Additive manufactured 316l stainless-steel samples: Microstructure, residual stress and corrosion characteristics after post-processing," *Metals (Basel).*, vol. 11, no. 2, pp. 1–16, 2021, doi: 10.3390/met11020182.

[112] M. Chimmat and D. Srinivasan, "Understanding the Residual Stress in DMLS CoCrMo and SS316L using X-ray diffraction," *Procedia Struct. Integr.*, vol. 14, pp. 746–757, 2019, doi: https://doi.org/10.1016/j.prostr.2019.05.093.

[113] X. Zhang *et al.*, "Evolution of Microstructure, Residual Stress, and Tensile Properties of Additively Manufactured Stainless Steel Under Heat Treatments," *JOM*, vol. 72, no. 12, pp. 4167–4177, 2020, doi: 10.1007/s11837-020-04433-9.

[114] X. Wang and K. Chou, "The effects of stress relieving heat treatment on the microstructure and residual stress of Inconel 718 fabricated by laser metal powder bed fusion additive manufacturing process," *J. Manuf. Process.*, vol. 48, pp. 154–163, 2019, doi: https://doi.org/10.1016/j.jmapro.2019.10.027.

[115] C. Pei, D. Shi, H. Yuan, and H. Li, "Assessment of mechanical properties and fatigue performance of a selective laser melted nickel-base superalloy Inconel 718," *Mater. Sci. Eng. A*, vol. 759, pp. 278–287, 2019, doi: https://doi.org/10.1016/j.msea.2019.05.007.

[116] Ó. Teixeira, F. J. G. Silva, and E. Atzeni, "Residual stresses and heat treatments of Inconel 718 parts manufactured via metal laser beam powder bed fusion: an overview," *Int. J. Adv. Manuf. Technol.*, vol. 113, no. 11, pp. 3139–3162, 2021, doi: 10.1007/s00170-021-06835-8.

[117] P. Bian, C. Wang, K. Xu, F. Ye, Y. Zhang, and L. Li, "Coupling Analysis on Microstructure and Residual Stress in Selective Laser Melting (SLM) with Varying Key Process Parameters," 2022. doi: 10.3390/ma15051658.

[118] V. Manvatkar, A. De, and T. DebRoy, "Spatial variation of melt pool geometry, peak temperature and solidification parameters during laser assisted additive manufacturing process," *Mater. Sci. Technol.*, vol. 31, no. 8, pp. 924–930, Jun. 2015, doi: 10.1179/1743284714Y.0000000701.

[119] F. Brückner, D. Lepski, and E. Beyer, "Modeling the Influence of Process Parameters and Additional Heat Sources on Residual Stresses in Laser Cladding," *J. Therm. Spray Technol.*, vol. 16, no. 3, pp. 355–373, 2007, doi: 10.1007/s11666-007-9026-7.

[120] X. Lu, M. Chiumenti, M. Cervera, G. Zhang, and X. Lin, "Mitigation of residual stresses and microstructure homogenization in directed energy deposition processes," *Eng. Comput.*, vol. 38, no. 6, pp. 4771–4790, 2022, doi: 10.1007/s00366-021-01563-9.

[121] R. Jendrzejewski and G. Śliwiński, "Investigation of temperature and stress fields in laser cladded coatings," *Appl. Surf. Sci.*, vol. 254, no. 4, pp. 921–925, 2007, doi: https://doi.org/10.1016/j.apsusc.2007.08.014.

[122] E. R. Denlinger, J. C. Heigel, P. Michaleris, and T. A. Palmer, "Effect of inter-layer dwell time on distortion and residual stress in additive manufacturing of titanium and nickel alloys," *J. Mater. Process. Technol.*, vol. 215, pp. 123–131, 2015, doi: https://doi.org/10.1016/j.jmatprotec.2014.07.030.

[123] R. Li and J. Xiong, "Influence of interlayer dwell time on stress field of thin-walled components in WAAM via numerical simulation and experimental tests," *Rapid Prototyp. J.*, vol. 25, no. 8, pp. 1433–1441, Jan. 2019, doi: 10.1108/RPJ-03-2019-0067.

[124] N. Dumontet, B. Malard, and B. Viguier, "Study on the origins of residual stresses in Ti-6Al-4V processed by additive manufacturing," *MATEC Web Conf.*, vol. 321, p. 3001, 2020, doi: 10.1051/matecconf/202032103001.

[125] S. Y. Ivanov, A. Vildanov, P. A. Golovin, A. Artinov, and I. Karpov, "Effect of Inter-Layer Dwell Time on Distortion and Residual Stresses of Laser Metal Deposited Wall,"

Key Eng. Mater., vol. 822, pp. 445–451, 2019, doi: 10.4028/www.scientific.net/KEM.822.445.

[126] L. van Belle, G. Vansteenkiste, and J. C. Boyer, "Investigation of Residual Stresses Induced during the Selective Laser Melting Process," *Key Eng. Mater.*, vol. 554–557, pp. 1828–1834, 2013, doi: 10.4028/www.scientific.net/KEM.554-557.1828.

[127] J.-P. Kruth, J. Deckers, E. Yasa, and R. Wauthlé, "Assessing and comparing influencing factors of residual stresses in selective laser melting using a novel analysis method," *Proc. Inst. Mech. Eng. Part B J. Eng. Manuf.*, vol. 226, no. 6, pp. 980–991, Mar. 2012, doi: 10.1177/0954405412437085.

[128] E. Mirkoohi, H.-C. Tran, Y.-L. Lo, Y.-C. Chang, H.-Y. Lin, and S. Y. Liang, "Effect of Powder Layer Thickness on Residual Stress in Laser Powder Bed Fusion of IN718," Jun. 27, 2022. doi: 10.1115/MSEC2022-85391.

[129] H. Ali, H. Ghadbeigi, and K. Mumtaz, "Processing Parameter Effects on Residual Stress and Mechanical Properties of Selective Laser Melted Ti6Al4V," *J. Mater. Eng. Perform.*, vol. 27, no. 8, pp. 4059–4068, 2018, doi: 10.1007/s11665-018-3477-5.

[130] G. Feng, H. Wang, Y. Wang, D. Deng, and J. Zhang, "Numerical Simulation of Residual Stress and Deformation in Wire Arc Additive Manufacturing," 2022. doi: 10.3390/cryst12060803.

[131] J. C. Diaz *et al.*, "Effect of Layer Thickness and Heat Treatment on Microstructure and Mechanical Properties of Alloy 625 Manufactured by Electron Beam Powder Bed Fusion," 2022. doi: 10.3390/ma15217767.

[132] J. Delgado, J. Ciurana, and C. A. Rodríguez, "Influence of process parameters on part quality and mechanical properties for DMLS and SLM with iron-based materials," *Int. J. Adv. Manuf. Technol.*, vol. 60, no. 5, pp. 601–610, 2012, doi: 10.1007/s00170-011-3643-5.

[133] J. Schröder *et al.*, "Diffraction-Based Residual Stress Characterization in Laser Additive Manufacturing of Metals," 2021. doi: 10.3390/met11111830.

[134] N. Ahmed, I. Barsoum, G. Haidemenopoulos, and R. K. A. Al-Rub, "Process parameter selection and optimization of laser powder bed fusion for 316L stainless steel: A review," *J. Manuf. Process.*, vol. 75, pp. 415–434, 2022, doi: https://doi.org/10.1016/j.jmapro.2021.12.064.

[135] N. C. Levkulich, S. L. Semiatin, J. E. Gockel, J. R. Middendorf, A. T. DeWald, and N. W. Klingbeil, "The effect of process parameters on residual stress evolution and distortion in the laser powder bed fusion of Ti-6Al-4V," *Addit. Manuf.*, vol. 28, pp. 475–484, 2019, doi: https://doi.org/10.1016/j.addma.2019.05.015.

[136] A. M. Jonaet, H. S. Park, and L. C. Myung, "Prediction of residual stress and deformation based on the temperature distribution in 3D-printed parts," *Int. J. Adv. Manuf. Technol.*, vol. 113, no. 7, pp. 2227–2242, 2021, doi: 10.1007/s00170-021-06711-5.

[137] P. Bian, J. Shi, Y. Liu, and Y. Xie, "Influence of laser power and scanning strategy on residual stress distribution in additively manufactured 316L steel," *Opt. Laser Technol.*, vol. 132, p. 106477, 2020, doi: https://doi.org/10.1016/j.optlastec.2020.106477.

[138] G. Vastola, G. Zhang, Q. X. Pei, and Y.-W. Zhang, "Controlling of residual stress in additive manufacturing of Ti6Al4V by finite element modeling," *Addit. Manuf.*, vol. 12, pp. 231–239, 2016, doi: https://doi.org/10.1016/j.addma.2016.05.010.

[139] T. Mukherjee, V. Manvatkar, A. De, and T. DebRoy, "Mitigation of thermal distortion during additive manufacturing," *Scr. Mater.*, vol. 127, pp. 79–83, 2017, doi: https://doi.org/10.1016/j.scriptamat.2016.09.001.

[140] I. Yadroitsev, I. Yadroitsava, P. Bertrand, and I. Smurov, "Factor analysis of selective laser melting process parameters and geometrical characteristics of synthesized single

tracks," *Rapid Prototyp. J.*, vol. 18, no. 3, pp. 201–208, Jan. 2012, doi: 10.1108/13552541211218117.

[141] A. Hussein, L. Hao, C. Yan, and R. Everson, "Finite element simulation of the temperature and stress fields in single layers built without-support in selective laser melting," *Mater. Des.*, vol. 52, pp. 638–647, 2013, doi: https://doi.org/10.1016/j.matdes.2013.05.070.

[142] L.-E. Loh *et al.*, "Numerical investigation and an effective modelling on the Selective Laser Melting (SLM) process with aluminium alloy 6061," *Int. J. Heat Mass Transf.*, vol. 80, pp. 288–300, 2015, doi: https://doi.org/10.1016/j.ijheatmasstransfer.2014.09.014.

[143] K. Cho *et al.*, "Effect of Scan Speed on Microstructure and Tensile Properties of Ti48Al2Cr2Nb Alloys Fabricated via Additive Manufacturing," *Mater. Trans.*, vol. 64, no. 6, pp. 1112–1118, 2023, doi: 10.2320/matertrans.MT-ME2022012.

[144] J. Li, Y. Wu, B. Zhou, and Z. Wei, "Laser Powder Bed Fusion of Pure Tungsten: Effects of Process Parameters on Morphology, Densification, Microstructure," 2021. doi: 10.3390/ma14010165.

[145] M. A. Pekok, R. Setchi, M. Ryan, Q. Han, and D. Gu, "Effect of process parameters on the microstructure and mechanical properties of AA2024 fabricated using selective laser melting," *Int. J. Adv. Manuf. Technol.*, vol. 112, no. 1, pp. 175–192, 2021, doi: 10.1007/s00170-020-06346-y.

[146] D. Gu *et al.*, "Densification behavior, microstructure evolution, and wear performance of selective laser melting processed commercially pure titanium," *Acta Mater.*, vol. 60, no. 9, pp. 3849–3860, 2012, doi: https://doi.org/10.1016/j.actamat.2012.04.006.

[147] Q. Jia and D. Gu, "Selective laser melting additive manufacturing of Inconel 718 superalloy parts: Densification, microstructure and properties," *J. Alloys Compd.*, vol. 585, pp. 713–721, 2014, doi: https://doi.org/10.1016/j.jallcom.2013.09.171.

[148] L. C. Zhang, D. Klemm, J. Eckert, Y. L. Hao, and T. B. Sercombe, "Manufacture by selective laser melting and mechanical behavior of a biomedical Ti–24Nb–4Zr–8Sn alloy," *Scr. Mater.*, vol. 65, no. 1, pp. 21–24, 2011, doi: https://doi.org/10.1016/j.scriptamat.2011.03.024.

[149] A. S. Wu, D. W. Brown, M. Kumar, G. F. Gallegos, and W. E. King, "An Experimental Investigation into Additive Manufacturing-Induced Residual Stresses in 316L Stainless Steel," *Metall. Mater. Trans. A*, vol. 45, no. 13, pp. 6260–6270, 2014, doi: 10.1007/s11661-014-2549-x.

[150] H. Zhao, C. Gao, Z. Wang, Q. Wang, C. Liu, and Y. Zhan, "Residual stress analysis of TC4/Inconel718 functionally graded material produced by laser additive manufacturing based on progressive activation element method," *Int. J. Adv. Manuf. Technol.*, vol. 129, no. 3, pp. 1443–1453, 2023, doi: 10.1007/s00170-023-12348-3.

[151] L. Junfeng and W. Zhengying, "Process Optimization and Microstructure Characterization of Ti6Al4V Manufactured by Selective Laser Melting," *IOP Conf. Ser. Mater. Sci. Eng.*, vol. 269, no. 1, p. 6, doi: DOI:101088/1757-899X/269/1/012026.

[152] B. Vandenbroucke and J. Kruth, "Selective laser melting of biocompatible metals for rapid manufacturing of medical parts," *Rapid Prototyp. J.*, vol. 13, no. 4, pp. 196–203, Jan. 2007, doi: 10.1108/13552540710776142.

[153] E. Lannunziata, N. Zapparoli, L. Iuliano, and A. Saboori, "Effect of powder atomising route on the surface quality and mechanical performance of AISI 316L samples produced via laser powder bed fusion process," *Procedia CIRP*, vol. 118, pp. 688–693, 2023, doi: https://doi.org/10.1016/j.procir.2023.06.118.

[154] H. Meier and C. Haberland, "Experimental studies on selective laser melting of metallic parts," *Materwiss. Werksttech.*, vol. 39, no. 9, pp. 665–670, Sep. 2008, doi:

https://doi.org/10.1002/mawe.200800327.

[155] T. Simson, A. Emmel, A. Dwars, and J. Böhm, "Residual stress measurements on AISI 316L samples manufactured by selective laser melting," *Addit. Manuf.*, vol. 17, pp. 183–189, 2017, doi: https://doi.org/10.1016/j.addma.2017.07.007.

[156] B. K. Panda and S. Sahoo, "Numerical simulation of residual stress in laser based additive manufacturing process," *IOP Conf. Ser. Mater. Sci. Eng.*, vol. 338, no. 1, p. 12030, 2018, doi: 10.1088/1757-899X/338/1/012030.

[157] Y. S. Huo, C. Hong, H. X. Li, and P. Liu, "Influence of different processing parameter on distortion and residual stress of inconel 718 alloys fabricated by selective laser melting (SLM)," *Mater. Res.*, vol. 23, no. 6, 2021, doi: 10.1590/1980-5373-MR-2020-0176.

[158] A. Malmelöv, C.-J. Hassila, M. Fisk, U. Wiklund, and A. Lundbäck, "Numerical modeling and synchrotron diffraction measurements of residual stresses in laser powder bed fusion manufactured alloy 625," *Mater. Des.*, vol. 216, p. 110548, 2022, doi: https://doi.org/10.1016/j.matdes.2022.110548.

[159] B. B. Ravichander, A. Amerinatanzi, and N. Shayesteh Moghaddam, "Study on the Effect of Powder-Bed Fusion Process Parameters on the Quality of as-Built IN718 Parts Using Response Surface Methodology," 2020. doi: 10.3390/met10091180.

[160] E. Liverani, S. Toschi, L. Ceschini, and A. Fortunato, "Effect of selective laser melting (SLM) process parameters on microstructure and mechanical properties of 316L austenitic stainless steel," *J. Mater. Process. Technol.*, vol. 249, pp. 255–263, 2017, doi: https://doi.org/10.1016/j.jmatprotec.2017.05.042.

[161] G. B. Bang *et al.*, "Effect of process parameters for selective laser melting with SUS316L on mechanical and microstructural properties with variation in chemical composition," *Mater. Des.*, vol. 197, p. 109221, 2021, doi: https://doi.org/10.1016/j.matdes.2020.109221.

[162] T. Mishurova, K. Artzt, S. Cabeza, G. Requena, G. Bruno, and J. Haubrich, "Creative Commons CC-BY-NC licence https://creativecommons.org/licenses/by-nc/4.0/ Subsurface Residual Stress Analysis in Ti-6Al-4V Additive Manufactured Parts by Synchrotron X-ray Diffraction." [Online]. Available: http://www.ndt.net/?id=22781

[163] Y. Jia, C. Zeng, and J. Xue, "Scanning strategy optimization for the selective laser melting additive manufacturing of Ti6Al4V," *Eng. Res. Express*, vol. 5, no. 1, p. 15041, 2023, doi: 10.1088/2631-8695/acbd12.

[164] R. Li *et al.*, "Effect of path strategy on residual stress and distortion in laser and cold metal transfer hybrid additive manufacturing," *Addit. Manuf.*, vol. 46, p. 102203, 2021, doi: https://doi.org/10.1016/j.addma.2021.102203.

[165] B. Cheng, S. Shrestha, and K. Chou, "Stress and deformation evaluations of scanning strategy effect in selective laser melting," *Addit. Manuf.*, vol. 12, pp. 240–251, 2016, doi: https://doi.org/10.1016/j.addma.2016.05.007.

[166] W. Zhang, M. Tong, and N. M. Harrison, "Scanning strategies effect on temperature, residual stress and deformation by multi-laser beam powder bed fusion manufacturing," *Addit. Manuf.*, vol. 36, p. 101507, 2020, doi: https://doi.org/10.1016/j.addma.2020.101507.

[167] S. Zou *et al.*, "Numerical analysis of the effect of the scan strategy on the residual stress in the multi-laser selective laser melting," *Results Phys.*, vol. 16, p. 103005, 2020, doi: https://doi.org/10.1016/j.rinp.2020.103005.

[168] Y. Zhan, H. Xu, W. Du, and C. Liu, "Study on the Effect of Scanning Strategy on Residual Stress in Laser Additive Manufacturing with the Laser Ultrasound Technique," *Exp. Mech.*, vol. 62, no. 4, pp. 563–572, 2022, doi: 10.1007/s11340-021-00795-6.

[169] W. Zhang *et al.*, "X-ray diffraction measurements and computational prediction of

residual stress mitigation scanning strategies in powder bed fusion additive manufacturing," *Addit. Manuf.*, vol. 61, p. 103275, 2023, doi: https://doi.org/10.1016/j.addma.2022.103275.

[170] I. Serrano-Munoz *et al.*, "The residual stress in as-built Laser Powder Bed Fusion IN718 alloy as a consequence of the scanning strategy induced microstructure," *Sci. Rep.*, vol. 10, no. 1, p. 14645, 2020, doi: 10.1038/s41598-020-71112-9.

[171] L. Mugwagwa, D. Dimitrov, S. Matope, and I. Yadroitsev, "Evaluation of the impact of scanning strategies on residual stresses in selective laser melting," *Int. J. Adv. Manuf. Technol.*, vol. 102, no. 5, pp. 2441–2450, 2019, doi: 10.1007/s00170-019-03396-9.

[172] M. Strantza *et al.*, "Effect of the scanning strategy on the formation of residual stresses in additively manufactured Ti-6Al-4V," *Addit. Manuf.*, vol. 45, p. 102003, 2021, doi: https://doi.org/10.1016/j.addma.2021.102003.

[173] I. Yadroitsev and I. Yadroitsava, "Evaluation of residual stress in stainless steel 316L and Ti6Al4V samples produced by selective laser melting," *Virtual Phys. Prototyp.*, vol. 10, no. 2, pp. 67–76, Apr. 2015, doi: 10.1080/17452759.2015.1026045.

[174] G. Bi, C. N. Sun, and A. Gasser, "Study on influential factors for process monitoring and control in laser aided additive manufacturing," *J. Mater. Process. Technol.*, vol. 213, no. 3, pp. 463–468, 2013, doi: https://doi.org/10.1016/j.jmatprotec.2012.10.006.

[175] Y. Lu *et al.*, "Study on the microstructure, mechanical property and residual stress of SLM Inconel-718 alloy manufactured by differing island scanning strategy," *Opt. Laser Technol.*, vol. 75, pp. 197–206, 2015, doi: https://doi.org/10.1016/j.optlastec.2015.07.009.

[176] J. P. Kruth, L. Froyen, J. Van Vaerenbergh, P. Mercelis, M. Rombouts, and B. Lauwers, "Selective laser melting of iron-based powder," *J. Mater. Process. Technol.*, vol. 149, no. 1, pp. 616–622, 2004, doi: https://doi.org/10.1016/j.jmatprotec.2003.11.051.

[177] I. K. Sarma, N. Selvaraj, and A. Kumar, "Influence of hexagonal scanning strategy island size on microstructure, residual stress, and corrosion behavior of 17-4 PH SS made by L-PBF," *Proc. Inst. Mech. Eng. Part L J. Mater. Des. Appl.*, vol. 237, no. 5, pp. 1093–1108, Dec. 2022, doi: 10.1177/14644207221136237.

[178] J. Robinson, I. Ashton, P. Fox, E. Jones, and C. Sutcliffe, "Determination of the effect of scan strategy on residual stress in laser powder bed fusion additive manufacturing," *Addit. Manuf.*, vol. 23, pp. 13–24, 2018, doi: https://doi.org/10.1016/j.addma.2018.07.001.

[179] N. Nadammal *et al.*, "Critical role of scan strategies on the development of microstructure, texture, and residual stresses during laser powder bed fusion additive manufacturing," *Addit. Manuf.*, vol. 38, p. 101792, 2021, doi: https://doi.org/10.1016/j.addma.2020.101792.

[180] J. Hajnys, M. Pagáč, J. Měsíček, J. Petru, and M. Król, "Influence of Scanning Strategy Parameters on Residual Stress in the SLM Process According to the Bridge Curvature Method for AISI 316L Stainless Steel," 2020. doi: 10.3390/ma13071659.

[181] X. Lu *et al.*, "Substrate design to minimize residual stresses in Directed Energy Deposition AM processes," *Mater. Des.*, vol. 202, p. 109525, 2021, doi: 10.1016/j.matdes.2021.109525.

[182] O. Gülcan, K. Günaydın, E. Kundakcıoğlu, and A. Tamer, "An experimental and numerical study about the effect of substrate thickness on dimensional deviation in laser powder bed fusion process," *Mater. Res. Express*, vol. 11, no. 7, 2024, doi: 10.1088/2053-1591/ad5fe2.

[183] X. Lu *et al.*, "Crack-free laser powder bed fusion by substrate design," *Addit. Manuf.*, vol. 59, no. PA, p. 103149, 2022, doi: 10.1016/j.addma.2022.103149.

[184] C. Chen, Z. Xiao, W. Zhang, Y. Wang, and H. Zhu, "Effect of laser jump speed on

temperature distribution and thermal stress in laser powder bed fusion," *Opt. Laser Technol.*, vol. 142, p. 107275, 2021, doi: https://doi.org/10.1016/j.optlastec.2021.107275.

[185] P. Mercelis and J. Kruth, "Residual stresses in selective laser sintering and selective laser melting," *Rapid Prototyp. J.*, vol. 12, no. 5, pp. 254–265, Jan. 2006, doi: 10.1108/13552540610707013.

[186] Y. Luo, M. Wang, J. Tu, Y. Jiang, and S. Jiao, "Reduction of residual stress in porous Ti6Al4V by in situ double scanning during laser additive manufacturing," *Int. J. Miner. Metall. Mater.*, vol. 28, no. 11, pp. 1844–1853, 2021, doi: 10.1007/s12613-020-2212-z.

[187] W. Zhang, W. M. Abbott, A. Sasnauskas, and R. Lupoi, "Process Parameters Optimisation for Mitigating Residual Stress in Dual-Laser Beam Powder Bed Fusion Additive Manufacturing," *Metals (Basel).*, vol. 12, no. 3, p. 420, 2022, doi: 10.3390/met12030420.

[188] T. Heeling and K. Wegener, "The effect of multi-beam strategies on selective laser melting of stainless steel 316L," *Addit. Manuf.*, vol. 22, no. August 2017, pp. 334–342, 2018, doi: 10.1016/j.addma.2018.05.026.

[189] Y. Wang, C. Chen, Y. Qi, and H. Zhu, "Residual stress reduction and surface quality improvement of dual-laser powder bed fusion," *Addit. Manuf.*, vol. 71, p. 103565, 2023, doi: https://doi.org/10.1016/j.addma.2023.103565.

[190] M. Matsumoto, M. Shiomi, K. Osakada, and F. Abe, "Finite element analysis of single layer forming on metallic powder bed in rapid prototyping by selective laser processing," *Int. J. Mach. Tools Manuf.*, vol. 42, no. 1, pp. 61–67, 2002, doi: https://doi.org/10.1016/S0890-6955(01)00093-1.

[191] I. A. Roberts, "Investigation of residual stresses in the laser melting of metal powders in additive layer manufacturing," 2012, *University of Wolverhampton*. [Online]. Available: https://wlv.openrepository.com/bitstream/2436/254913/1/Roberts _PhD Thesis.pdf

[192] I. Yadroitsev, P. Krakhmalev, and I. Yadroitsava, "Selective laser melting of Ti6Al4V alloy for biomedical applications: Temperature monitoring and microstructural evolution," *J. Alloys Compd.*, vol. 583, pp. 404–409, 2014, doi: https://doi.org/10.1016/j.jallcom.2013.08.183.

[193] J. Liu, J. Ye, D. Silva Izquierdo, A. Vinel, N. Shamsaei, and S. Shao, "A review of machine learning techniques for process and performance optimization in laser beam powder bed fusion additive manufacturing," *J. Intell. Manuf.*, vol. 34, no. 8, pp. 3249–3275, 2023, doi: 10.1007/s10845-022-02012-0.

[194] C. Kamath, "Data mining and statistical inference in selective laser melting," *Int. J. Adv. Manuf. Technol.*, vol. 86, no. 5–8, pp. 1659–1677, 2016, doi: 10.1007/s00170-015-8289-2.

[195] G. Tapia, S. Khairallah, M. Matthews, W. E. King, and A. Elwany, "Gaussian process-based surrogate modeling framework for process planning in laser powder-bed fusion additive manufacturing of 316L stainless steel," *Int. J. Adv. Manuf. Technol.*, vol. 94, no. 9–12, pp. 3591–3603, 2018, doi: 10.1007/s00170-017-1045-z.

[196] S. Thakur, G. Talla, and P. Verma, "Residual stress, distortion, and porosity analysis of LED heat sink printed by SLM process using machine learning," *Eng. Res. Express*, vol. 3, no. 4, 2021, doi: 10.1088/2631-8695/ac3dc6.

[197] S. H. Wu, U. Tariq, R. Joy, T. Sparks, A. Flood, and F. Liou, "Experimental, Computational, and Machine Learning Methods for Prediction of Residual Stresses in Laser Additive Manufacturing: A Critical Review," *Materials (Basel).*, vol. 17, no. 7, 2024, doi: 10.3390/ma17071498.

[198] M. Woo and H. Ki, "Deep learning-based prediction of thermal residual stress and melt pool characteristics in laser-irradiated carbon steel," *Int. Commun. Heat Mass Transf.*,

vol. 155, p. 107536, 2024, doi: 10.1016/j.icheatmasstransfer.2024.107536.

[199] F. Auricchio and I. Sani, “Istituto Universitario di Studi Superiori di Pavia Selective Laser Melting process simulation : advancements towards a cost-effective model,” 2016.

[200] P. Tan, F. Shen, B. Li, and K. Zhou, “A thermo-metallurgical-mechanical model for selective laser melting of Ti6Al4V,” *Mater. Des.*, vol. 168, p. 107642, 2019, doi: 10.1016/j.matdes.2019.107642.

[201] A. Moradi Ghasemabadi, “Machine Learning Assisted Laser-Powder Bed Fusion Process Optimization for AISI 316L-Cu Alloy,” 2024, *Politecnico di Torino*.

[202] M. Masoomi, J. W. Pegues, S. M. Thompson, and N. Shamsaei, “A numerical and experimental investigation of convective heat transfer during laser-powder bed fusion,” *Addit. Manuf.*, vol. 22, no. May, pp. 729–745, 2018, doi: 10.1016/j.addma.2018.06.021.

[203] A. M. Khorasani, I. Gibson, U. S. Awan, and A. Ghaderi, “The effect of SLM process parameters on density, hardness, tensile strength and surface quality of Ti-6Al-4V,” *Addit. Manuf.*, vol. 25, no. September 2018, pp. 176–186, 2019, doi: 10.1016/j.addma.2018.09.002.

[204] K. S. Al-Rubaie, S. Melotti, A. Rabelo, J. M. Paiva, M. A. Elbestawi, and S. C. Veldhuis, “Machinability of SLM-produced Ti6Al4V titanium alloy parts,” *J. Manuf. Process.*, vol. 57, no. July, pp. 768–786, 2020, doi: 10.1016/j.jmapro.2020.07.035.